# Broadband Microwave Spectroscopy of $YBa_2Cu_3O_{6+y}$

by

Patrick James Turner

B.Sc., McMaster University, 1997
M.Sc., The University of British Columbia, 1999

A THESIS SUBMITTED IN PARTIAL FULFILMENT OF
THE REQUIREMENTS FOR THE DEGREE OF

DOCTOR OF PHILOSOPHY

in

The Faculty of Graduate Studies

(Department of Physics and Astronomy)

We accept this thesis as conforming
to the required standard

THE UNIVERSITY OF BRITISH COLUMBIA

April 6, 2004

*Your file Votre référence*
*ISBN: 0-612-90283-8*
*Our file Notre référence*
*ISBN: 0-612-90283-8*

# Abstract

A novel low temperature bolometric method has been devised and implemented for high-precision measurements of the microwave surface resistance of small single-crystal platelet samples having very low absorption, as a continuous function of frequency from 0.5 GHz to 21 GHz. The key to the success of this non-resonant method is the *in-situ* use of a normal metal reference sample that calibrates the absolute rf field strength. The sample temperature can be controlled independently of the 1.2 K liquid helium bath, allowing for measurements of the temperature evolution of the absorption. Using this method, the minimum detectable power at 1.3 K is 1.5 pW, corresponding to a surface resistance sensitivity of approximately 1 $\mu\Omega$ for a typical 1 mm$\times$1 mm platelet sample.

Using this apparatus, the zero-field electron spin resonance absorption spectrum of a dilute array of Gd ions substituted for Y in $YBa_2Cu_3O_{6+y}$ was used as a unique means of accessing the absolute value of the low temperature magnetic penetration depth $\lambda(T \rightarrow 0)$ in the Meissner state. The result is a new set of precise values of $\lambda$ for screening currents along the three principal crystallographic orientations in samples of $Gd_xY_{1-x}Ba_2Cu_3O_{6+y}$ for three different oxygen-ordered phases having $T_c$ values of 89 K, 75 K and 56 K. The in-plane values are found to depart substantially from the widely-reported relation $T_c \propto 1/\lambda^2$ inferred mainly from muon spin relaxation measurements on polycrystalline materials.

The broadband microwave spectrometer has allowed measurements in unprecedented detail of the in-plane microwave absorption in high-purity $YBa_2Cu_3O_{6+y}$ single crystals. This has permitted, for the first time, the observation of the cusp-shaped conductivity spectra characteristic of weak-limit scattering from impurities in a *d*-wave superconductor. A comparison of the detailed measurements for samples of ortho-II ordered $YBa_2Cu_3O_{6.52}$ ($T_c$=56 K) and fully-doped $YBa_2Cu_3O_{6.993}$ ($T_c$=89 K) with theoretical calculations indicate that intermediate scattering strengths may best describe the behaviour. However, the data reveal a residual quasiparticle spectral weight that is not accounted for within the standard theoretical framework for nodal quasiparticles.

# Contents

# List of Tables

# List of Figures

# Acknowledgements

One of the great things about life as a graduate student is having the opportunity to work closely with a group of talented and dedicated people. I most certainly have had this opportunity during the past six years at UBC, and the work presented in this thesis would not have been possible without the combined contributions of my fellow coworkers in the UBC superconductivity lab. Walter Hardy is an exemplary Ph.D. supervisor — his talent and passion for experimental physics, never-ending curiosity about the physical world, and patience for passing on his insights are nothing short of inspirational. Thanks Walter, for your unfailing support at every stage of my graduate student career, and for your willingness to help me out every single time I asked for it. I have had the fortune of having two supervisors simultaneously throughout my time at UBC and Doug Bonn's support and encouragement has also been unwavering since Richard and I first showed up as soon-to-be McMaster graduates in 1997 (with raccoon eyes following a sunny day at Whistler!). Thanks Doug, for sharing your expansive understanding of physics and the cuprate problem in particular, and for helping us to understand our work in a broader context. Thanks too for sharing your talents in sample preparation and for your keen insights into which experiment would be most important to do next.

It is impossible to overstate the importance of Dr. Ruixing Liang's elevation of the growth of $YBa_2Cu_3O_{6+y}$ single crystals to new heights — his wizardry in the room next door has really kept us all going. The substantial effort of Richard Harris in modeling the microwave conductivity data coming out of the lab has allowed us to be much more definitive in our interpretation of the microwave data. I am also very thankful to have had the tutelage of Pinder Dosanjh in all matters technical — you know all of the tricks and I thank you for sharing *some* of them! I'd like to thank Drs. Mike Hayden and Saeid Kamal for providing such a high standard as you passed the reins of the bolometry experiment over to me so long ago. More recently, I have had the pleasure and privilege of working closely with Dr. David Broun whose amazing enthusiasm for physics will always be contagious. Thanks Dave, for sharing your talents and supporting my endeavors, and for so effortlessly making big contributions to all of the work done in the lab. Thanks also to the numerous other students who have helped to make coming to the lab everyday a pleasure: Chris Bidinosti, Jake Bobowski, Jennifer DeBenedictis, Michael Gardner, Ahmad Hosseini, Marty Kurylowicz, Geoff Mullins, and Andre Wong. Darren Peets has been most helpful in sharing his otherworldly understanding of computers — thanks for all the help Darren. And finally, thanks to the talented guys in the UBC machine shop and electronics shop for all of their help with the construction and repairing of experimental apparatus.

My years in Vancouver have been filled with many good times outside of the lab as well which have been shared with numerous friends and family members. Thanks everyone, for understanding my sometimes-long disappearances when experiments called, and for your support and encouragement throughout my studies. Chris, thanks for getting me back out on skates after such a long hiatus, and Dave and Walter, I will always look back on our hockey mornings fondly. Thanks also to my UBC connections: the intramural volleyball, soccer, and hockey teams, Dave Balzarini's hockey organization, the Blenheim Gang, Ed and Christine, Erin and Joey, the SCARPies, and CBC radio (particularly Ross Porter and other jazz lovers) for keeping me company during the many late nights in the lab. And of course, a big thanks to Holly, for all of your patience, support, and companionship over the years.

# Chapter 1

# Introduction

While scientific advances are often made incrementally through the process of trial and error, on occasion breakthrough discoveries emerge. In condensed matter physics, the discovery of superconductivity first in elemental metals by Onnes in 1911 [1] and then again more recently in a cuprate ceramic by Bednorz and Müller [2] captured the imagination of the research community. Not until over 40 years had passed since the measurements of Onnes did the 1957 theoretical description provided by Bardeen, Cooper and Shrieffer (BCS) [3] explain how many-body interactions could drive the formation of a superconducting ground state. It is hoped that in a similar scenario a theoretical mechanism will unite the many strange electronic and magnetic properties that have been observed in the rare earth copper oxides, including the existence of high temperature superconductivity. One feature of these materials is clear — due to the strong electronic interactions, their physical properties differ substantially from those described by Landau Fermi liquid theory.

## 1.1 Superconductivity in the Cuprates

A sensible starting point for any discussion of cuprate superconductivity is the generic doping phase diagram which describes the landscape of exotic behaviour that has been uncovered. While broadly similar phase diagrams have been found in both hole and electron-doped superconductors, here the discussion is restricted to the hole-doped case. A feature that is common to the crystal structure of the cuprate superconductors is the presence of two-dimensional $CuO_2$ planes which are separated by chemical units whose thickness and structure varies considerably from one member of the cuprate family to another. In the $CuO_2$ layers, the Cu and oxygen atoms form a nearly square lattice. The electronic doping of these sheets is the control parameter that allows access to the different regions of the phase diagram. How to label the various phases that exist within the cuprate phase diagram is by no means a settled issue, however there are some certainties and one particular version is shown in Fig. 1.1. At low doping one finds the antiferromagnetic (AFM) insulating state characteristic of the undoped parent compound. In this case, the planar Cu atoms each have a single 3d hole. The on-site Coulomb interaction is significant enough that the valence electrons are strongly localized on the Cu atoms and AFM ordering with a high Néel temperature results. Simple band structure calculations for the undoped compound predict non-magnetic metallic behaviour [4], and the AFM behaviour indicates the importance of strong electronic interactions within the material. As electrons are removed from the $CuO_2$ planes, the Néel temperature falls as the holes become free to move. The continued removal of electrons uncovers another surprise at slightly

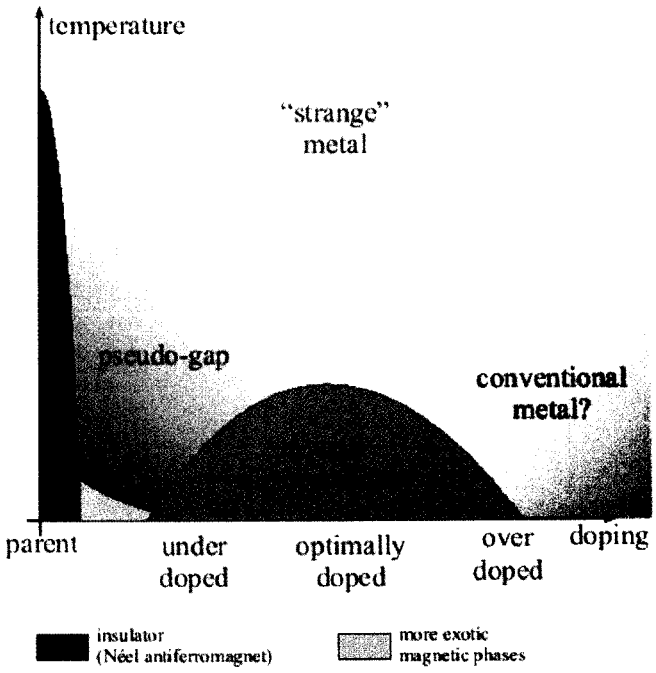


Figure 1.1: Generic phase diagram for the cuprate superconductors. (After Schofield.)

higher doping, that of the unconventional superconducting phase.

In conventional superconductors, a phonon-mediated attractive interaction competes with the Coulomb repulsion and, at low enough temperatures, results in the formation of Cooper pairs of electrons having opposite momentum. The spin-singlet (S=0, $s$-wave) Cooper pairs then collectively form the superconducting condensate whose groundstate energy is separated from the excited states by a gap of magnitude $|\Delta_{\mathbf{k}}|$ that is approximately isotropic in momentum-space. The gap function $\Delta_{\mathbf{k}}$ represents the order parameter of superconductivity and, in the $s$-wave case, it does not change sign on going around the Fermi surface.

In the cuprate problem, the superconductivity arises from doping the AFM insulator as described above. To avoid the on-site Coulomb energy cost, the electrons form Cooper pairs that have finite relative orbital angular momentum. Then the pair wavefunction $\Delta(\mathbf{r}) = \sum_{\mathbf{k}} \Delta_{\mathbf{k}} e^{i\mathbf{k}\cdot\mathbf{r}}$ therefore has zero amplitude at the origin. This concept leads to a clear definition of unconventional superconductivity, and suggests a strong link between electron correlation and unconventional pairing. In order that $\Delta(\mathbf{r})$ vanish at $\mathbf{r} = 0$, the order parameter must sum to zero over the Brillouin zone [5]:

$$\Delta(\mathbf{r}=0) = 0 \quad \Rightarrow \quad \sum_{\mathbf{k}} e^{i\mathbf{k}\cdot 0}\Delta_{\mathbf{k}} = \sum_{\mathbf{k}} \Delta_{\mathbf{k}} = 0. \tag{1.1}$$

This relation holds for all superconductors that do not have $s$-wave symmetry. (For orthorhombicity of the sort found in $YBa_2Cu_3O_{6+y}$, Eq. 1.1 is not strictly true. However, the actual orthorhombic distortion is small and in any case this lifts the dis-

tinction between $s$ and $d_{x^2-y^2}$.) This simple description conveys the importance of the electronic correlations in determining their dynamics, but does not explain what microscopic mechanism drives the pairing interaction.

Other clues as to the nature of the correlations lie within different regions of the phase diagram: a *pseudogap* phase at higher temperatures and intermediate dopings is characterized by the onset of a partial gap in the spin and charge excitation spectra [6]; a *strange metallic* phase above the superconducting dome shows metallic behaviour but with significant departures from normal Fermi liquid behaviour [7]; as the doping is increased further there seems to be a tendency to recover more conventional metallic behaviour [8]. Perhaps the most poorly understood and yet most interesting region is found on the border between the AFM state and the superconducting state. This region has been especially hard to probe experimentally due to the difficulty in producing homogeneous samples, although quite recently some progress has been made in the $YBa_2Cu_3O_{6+y}$ and $La_2CuO_{4+y}$ systems [9–11].

The guiding motivation of the experimentalist should be to perform measurements where the results will permit the clearest interpretation. To this end, the work in this thesis has focussed on parts of the doping phase diagram where the sample chemistry is very well controlled. The samples not only have exceptionally low cation disorder, but we are able to take advantage of ordered phases of oxygen to work at a number of discrete dopings where the samples have a high degree of crystalline order.

## 1.2 Electrodynamic Response of a Superconductor

The phenomenological London equation predates any microscopic understanding of superconductivity, but provides a convenient description of the electrodynamics of the Meissner state in a rather simple form [12]. As a starting point, consider a superconductor in the absence of an applied field. In this case, the groundstate of the system can be expected to have zero net canonical momentum $\langle \mathbf{p} \rangle$ and one can write

$$\langle \mathbf{p} \rangle = \langle m\mathbf{v} + e\mathbf{A} \rangle = 0 \tag{1.2}$$

where $m$ is the electron mass, $e$ is the electron charge and $\mathbf{A}$ is the vector potential. If, as F. and H. London proposed [13], the electrons in the superfluid remain in their groundstate when a magnetic field is applied, then they will be accelerated to a velocity $\mathbf{v}_s = -e\mathbf{A}/m$. For a superfluid of density $n_s$, the current density is then

$$\mathbf{J}_s = n_s e \mathbf{v}_s = -\frac{n_s e^2 \mathbf{A}}{m}. \tag{1.3}$$

(This amounts to a particular choice of gauge – the London gauge.) This equation describes the diamagnetic response that characterizes the superconducting state. Taking a time derivative and using the Maxwell relation $\partial \mathbf{A}/\partial t = -\mathbf{E}$ reveals that the dynamic response will be governed by the equation

$$\frac{\partial \mathbf{J}_s}{\partial t} = \frac{n_s e^2}{m^*} \mathbf{E}. \tag{1.4}$$

If the response is local and the applied field is sinusoidal, then the Fourier transform of this expression can easily be seen to lead to an expression for the purely imaginary conductivity of a collisionless electron gas: $\sigma(\omega) = -in_s e^2/m^*\omega$. Note that causality requires an accompanying zero-frequency delta function $\pi n_s e^2 \delta(\omega)/m^*$ for the real part of the conductivity that corresponds to the energy absorbed in accelerating the non-dissipative superfluid. Taking the curl of Eq. 1.3 gives

$$\nabla \times \mathbf{J}_s + \frac{n_s e^2}{m^*}\mathbf{B} = 0. \tag{1.5}$$

which immediately gives the Meissner effect,

$$\nabla^2 \mathbf{B} = \frac{\mathbf{B}}{\lambda_L^2} \tag{1.6}$$

where $\lambda_L$ is the London penetration depth defined as $\lambda_L^{-2} = \mu_o n_s e^2/m^*$.

The above discussion completely omits the presence of carriers that are dissipative, but these can be added as a parallel channel for conduction. In the clean-limit, sum-rule arguments enable a clean partitioning of the conduction electron density $n$ into a superfluid density $n_s$ and a normal-fluid density $n_n = n - n_s$ corresponding to quasiparticles thermally excited from the condensate. In this type of generalized two-fluid model [14], the temperature dependence of $n_s$ is determined phenomenologically from measurements of the magnetic penetration depth $\lambda$ via the London relation Eq. 1.6. The conductivity can then be written in terms of a superfluid part $\sigma_S$, consisting of the zero-frequency delta function with associated reactive term, and a normal-fluid component $\sigma_N$:

$$\begin{aligned} \sigma(\omega,T) &= \sigma_{1S} - \mathrm{i}\sigma_{2S} + \sigma_{1N} - \mathrm{i}\sigma_{2N} \\ &= \pi\frac{n_s e^2}{m^*}\delta(\omega) - \mathrm{i}\frac{n_s e^2}{m^*\omega} + \sigma_{1N} - \mathrm{i}\sigma_{2N}. \end{aligned} \tag{1.7}$$

Thus, using the London relation for the superfluid density $n_s$, at finite frequencies the conductivity can be written as

$$\sigma(\omega,T) = \sigma_{1N}(\omega,T) - \mathrm{i}\left[\sigma_{2N}(\omega,T) + \frac{1}{\mu_0\omega\lambda_L^2(T)}\right]. \tag{1.8}$$

If we define $\lambda$ to be $[\mu_o\omega\sigma_2]^{-1/2}$, then a measurement of $\lambda$ will not give $\lambda_L$ unless the term $\sigma_{2N}$ is negligible.

In the analysis of spectroscopic data, the fact that the conductivity is a causal response function provides an important constraint. The Kramers–Krönig transform relates the real and imaginary part of the conductivity as

$$\sigma_2(\omega) = \frac{2\omega}{\pi}\mathcal{P}\int_0^\infty \frac{\sigma_1(\Omega)}{\Omega^2 - \omega^2}\mathrm{d}\Omega, \tag{1.9}$$

where $\mathcal{P}$ denotes the principal part of the integral. A corollary of Eq. 1.9 is the oscillator strength sum rule

$$\frac{n_n(T)e^2}{m^*} = \frac{2}{\pi}\int_0^\infty \sigma_1(\omega,T)\mathrm{d}\omega. \tag{1.10}$$

## 1.3 Microwave Surface Impedance

When measuring the response of a conducting surface at microwave frequencies, the experimentally accessible quantity is the surface impedance $Z_s$, defined to be the ratio of the tangential electric field $\mathbf{E}$ at the surface to the total surface current density $\mathbf{J}_{\text{surf}}$. For a surface in the $x-y$ plane, the expression is written

$$Z_s = \frac{E_x(0)}{\int_0^\infty J_x(z)\mathrm{d}z} = \frac{E_x(0)}{H_y(0)} = R_s + \mathrm{i}X_s \tag{1.11}$$

where use has been made of the Maxwell relation $\nabla \times \mathbf{H} = \mathbf{J}$. Specifically relevant to the bolometric work in this thesis, it is shown in Appendix A that the power absorption in a microwave magnetic field is directly proportional to the surface resistance $R_s$:

$$P_{abs} = R_s \int_S H_{rf}^2 \mathrm{d}S, \tag{1.12}$$

where $H_{rf}$ is the root-mean-square magnitude of the magnetic field at the surface $S$. The surface reactance $X_s$ describes the inductive charge response. For situations where the electrodynamic response is local, $Z_s$ is related to the complex conductivity $\sigma = \sigma_1 - \mathrm{i}\sigma_2$ in a straightforward manner via the expression

$$Z_s = R_s + \mathrm{i}X_s = \sqrt{\frac{\mathrm{i}\omega\mu_o}{\sigma}}. \tag{1.13}$$

In metallic samples where the purity is not too high, the electronic scattering rate is typically much larger than the measurement frequency, rendering the conductivity predominantly real (*i.e.* $\sigma_1 \gg \sigma_2$). This is called the classical skin effect regime for a normal metal and is characterized by the property that $R_s = X_s = \sqrt{\mu_o\omega\rho/2}$ where $\rho$ is the dc resisitivity.

It should be noted that in metals of extremely high purity the scattering rate can be low enough that the electron mean free path becomes longer than the electromagnetic skin depth, in which case local electrodynamics breaks down [15]. However, with a careful choice of geometry, any layered material, such as a cuprate superconductor, can be forced to have local electrodynamics by virtue of its quasi-two-dimensional electronic structure [16, 17].

In a superconductor, as pairs are condensed, the superfluid response quickly dwarfs the dissipative response and over most of the temperature range $\sigma_2 \gg \sigma_1$. The surface impedance expressions can then be approximated as

$$\begin{aligned} R_s(\omega,T) &\simeq \frac{1}{2}\mu_o^2\omega^2\lambda^3(T)\sigma_1(\omega,T), \\ X_s(\omega,T) &\simeq \mu_o\omega\lambda(T). \end{aligned} \tag{1.14}$$

Hence, in the superconducting state, one finds the surprising result that the surface resistance $R_s$ is proportional to the real part of the conductivity $\sigma_1$. This is because in the limit $\sigma_2 \gg \sigma_1$ the superfluid on its own determines the spatial profile of the

electromagnetic fields inside the sample, setting the surface electric field through Faraday's law $\nabla \times \mathbf{E} = -\partial \mathbf{B}/\partial t$. A simple integration of the power absorbed per unit volume $\sigma_1 E^2$ gives the desired result $R_s \propto \sigma_1 \lambda^3$. The surface reactance $X_s$ is directly proportional to the penetration depth $\lambda$.

## 1.4 Electrodynamics of the High-$T_c$ Cuprates

For nearly a decade after the discovery of superconductivity in the ceramic cuprate material $La_{2-x}Ba_xCuO_4$ by Bednorz and Müller [2], the symmetry of the superconducting pairing state in the high temperature superconductors remained an open question. It was known, from earlier work done in the context of heavy-fermion superconductivity and $^3$He, that pairing states having non-zero angular momentum were possible. Hence a high priority was placed upon measuring the symmetry of the pairing state in the quest for clues about the interaction responsible for the superconductivity.

Since the magnetic penetration depth is set by the density of the pair condensate, electrodynamic measurements of its temperature dependence probe the structure of the superconducting gap. In the BCS theory for conventional superconductors, a full gap in the density of states exists at the Fermi energy and results in exponentially-activated thermodynamic variables. This has been widely confirmed experimentally in, for example, heat capacity, ultrasound attenuation, nuclear magnetic resonance, and electromagnetic absorption measurements [12]. On the other hand, the finite angular momentum pairing known to exist in unconventional superconductors leads to structure in the energy gap. Figure 1.2 shows a simple diagram contrasting the quasiparticle density of states for an $s$-wave gap and that of a $d$-wave gap which has four nodes at which the gap function crosses the Fermi surface. The hallmark feature of a linear energy dependence of the clean $d$-wave gap at low energy is evident. (Note that it is possible to produce the same behaviour with a very anisotropic $s$-wave gap.[1]) The result of this gap structure is that the thermodynamic variables now exhibit power-law dependences, and in particular the penetration depth develops a linear temperature dependence $\Delta\lambda(T) \propto T$. This was eventually observed in high purity crystals of $YBa_2Cu_3O_{6+y}$ by Hardy *et al.* [19] and taken as strong evidence of $d$-wave pairing in the cuprates. However, the path to this conclusion was not completely straightforward.

One very important feature of conventional superconductors is their insensitivity to disorder. Anderson showed that the presence of random elastic impurity scattering has little effect on $T_c$ or the density of states [20]. In the case of the unconventional superconducting state, the momentum-dependent structure of the gap results in a high sensitivity to impurities. Some of the first insight into this came from early measurements on heavy Fermion superconductors (such as $UBe_{13}$ and $UPt_3$), which revealed significant low energy excitations. Theoretical calculations then showed that if the energy gap had nodes on the Fermi surface, then impurities could lead to a

[1] Measurements that probe the phase of the superconducting order parameter have since provided very clear evidence that the cuprate gap has $d_{x^2-y^2}$ symmetry [18].

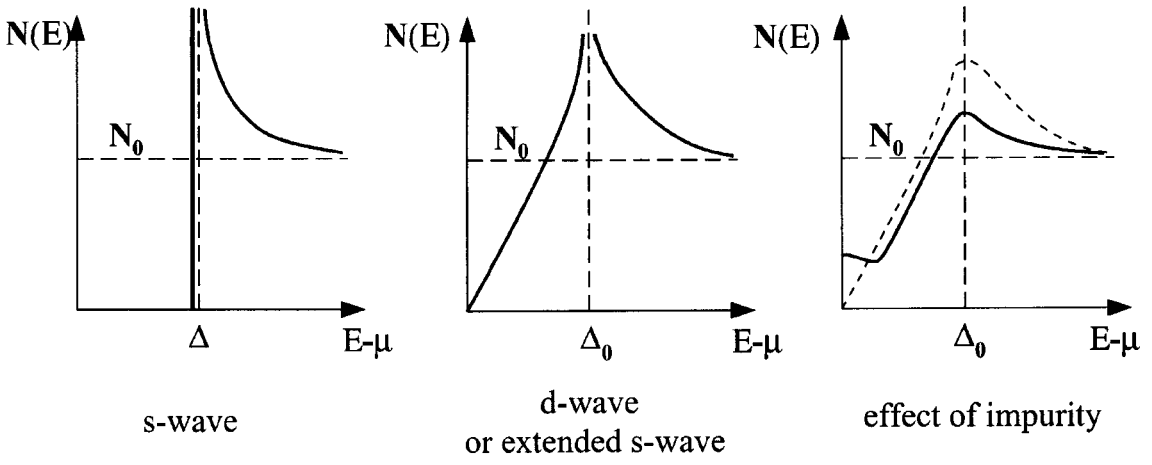


Figure 1.2: Cartoon of the density of states N(E) for an $s$-wave and $d$-wave superconductor and the effect of impurities on the $d$-wave case.

finite density of states at the Fermi level [21]. The explanation for this lies in the way the elastic scattering processes average the anisotropic gap around the Fermi surface. However, in the weak scattering limit the residual density of states is only produced at exponentially small energies. In order to generate significant pair breaking, the limit of resonant impurity scattering must be considered. The result of this is shown pictorially for the $d$-wave case in Fig. 1.2, where the presence of a low concentration of resonant-limit scatterers can introduce a finite density of states at the Fermi level. Along with the proposal that the high temperature superconductors had a gap of $d$-wave symmetry came the realization that the low temperature electrodynamic measurements were likely highly dependent on the purity and crystallinity of the samples. It was demonstrated both experimentally through the systematic addition of Zn impurities [22] and theoretically [23] that such low energy pair-breaking can introduce a crossover of the temperature dependence of the magnetic penetration depth from a $T$ to a $T^2$ behaviour.

Equipped with a convincing understanding of the superconducting pairing symmetry and of the way in which impurities can modify the low energy excitations from the condensate, it should be possible to accurately model the electrical transport properties in the impurity-dominated regime. The physics ought to be the least complicated at low temperatures where the density of states in a clean $d_{x^2-y^2}$ superconductor should have the form $N(\varepsilon) \propto \varepsilon/\Delta_0$ where $\varepsilon$ is the energy and $\Delta_0$ is the gap maximum. In this regime, the scattering rate should be strictly governed by the phase space available for the nodal quasiparticle excitations to scatter into. The microscopic details of the scattering mechanism and the framework for calculating the conductivity provide an opening where novel physics can enter into the problem. In the low temperature limit, the conventional framework is a self-consistent $t$-matrix approximation (SCTMA) that was developed to account for impurity pair-breaking effects that occur in the unitarity scattering limit where the elastic scattering cross-section is maximum. The treatment must be done self-consistently because pair-breaking si-

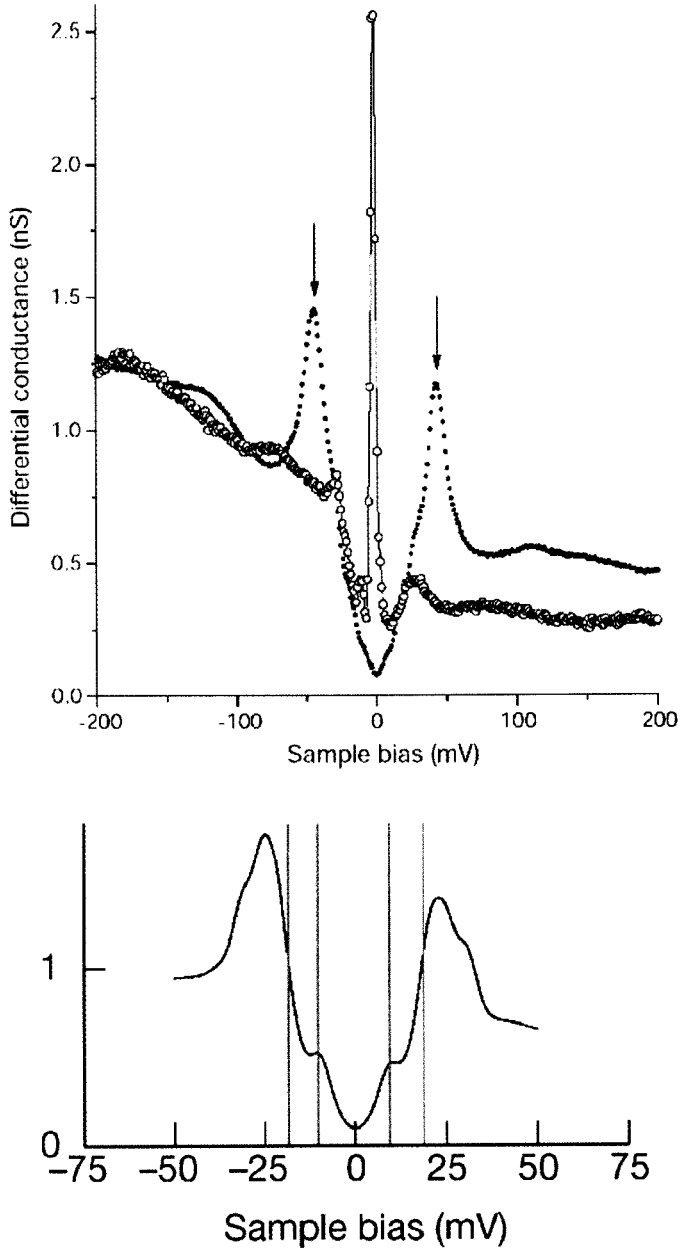


Figure 1.3: STM measurements of the differential conductance (proportional to the density of states) on $Bi_2Sr_2CaCu_2O_8$ showing the effect of impurity bound states on the local density of states at an impurity site. In the top figure, the solid circles are a spectrum taken away from an impurity site showing the usual $d$-wave gap structure. The open circles are for a spectrum taken at the centre of a Zn atom which is seen to strongly suppress the coherence peaks (indicated by arrows) and to induce a large density of states at the Fermi energy. These features are consistent with calculations for strong-limit impurity scattering in a $d$-wave superconductor. In the lower figure, a spectrum at a Ni impurity (averaged over several spectra) shows that the supression of the coherence peak amplitude is much less than at a Zn atom and the impurity resonance is moved away from the Fermi energy, consistent with an intermediate scattering strength.

multaneously modifies both the density of quasiparticle states $N(\varepsilon)$ and their lifetime [24, 25]. A key outcome of this work was an expression for the microwave conductivity that showed that for any scattering strength, $\sigma(\omega, T)$ takes a simple energy-averaged Drude form,

$$\sigma(\omega, T) = \frac{ne^2}{m^*} \left\langle \frac{1}{i\omega + 1/\tau(\varepsilon)} \right\rangle_\varepsilon \tag{1.15}$$

where the energy dependence of the scattering rate $1/\tau(\varepsilon)$ is determined by the strength of the scattering and $\langle \cdots \rangle_\varepsilon$ denotes a thermal average weighted by $N(\varepsilon)$ [24].[2] The physics of the quasiparticle transport can be understood quite easily in the two limits of weak and strong scattering, where in both cases the energy dependence of $N(\varepsilon)$ tends to induce a strong energy dependence in $1/\tau(\varepsilon)$. The limit of weak scattering is characterized by an impurity resonance that is far away from the Fermi energy, thus allowing the application of the Born approximation. In this case, the scattering rate can be calculated using Fermi's golden rule and is proportional to the density of states, *i.e.* $1/\tau(\varepsilon) \approx \Gamma_B \varepsilon$. In the unitarity limit, the scattering resonance is *at* the Fermi energy and results in a modification of the density of states. In this case the scattering rate takes an approximate form $1/\tau(\varepsilon) \approx \Gamma_u/\varepsilon$. Both scale factors $\Gamma_u$ and $\Gamma_B$ are set by the density of impurities [26].

Another avenue for insight into the way in which impurities scatter quasiparticles is through high resolution scanning tunneling microscopy (STM) measurements which obtain a map of the local density of quasiparticle states over atomic lengthscales. It was predicted quite early in the study of the cuprates that STM measurements would provide the spatial information needed to determine the symmetry of the pairing state [27]. This has been borne out beautifully with recent measurements that have furthermore provided a very clear experimental picture of the way in which impurities can locally modify superconductivity [28, 29]. Particularly impressive are studies by the group of J.C. Davis, on $Bi_2Sr_2CaCu_2O_8$ samples intentionally doped with Ni and Zn impurities. The data in Fig. 1.3 shows that the normal $d$-wave density of states seen in the material becomes modified when the STM tip is moved to the location of impurity. In the case of Zn, the magnitude of the superconducting gap is strongly suppressed and a large density of states at the Fermi energy arises, consistent with the description given above for unitarity-limit scattering. This is in contrast to the case of the Ni atom in which the suppression of the gap is much less pronounced and the impurity resonance has moved away from the Fermi energy.

Given the success of the SCTMA in describing the effect of impurities on the low temperature penetration depth, and the extent to which the STM-measured impurity resonances do indeed behave in accord with the SCTMA predictions, it is somewhat surprising that previous measurements of the real part of the microwave conductivity have shown poor agreement with the theory [30]. This inconsistency with a theory that has been so successful in explaining other aspects of the unconventional superconducting state is an indication of the extreme scrutiny that microwave spectroscopy can subject a superconductor to. Whereas an STM measurement probes the superconductivity on a very local scale, a microwave measurement explores the

[2]The complete expression is given in Appendix B.

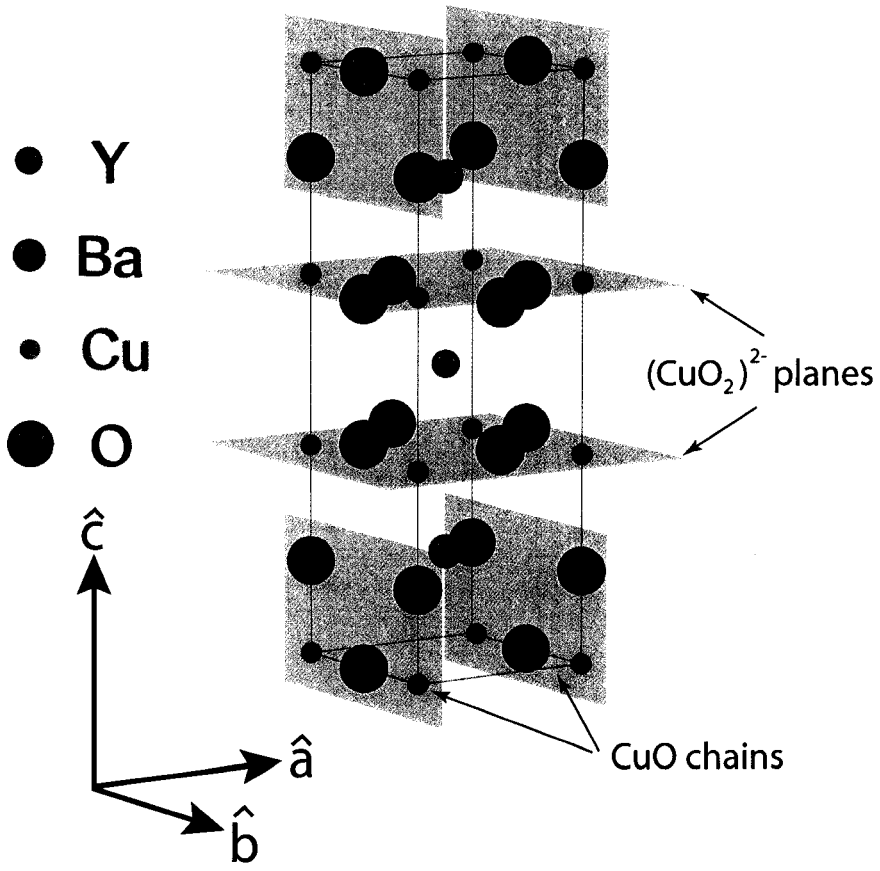


Figure 1.4: The orthorhombic unit cell of $YBa_2Cu_3O_{6+y}$ highlighting the $CuO_2$ planes and CuO chains that run along the $\hat{b}$-axis direction. The hole doping in this system is controlled by setting the concentration and ordering of the CuO chain oxygen atoms, but the mechanism driving superconductivity is believed to reside within the two-dimensional $CuO_2$ planes. Figure provided courtesy of D. Peets.

long wavelength properties, and it is the long wavelength behaviour that should be most sensitive to *qualitative* properties of the underlying physics. In other words, we expect the qualitative differences between distinct electronic states, for example, between a Fermi liquid and a more exotic non-Fermi liquid state, to be most definitively revealed in the long wavelength physical properties. (At short distances, the physics is necessarily more complicated, and many different processes may be conspiring to produce a particular result. At long wavelengths, the possibilities are more limited, and there the theoretical predictions stand more chance of drawing unique distinctions.) Very detailed microwave spectroscopy measurements that examine the way that impurities scatter quasiparticles in a $d$-wave superconductor is one of the central focuses of this thesis, and is the subject of Chapter 4.

## 1.5 $YBa_2Cu_3O_{6+y}$ Single Crystals

The bilayer compound $YBa_2Cu_3O_{6+y}$ remains the most widely studied of the cuprate superconductors, and is the subject of all of the work presented in this thesis. Reasons for its popularity include the relative ease with which high quality single-crystal and thin-film samples can be grown, and the fact that the chemistry of the compound ensures a low level of cation cross-substitution ($< 10^{-4}$). Figure 1.4 shows the orthorhombic unit cell of the fully-oxygenated material (y=1) which has a perovskite-like crystal structure. The lattice parameters are: $\hat{a}$=3.9198 Å, $\hat{b}$=3.8849 Å and $\hat{c}$=11.6762 Å. The single CuO chain layer indicated in the figure acts as a charge reservoir for the doping of holes into the two $CuO_2$ plane layers. The undoped material (y=0) has no oxygen atoms in the chain layer and is in the AFM insulating state. Just above y=6.3 the first superconductivity emerges and the critical temperature continuously rises with doping as shown in Fig. 1.5. This process is not without subtleties, and it is important to realize that the chain oxygen content alone does not determine the doping level in the planes; charge transfer is driven by the oxygen coordination number of the chain Cu atom [31]. This feature is especially important around y=6.3 where discussions of any phase diagram must pay careful attention to the extent to which the oxygens are ordered [10]. (The data below y=6.4 shown in Fig. 1.5 gives the maximum $T_c$ value achieved by a room temperature anneal, for a given y value.) $T_c$ can be increased further by increasing the ordering through the application of pressure, a subject of current exploration [32]. The microwave measurements presented in this thesis were all done on samples having considerably higher doping levels, which are indicated by the open red squares in Fig. 1.5.

The present work exclusively used the single crystal samples grown by Dr. Ruixing Liang at UBC using a self-flux technique that is described briefly here [33–35]. To begin, the 99.995-99.999 at.% purity constituent compounds ($Y_2O_3$–BaO–CuO) are combined in a crucible and heated to about 1000°C and melted. As the melt is cooled at a controlled rate, a localized temperature gradient causes the crystals to nucleate out of the melt onto the crucible walls. The growth rate is most rapid in the $\hat{a}$-$\hat{b}$-plane and the largest crystals tend to grow with the $\hat{c}$-axis parallel to the crucible wall, extending outward from the crucible wall. Typically the crystals are up to several mm in in-plane dimension and less than 0.5 mm in thickness. Following the growth, flux decanting, and crystal harvesting, the oxygen concentration is set, the sample mechanically detwinned under uniaxial stress at about 200°C, and then annealed to form phases having ordered oxygen atoms in the CuO chains. The particular order in which these final steps are performed depends on the desired doping level.

Significant improvements in the purity of $YBa_2Cu_3O_{6+y}$ single crystals followed the recent advent of $BaZrO_3$ crucibles, which do not corrode during crystal growth [34, 36]. This improvement in the purity resulted in an increase in the mobility of the chain oxygen atoms thus allowing the production of samples that had longer correlation lengths for the ordering than had been previously observed [35]. As has already been touched upon, the existence of oxygen-ordered phases is an important part of understanding the $YBa_2Cu_3O_{6+y}$ phase diagram. Although the chain oxygen layers are some distance away from the $CuO_2$ plane layers where the superconductivity

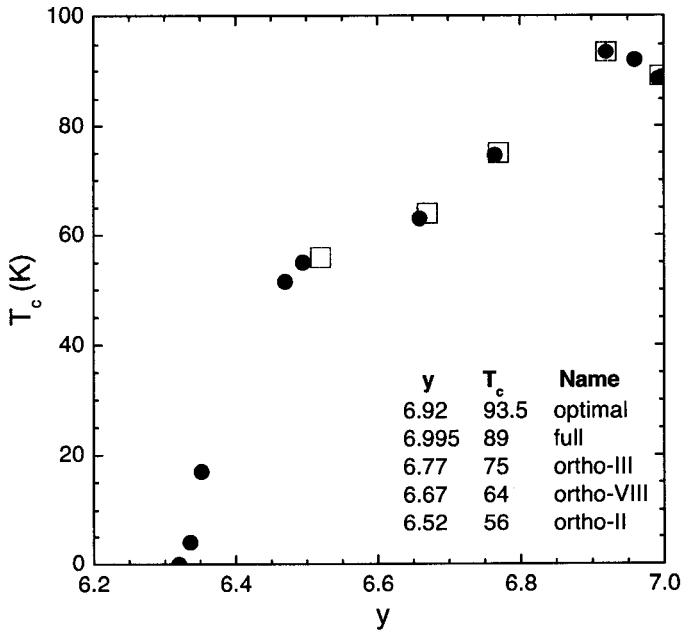


Figure 1.5: The $YBa_2Cu_3O_{6+y}$ superconducting phase diagram [32]. The microwave measurements presented in this thesis were made on samples having $T_c$ values indicated by the open red boxes.

is thought to reside, the extent to which the off-plane disorder is important is not yet fully understood. In the present microwave work the ordered phases are exploited as an opportunity to study samples having minimal disorder that may mask the intrinsic physics of the material. It will be demonstrated in Chapter 3 that the zero-field electron spin resonance spectroscopy technique developed as part of this thesis work, although developed to serve an entirely different purpose, provides a sensitive means of examining the ordering of the chain oxygen atoms. A more complete discussion of oxygen ordering is given at that time.

# Chapter 2

# Broadband Bolometric Microwave Technique

This chapter provides a detailed description of the experimental method that has been developed as the core of this thesis work and used to obtain high resolution measurements of the low temperature electromagnetic absorption spectrum of a number of different superconducting materials. First, a general survey of the methods that have been applied to measuring the microwave surface resistance of superconductors is presented. Having demonstrated a clear motivation for its development, a detailed description of the broadband bolometric apparatus completes the chapter.

## 2.1 Microwave Techniques and Unconventional Superconductivity

All unconventional superconductors known to date are alloys, made from as many as five different elements. The chemistry can be complex and, coupled with the fact that an unconventional superconducting state may be highly sensitive to impurities and disorder, it is important to study the best quality samples. In general, thin films of superconductors are more likely to retain significant disorder, and the materials having the highest perfection tend to be small single crystals, typically having a surface area of approximately 1 $mm^2$ or less. Working with these small samples is technically demanding since the experimental apparatus must be carefully tailored to probe small changes in the penetration depth or the small absorption in the superconducting crystals. Resolving these features in the microwave region has been successfully achieved over most of the temperature range below $T_c$ by the use of cavity-perturbation techniques [37, 38]. In these experiments, the sample under test is brought into the microwave fields of a high quality-factor resonant structure, such as a superconducting cavity or a low-loss dielectric puck. Changes in the resonant bandwidth and frequency of the resonator are related in a straightforward way to changes in the absorption and penetration depth of the sample respectively.

A limitation of such techniques is that the resonator is generally restricted to operation at a single fixed frequency, therefore requiring the use of many separate experimental apparatuses in order to provide a spectrum. Furthermore, a very general limitation of the cavity perturbation method is that the dissipation of the unknown sample must be comparable to the dissipation of the cavity itself in order for the absorption to be measured with high precision — a very strong requirement when the sample is a high quality superconductor in the $T \rightarrow 0$ limit. It is also important

to understand the non-perturbative effects of the resonator carefully to ensure that systematic errors are absent. The measurement of the residual absorption in superconductors is challenging at any frequency: in the case of infra-red spectroscopy the problem becomes that of measuring values of reflectance that are very close to unity. The challenge lies in the calibration of the measurement, and in both microwave and infra-red work, one relies on having a reference sample of known absorption to calibrate the loss in the walls of the microwave resonator or the infra-red reflectance. Despite these limitations, resonant microwave techniques have been the only methods with sufficient sensitivity to measure the evolution of the microwave absorption over a wide temperature range, albeit with limited frequency coverage. An example of this is provided by recent work done at UBC where five superconducting cavities operating between 1 GHz and 75 GHz were used to obtain a coarse conductivity spectrum of $YBa_2Cu_3O_{6+y}$[30].

A natural way of covering the microwave spectrum in more detail than is possible using a set of fixed-frequency resonators is through the use of bolometric detection. This approach was used as part of a pioneering study in 1959 by Biondi and Garfunkel who performed detailed measurements of the temperature dependence of the superconducting gap frequency in Al [39]. They carefully prepared an extruded Al waveguide section measuring $0.05 \times 1.06 \times 8$ cm$^3$ having a low frequency cutoff of 14.3 GHz. The guide had one end terminated in a short circuit and the other end thermally isolated from but aligned with a Cu waveguide that functioned as a power monitor. Using a carbon resistance thermometer [40] to detect the temperature rise of the guide, they were able to resolve $\sim$1 nW power absorptions over a temperature range $0.38 < T < 1.25$ K.

More recently, frequency-scanned bolometric measurements have proven useful in probing collective excitations in small samples of high-$T_c$ cuprates. The principal figure in this work has been Yuji Matsuda who has applied the bolometric method to situations where superconducting cavities were unsuitable. These include high-field measurements of vortex dynamics at a fixed-frequency of 30 GHz [41], as well as frequency-scanned measurements of resonant absorption processes above 20 GHz [42–44]. Throughout this work, a low temperature minimum detectable power of $\sim$0.1 nW is stated. A 5.95 GHz Nb resonator was used by Rubin *et al.* to make a fixed-frequency bolometric measurement of $R_s(T)$ in single crystal samples of $YBa_2Cu_3O_{6+y}$[45]. In order to resolve the small absorption with their system, an array of four crystals was used that had a total surface area of 20 mm$^2$. Even with this large effective surface area, they found that the measurement was dominated by losses in the sample holder below 80 K for high quality $YBa_2Cu_3O_{6+y}$ samples. None of these previous techniques have focussed on the challenge of resolving the absolute absorption of high-quality single crystals of a cuprate superconductor across a broad frequency range at low temperatures.

## 2.2 The Bolometric Microwave Spectroscopy Apparatus

This section provides a detailed description of the apparatus that has been designed and constructed as a means of obtaining continuous-frequency measurements of the absolute microwave surface resistance in low-loss single crystal samples. This has been achieved using a bolometric technique whose essence we summarize here. The sample of interest is weakly thermally anchored to a base temperature and exposed to a radio frequency (or microwave) magnetic field $H_{rf}$ whose frequency can be varied. Measurements of the temperature rise of the sample as a function of frequency directly give $R_s(\omega)$. To enhance rejection of spurious temperature variations, we amplitude modulate the rf power at low frequency and the resulting temperature oscillations of the sample are detected synchronously. We first discuss some general considerations of the method of bolometric detection before delving into a detailed description of the experimental apparatus.

A characteristic feature of many electronic materials of current interest is reduced dimensionality, which gives rise to highly anisotropic transport coefficients. When making microwave measurements, a well-defined geometry must be chosen in order to separate the individual components of the conductivity tensor, and also to ensure that demagnetization effects are under control. One particularly clean approach that has been widely used places the sample to be characterized near a position of high symmetry in a microwave enclosure, in the quasi-homogeneous microwave magnetic field near an electric node. Single crystal samples of many of the cuprate superconductors grow naturally as platelets having a broad $\hat{a}$–$\hat{b}$ plane crystal face and thin $\hat{c}$-axis dimension. In this case, demagnetization effects are minimized if the broad face of the sample is aligned parallel to the field. In response to the applied rf magnetic field, screening currents flow near the surface of the sample along the broad $\hat{a}$ or $\hat{b}$ face and then necessarily flow along the $\hat{c}$ direction to complete a closed path. In some cases, it is desirable to work with samples that are very thin, rendering the $\hat{c}$-axis contribution negligible. Alternatively, by varying the aspect ratio of the sample by either cleaving or polishing, one can make a series of measurements to separate the different crystallographic contributions, without changing samples. For example, in $YBa_2Cu_3O_{6+y}$, the conductivity parallel to the two dimensional $CuO_2$ plane layers can be several orders of magnitude larger than that perpendicular to the weakly-coupled planes. Typical as-grown crystal dimensions are $1.0 \times 1.0 \times .01$ mm$^3$. For this aspect ratio, the $\hat{c}$-axis contribution was shown to be unimportant by using the technique of cleaving a sample into many pieces [46]. We note here that all measurements presented in this thesis employ the low-demagnetization sample orientation discussed above.

The broadband surface-resistance measurement technique we describe in the rest of this chapter provides three distinct technical advances over previous bolometric approaches: a uniform microwave field configuration in the sample region that permits the separation of anisotropic conductivity components; the use of an *in-situ* reference sample that calibrates the microwave field strength at the sample absolutely; and

very high sensitivity afforded by the choice of a resistive bolometer optimized for the low-temperature range and mounted on a miniaturized thermal stage. These features of our apparatus permit precision measurements of the absolute value of $R_s(\omega, T)$ in very-low-loss samples down to 1.2 K and over the frequency range 0.5-21 GHz.

### 2.2.1 Bolometric Detection: General Considerations

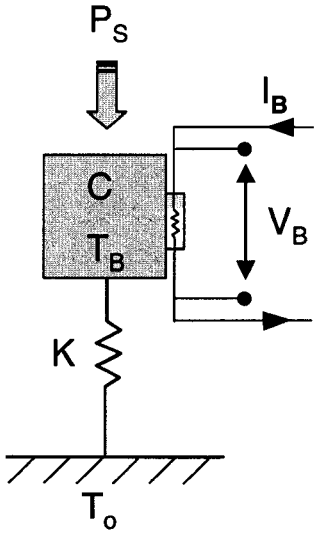


Figure 2.1: A simple thermal model consisting of a heat capacity $C$ thermally isolated from base temperature $T_0$ by a weak thermal link of conductance $K$. The resistive bolometer is thermally anchored to $C$ and monitors its temperature, $T_B$ , which is elevated above $T_0$ by a constant current bias $I_B$ passing through the bolometer. The absorption of incident signal power $P_s$ causes heating in $C$, detectable as a temperature rise through a change in the voltage $V_B$.

An instructive starting point is to consider the minimum power detectable by a simple thermal stage, the temperature of which is monitored by a resistive bolometer, as depicted in Fig. 2.1. In general, the thermal model of the bolometer stage should include a distributed heat capacity through which the thermal currents flow. However, we show in Section 2.2.5 that a necessary condition for optimal sensitivity is that the thermal weak link be operated in the low frequency limit where it *is* well approximated by a lumped thermal mass and a weak thermal link having negligible heat capacity. Here, we consider the bolometer to have a resistance $R_B$ and to be in thermal equilibrium with a larger heat capacity $C$ representing contributions from the sample, its holder, and the weak thermal link. This combination is weakly connected, via a thermal conductance $K$, to a heat sink maintained at base temperature $T_0$. The bolometer is heated to its operating temperature $T_B$ by a bias power $P_B = I_B^2 R_B$, where $I_B$ is the fixed bolometer bias current. For this analysis we do not consider feedback effects, although they are very important in the special case of transition edge

bolometers [47]. As a result, we consider a configuration where $I_B$ provides only modest self-heating of the bolometer, such that $\gamma \equiv (T_B - T_0)/T_0 \lesssim 1$. An incident signal power $P_S$ raises the temperature by an amount $\delta T_B = P_S/K$, causing a change in the readout voltage across the bolometer $\delta V_B = I_B(\mathrm{d}R_B/\mathrm{d}T)\delta T_B = I_B(\mathrm{d}R_B/\mathrm{d}T)P_S/K$. We then define a threshold detectable signal level that is equal to the thermal noise $v_n$ generated in a bandwidth $\Delta\nu$ in the bolometer, $\overline{v_n^2} = 4k_B T_B R_B \Delta\nu$. It is then possible to write an expression for the minimum detectable power $P_S^{min}$ in terms of the dimensionless sensitivity of the bolometer $S_d = T/R\,|\mathrm{d}R/\mathrm{d}T|$, typically of order unity (see Fig. 2.2), the noise power $P_n = k_B T_B \Delta\nu$, and the bolometer bias power $P_B$:

$$P_S^{min} = \frac{2}{\gamma S_d}\sqrt{P_n P_B}. \tag{2.1}$$

From this expression one immediately sees that it is desirable to minimize both the bias and noise powers, within the combined constraints of maintaining the bolometer temperature at $T_B$ and keeping the thermal response time fixed at a suitably short value. By miniaturization of the sample holder, the bias power required to reach a given temperature can be considerably reduced, while at the same time maintaining a practical thermal time constant. We note here that the *intrinsic* noise power is set by the thermal (Johnson) noise from the bolometer resistance at temperature $T_B$; in practice, the bolometer may show excess noise.

### 2.2.2 Temperature Sensors

For the work presented in this thesis, our bolometer of choice has been a Cernox 1050-BC resistance thermometer from LakeShore Cryotronics [48]. Figure 2.2 presents its resistance as a function of temperature, as well as the corresponding dimensionless sensitivity $S_d$ which exhibits a rather weak temperature dependence from 1-300 K. Our recent measurements of the low temperature noise spectrum indicate that the device is far from optimal; it shows approximately 40 dB of excess noise in the presence of a constant 1.3 $\mu$A bias current, a typical value used for our low temperature microwave work. This accounts quantitatively for the discrepancy between the minimum detectable power at 1.3 K of 17 fW calculated using Eq. 2.1 assuming only Johnson noise, and the experimentally determined value of 1.5 pW.

The source of the excess noise in the Cernox sensor has not been uniquely identified, however one possible candidate is generation-recombination noise that is known to exist in granular semiconductors [49]. In this case, random fluctuations in the carrier density result from the presence of energy level traps from defect and impurity states that exist within the semiconducting bandgap. Generation-recombination noise can be minimized by preparing single crystal semiconducting samples that have been doped in a way which avoids these traps. One way of achieving such a device is through the process of neutron transmutation doping (NTD) which results in a carefully controlled doping level [50]. We have purchased an NTD sensor from Haller-Beeman Associates Inc. [51], and preliminary measurements of the low frequency noise spectrum reveal no increase in the noise under constant current bias,

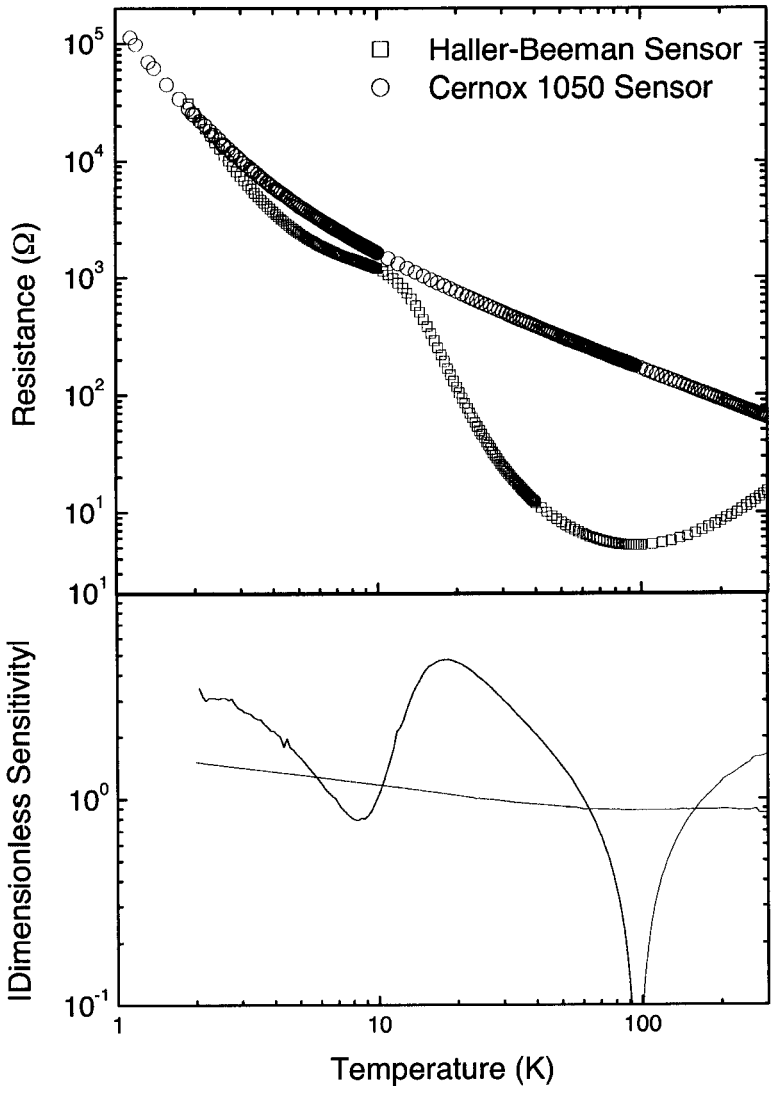


Figure 2.2: The temperature-dependent resistance of a Cernox 1050-BC and Haller-Beeman NTD-C model resistance thermometers calibrated against the Quantum Design SQUID magnetometer thermometer in the UBC superconductivity lab. The lower panel shows the dimensionless sensitivity $S_d = T/R\,|\mathrm{d}R/\mathrm{d}T|$ for the two sensors.

unlike the Cernox sensor. A comparison of the temperature calibration of the resistance, as well as the dimensionless sensitivity $S_d$ of the Haller-Beeman model NTD-C and Lakeshore Cernox model CX1050-BC sensors is provided in Fig. 2.2. Clearly the sensitivity of the bolometric method will be greatly enhanced if it is possible to avoid the 40 dB of excess noise observed in the Cernox sensor.

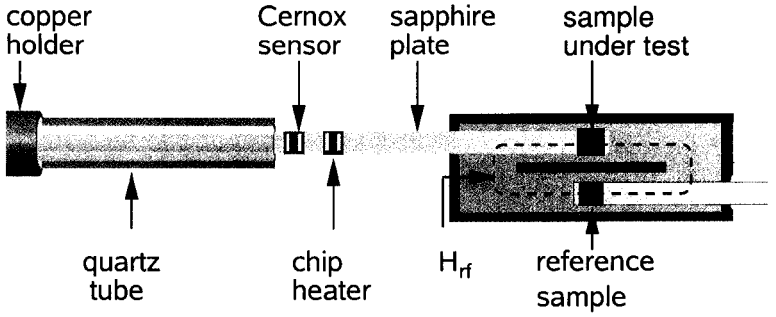


Figure 2.3: Schematic cross-section of the terminated coaxial line region showing the sample and reference materials suspended on sapphire plates in symmetric locations in the rf magnetic field. The sapphire plate is epoxied into the bore of a quartz tube which thermally isolates it from the copper holder, fixed at the temperature of the 1.2 K helium bath. The reference sample holder is not shown in this view. A photograph of the actual hot-finger is shown in Fig. 2.4.

### 2.2.3 Design and Description of Apparatus

For our method of bolometric detection to be most useful, it is necessary to deliver microwaves to the sample across a broad range of frequency. At the same time, one must not only accurately control the polarization of the microwave field at the sample, but also maintain a fixed relationship between the field intensity at the sample under test and the field intensity at the reference sample. Essential to this is the design of the microwave waveguide. We use a custom-made transmission line, shown in cross-section in Fig. 2.3, which consists of a rectangular outer conductor that measures 8.90 mm $\times$ 4.06 mm in cross-section and a broad, flat centre conductor, or septum, that measures 4.95 mm $\times$ 0.91 mm. This supports a TEM mode in which the magnetic fields lie in the transverse plane and form closed loops around the centre conductor, setting a fixed relationship between the microwave field strengths on either side of the septum. The line is terminated by shorting the centre conductor and outer conductor with a flat, metallic endwall. This enforces an electric field node at the end of the waveguide, adjacent to which we locate the small platelet sample and reference, with their flat faces parallel and very close to the endwall. The broad centre conductor ensures spatially uniform fields over the dimensions of the sample, making it possible to drive screening currents selectively along a chosen crystallographic direction. The electrodynamics of the rectangular waveguide are discussed in more detail in Section 2.2.6. A strong variation in the power delivered to the sample as a function of frequency arises due to standing waves in the microwave circuit. In order to properly account for this, we have incorporated an *in-situ* normal-metal reference sample of known surface resistance that acts as an absolute power meter. This second sample is held in a position that is electromagnetically equivalent to that of the test sample, on a separate thermal stage.

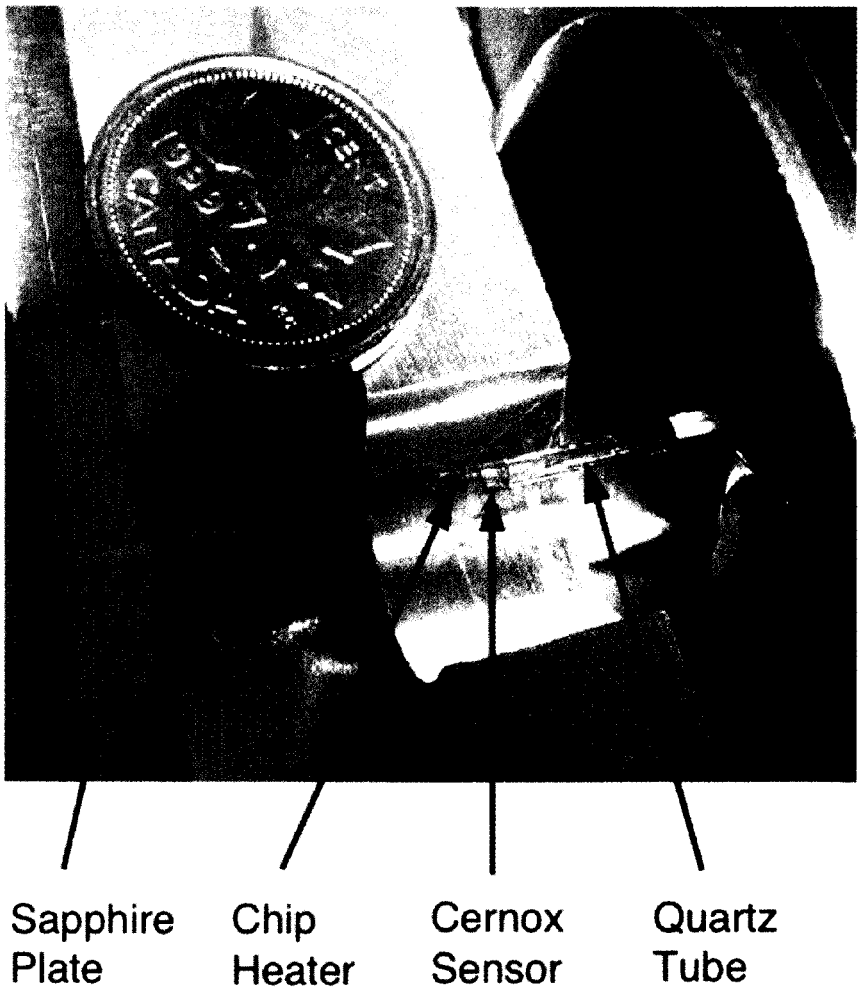


Figure 2.4: Photograph of the miniaturized sample thermal stage consisting of a quartz tube thermal weak link and sapphire isothermal stage that holds the Cernox bolometer and heater. The superconducting electrical leads running along the quartz tube are barely discernible in the photo. The sample to be measured is mounted on the thin sapphire plate using a small amount of vacuum grease, aligned with the score marks visible on the brass alignment block to the left in the photo. The brass and aluminum mounting block seen here is removed before assembling the probe.

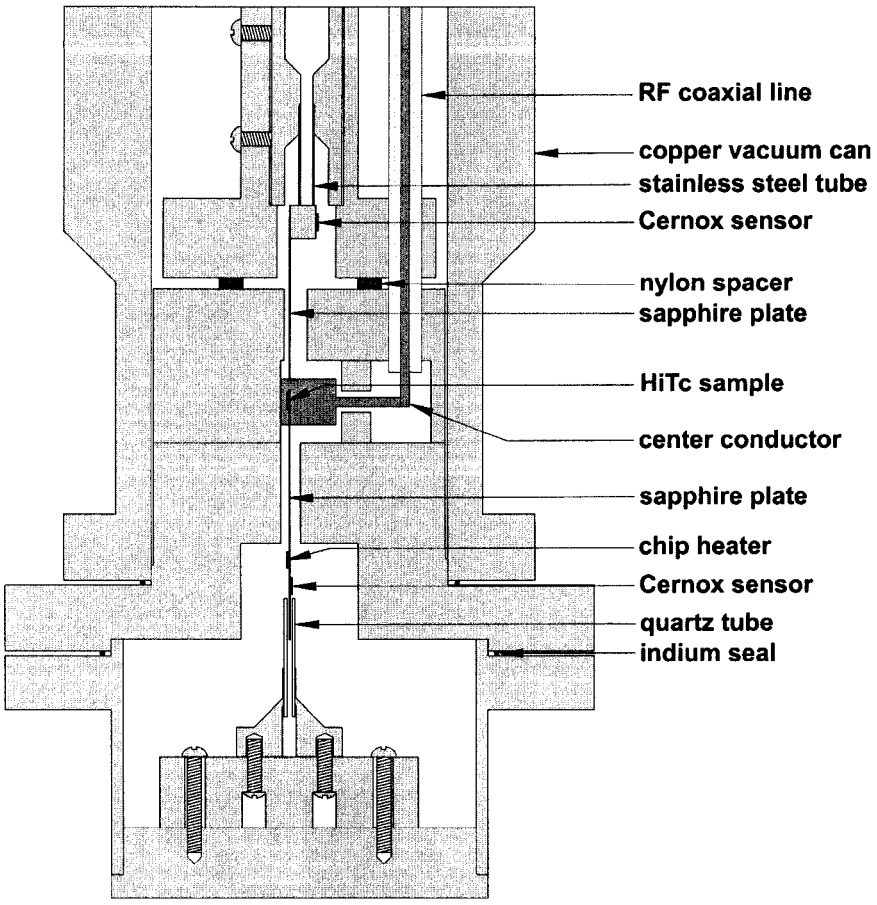


Figure 2.5: Scale drawing of the assembled apparatus indicating the details of the vacuum can and sample region. The alloy reference sample is not visible in this cut-away view.

One of the challenges of cryogenic microwave absorption measurements on small, low-loss samples is the design of the sample holder, which must measure and regulate the sample temperature, and yet contribute negligible dissipation compared to the sample. A widely used technique that satisfies these requirements is that of a sapphire hot-finger in vacuum [52], allowing the thermometry to be electromagnetically shielded from the microwave fields. In our apparatus, the sample holder is inserted through a hole that is beyond cut off for all operating frequencies. The ability to isolate the thermometry from the microwave radiation is critical to the success of the method; with infrared bolometric techniques, accounting for stray radiation is a serious concern. For ac calorimetric measurements, the design of the thermal stage is critical in setting the sensitivity of the system and we discuss the importance of its frequency response in Section 2.2.5. The experimental arrangement is shown schematically in Fig. 2.3. Here the sample under test is fixed on the end of a 100 $\mu$m thick sapphire plate using a tiny amount of vacuum grease [53]. The plate extends 17 mm from the sample to where it is epoxied into the bore of a 1.2 mm diameter quartz glass tube that acts as a thermal weak-link to the liquid helium bath. A

Cernox thermometer and a 1500 Ω surface-mount resistor used as a heater [54] are glued directly onto the sapphire plate with a very thin layer of Stycast 1266 epoxy [55], ensuring intimate thermal contact with the sapphire and hence the sample. We use 0.05 mm diameter NbTi superconducting electrical leads to the thermometer and heater for their very low thermal conductance, which is in parallel with the quartz weak-link. A photograph of the assembled hot-finger is shown in Fig. 2.4.

The microwave circuit is powered by a Hewlett-Packard 83630A synthesized sweeper (0.01-26.5 GHz) combined with either an 8347A (0.01-3.0 GHz) or 8349B (2-20 GHz) amplifier, generating up to 23 dBm of rf power across the spectrum. Approximately 2 m of 0.141" stainless steel coaxial line delivers power from the amplifier down the cryostat to the vacuum can. Inside the can, the coaxial line is soldered directly into the rectangular line as shown in Fig. 2.5. The r.m.s. microwave magnetic field amplitude at the samples is typically $\sim 10^{-2}$ oersteds, which generates $\sim \mu$K modulations in the sample-stage temperature for a typical high quality 1 mm$^2$ high-$T_c$ sample having a low frequency $R_s$ value of 1 $\mu\Omega$.

An assembled view of the low temperature apparatus including the microwave transmission line and the positions of the sample and reference holders is provided in Fig. 2.5. The sapphire plates that support both the test sample and reference sample are inserted through 4 mm diameter cut-off holes into the microwave magnetic field. The rectangular coaxial line consists of a centre conductor made from a 0.91 mm thick copper plate soldered at one end onto the centre conductor of the 0.141" semi-rigid coaxial line, and at the other end into the wall of the copper cavity that comprises the outer conductor of the transmission line. To minimize the rf power dissipated in the low temperature section of transmission line, the entire surface exposed to microwave radiation, including the final 15 cm of semi-rigid coaxial line, was coated with PbSn solder, which is superconducting below 7 K. During experiments, the vacuum can is completely immersed in a pumped liquid helium bath having a base temperature of 1.2 K.

The selection of a reference material for low-frequency work must be made carefully. Initially, we chose samples cut from commercially available stainless-steel shim stock, a common choice in infrared spectroscopy work. Calibration experiments produced erratic results which were eventually traced to the presence of anisotropic residual magnetism in the stainless steel. Subsequently, we produced our own reference material, choosing an Ag:Au alloy (70:30 at.% made from 99.99% pure starting materials), because it exhibits a very simple phase diagram that guarantees homogeneity [56]. By using an alloy, we ensure that the electrodynamics remain local at microwave frequencies, avoiding the potential complications arising from the anomalous skin effect [15]. Our sample was cut from a 93±5 $\mu$m thick foil having a measured residual dc resistivity value of $\rho$=5.28±0.3 $\mu\Omega$cm, constant below 20 K.

While the thermal stage for the reference sample is similar in design to that used for the sample under test, it uses a higher conductance stainless steel thermal weak-link (in place of the quartz tube), since the dissipation of the normal metal calibration sample is orders of magnitude larger than that of a typical superconducting sample. Because the apparatus was implemented as a retro-fit to an existing experiment, the

reference thermal stage had to be mounted directly onto the body of the transmission line structure. Although the cavity walls are superconducting to reduce their absorption, we use a nylon spacer to thermally isolate the base of the reference from the transmission line to avoid direct heating. The heat-sinking of the reference base to the helium bath is made using a separate copper braid that is not visible in Fig. 2.5.

As considered previously in our generic analysis, we operate the Cernox bolometer with a constant dc current bias, typically a few $\mu$A, provided by the series combination of an alkaline battery (1.5 V or 9 V) and bias resistor whose value is much larger than that of the Cernox sensor. With the helium bath under temperature regulation, the choice of bias power sets the temperature of the sample for a given experiment, with no other temperature control necessary. All electrical leads into the cryostat are shielded twisted pairs of insulated manganin wire, and true four-point resistance measurements are made on all sensors. The voltage signal appearing on the Cernox thermometer is amplified outside the cryostat by a carefully shielded and battery-powered circuit. We use a two-stage cascaded amplifier with one Analog Devices AD548 operational amplifier per stage, chosen because these are readily available, low-noise amplifiers. The dc level is nulled between stages to prevent saturation, and the total gain is $10^4$. The amplified signal, corresponding to the temperature modulation of the sample, is then demodulated with a Stanford Research Systems SR850 digital lock-in amplifier that is phase-locked to the rf-power amplitude modulation. There are two such systems; one for the sample and one for the reference measurements. The entire experiment is operated under computer control when collecting data.

### 2.2.4 Calibration

Two steps are necessary for an absolute calibration of the surface resistance of an unknown specimen from the measured temperature-rise data. The first is to calibrate the absolute power sensitivity of the sample and reference bolometer stages at the actual operating temperature and modulation frequency. This is achieved using the small *in-situ* heater to drive well-characterized heat pulses that mimic absorption by the sample, while at the same time measuring the corresponding temperature response. The second step requires the calibration of the magnetic field strength at the sample, at each frequency, using the known absorption of the reference sample. We exploit the fact that the metallic reference sample experiences the same incident microwave field $H_{rf}$ as the sample under test, guaranteed by conservation of magnetic flux. This ensures that taking the ratio of the absorbed power per unit surface area of each sample provides the ratio of the surface resistance values:

$$\frac{P_{abs}^{sam}}{P_{abs}^{ref}} = \frac{R_s^{sam} A^{sam}}{R_s^{ref} A^{ref}}. \tag{2.2}$$

The surface resistance of the unknown sample $R_s^{sam}(\omega)$ is then trivially found by multiplying the power absorption ratio, shown in Fig. 2.6, by $R_s(\omega)$ of the metallic reference sample calculated using the classical skin-effect formula $R_s(\omega) = \sqrt{\mu_o \omega \rho/2}$ where $\omega/2\pi$ is the frequency and $\mu_o$ is the permeability of free space. The raw power

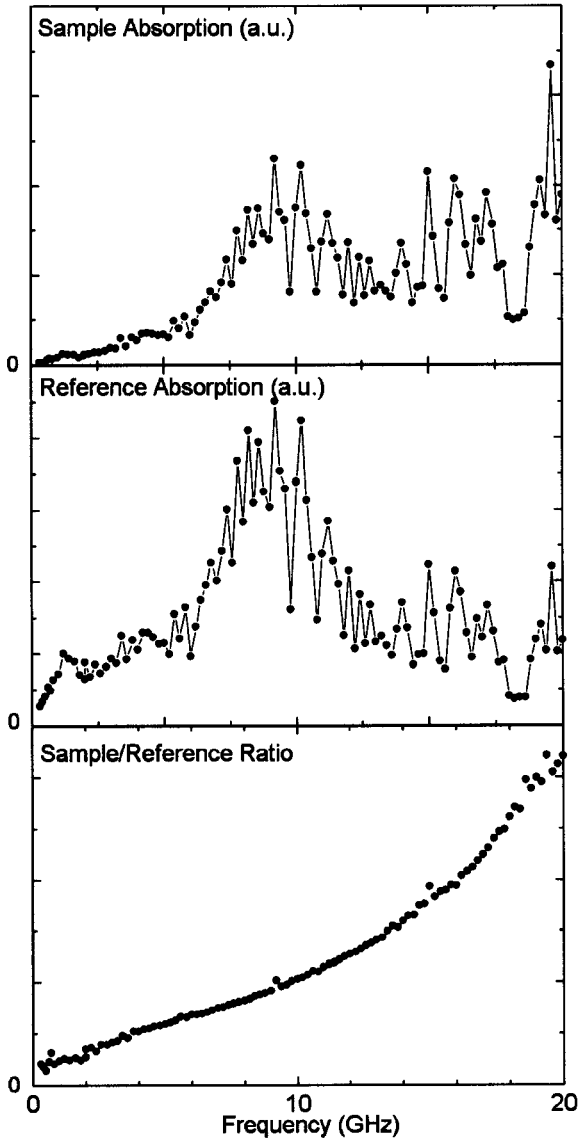


Figure 2.6: Raw absorption spectra corresponding to the temperature rise of the sample and the reference. Taking the ratio of the two signals corrects for the strong frequency dependence of $H_{rf}$ introduced by standing waves in the transmission line. The remaining frequency dependence of the ratio is due to the different $R_s(\omega)$ spectra of the sample and the reference.

absorption spectra, shown in the first two panels of Fig. 2.6, highlight the necessity of using a reference sample. The absorption spectra of the samples are completely masked by the large amplitude variations of $H_{rf}$ caused by the standing waves in the microwave circuit.

In practice, the small nonlinearities in the response of the thermal stages can lead to artificial deviations from a smooth ratio across the frequency scan. To minimize this effect, the software that automates the data collection is able to operate in

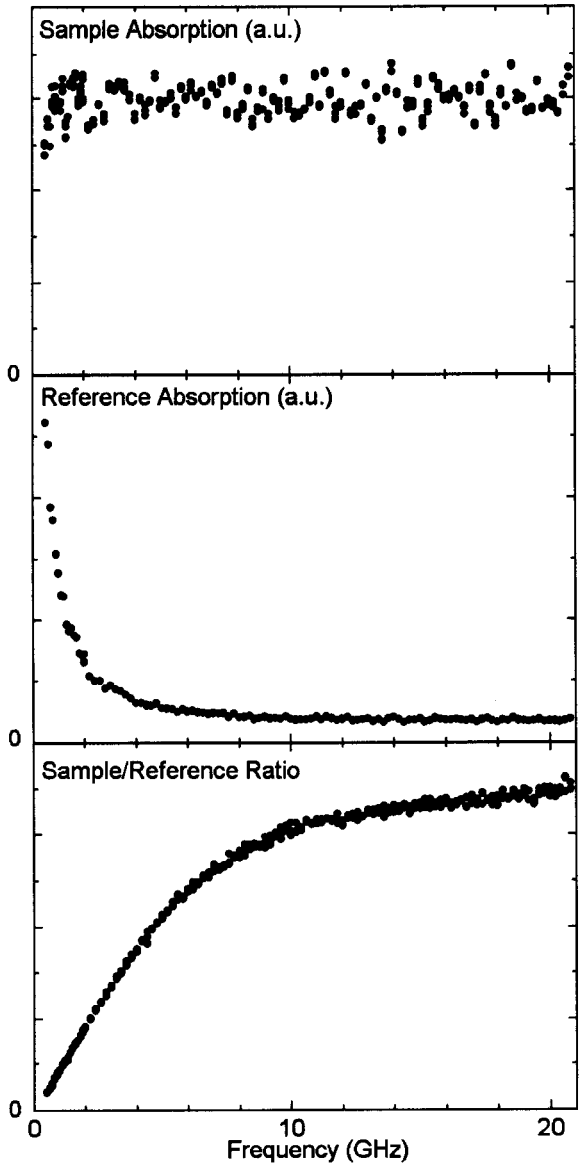


Figure 2.7: Absorption measurements for two samples having different $R_s(\omega)$ spectra similar to those shown in Fig. 2.6 except that here the microwave power has been adjusted during the scan to maintain an approximately fixed amplitude absorption signal on the sample stage.

a mode where the magnitude of the temperature oscillation of the sample is held approximately fixed by adjusting the rf power at each frequency to maintain a fixed response. An example of data taken in this fashion is provided in Fig. 2.7. The apparent scatter in the sample absorption data is a result of the 5% tolerance of the leveling routine designed to restrict the time spent on setting the rf power level, and maximize the time spent collecting data. For samples in which $R_s(\omega)$ has a monotonic frequency dependence, this is the method of choice since the rather large variations

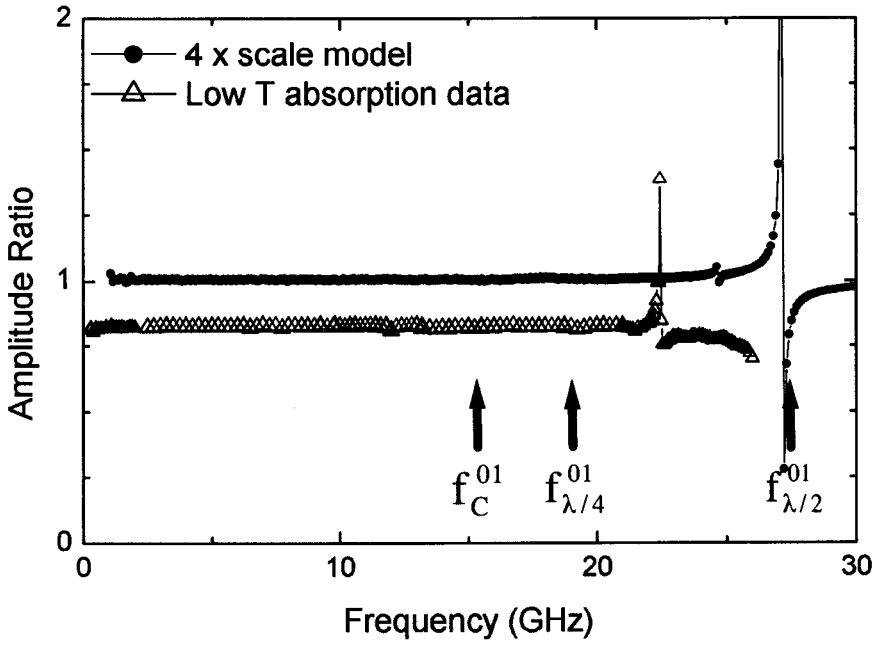


Figure 2.8: Ratio of the sample absorption to reference absorption for identical samples, compared to measurements of the field amplitude at equivalent positions in a ×4 scale model. (Frequencies for the scale model have been multiplied by a factor of 4 for the comparison.) The ratio technique is seen to break down with a sharp resonance in both cases. The origin of these resonances, which limit the useful frequency range of the apparatus, is discussed in detail in Section 2.2.6 and shown to be due to the presence of standing waves of the $TE_{01}$ waveguide mode. For this mode, the three arrows indicate: the cut-off frequency $f_C^{01} = 15.38$ GHz at which the mode is first free to propagate; its quarter-wave resonance frequency $f_{\lambda/4}^{01} = 19.11$ GHz, for open-circuit termination conditions; and the half-wave resonance frequency $f_{\lambda/2}^{01} = 27.4$ GHz, for short-circuit termination conditions. The $\lambda/4$ and $\lambda/2$ resonance frequencies bracket the observed resonances. The scale model, which has a large transition capacitance between circular and rectangular coax sections, is seen to fall at the high end of the range.

in power level evident in Fig. 2.6 are avoided.

An essential test of the method is to make a frequency-scanned measurement with identical samples mounted on the sample and the reference stages. The result should be a frequency-independent ratio across the spectrum, equal to unity for samples with the same surface area. In Fig. 2.8 we show such a measurement using two thin-platelet samples of our Ag:Au reference alloy, both at the base temperature of 1.2 K. The data reveal a ratio of 0.82 in the cryogenic apparatus, due to the fact that the centre conductor is inadvertently offset from centre by 0.1 mm in the termination region, intensifying the fields on one side relative to the other. This scale factor must

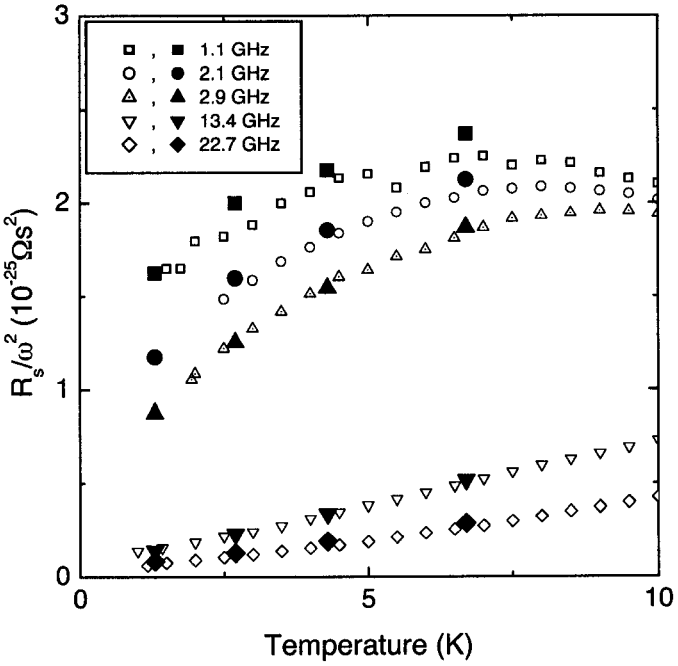


Figure 2.9: Comparison of measurements made on the same sample of $YBa_2Cu_3O_{6.52}$ using the broadband bolometric experiment (solid symbols) with those from five microwave resonators (open symbols). The agreement between methods is excellent. The data is plotted as $R_s(\omega)/\omega^2$ to remove the frequency dependence associated with superfluid screening.

be included in the calibration of all experimental data. The sharp resonance seen in the ratio at 22.5 GHz indicates the presence of a non-TEM electromagnetic mode in the sample cavity that breaks the symmetry in field strength between sample and reference positions. For our present design, this sets the upper frequency limit of operation.

At the low frequency end of the spectrum, the skin depth $\delta(\omega) = \sqrt{2\rho/\mu_o\omega}$ of the metal being measured can approach the physical dimensions of a small sample. When working with platelet samples, the smallest length scale is the thickness $t$, and the surface impedance expression must be modified to account for the partial transparency of the sample according to

$$Z_s(\omega) = \sqrt{i\mu_o\omega\rho}\tanh[t/2\delta(\omega)]. \tag{2.3}$$

This effect shows up clearly in our low frequency scans of the absorption in the Ag:Au reference alloy, demonstrated in Fig. 2.10. Here, data for the ratio when the two Ag:Au samples have different thickness values are shown to correspond very accurately to the calculated response. The values of $t$ required in the model agree very well with those measured using a calibrated optical microscope. By using an Ag:Au reference sample that is 93.5 $\mu$m thick, we ensure that thin-limit corrections are less than 1 % when working at frequencies above 45 MHz.

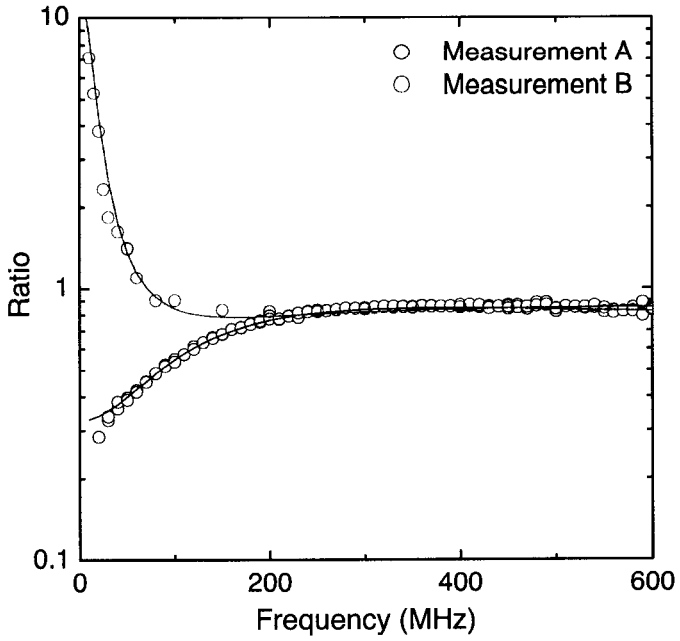


Figure 2.10: Low frequency absorption measurements made with samples of the Ag:Au reference alloy of different thickness on the sample and reference stages. The ratio of the sample to reference power absorptions per unit area is seen to deviate from the high frequency value of 0.82 as the skin depth at the measurement frequency approaches the half thickness of the thinner of the two samples. The lines on the plot show the predicted behaviour using the classical skin effect expression for the surface resistance of each sample, $R_s(\omega) = \mathrm{Re}\left\{\sqrt{i\mu_o\omega\rho}\tanh[t/2\delta(\omega)]\right\}$, with sample:reference thickness values of $23\mu$m:$31\mu$m and $80\mu$m:$31\mu$m in Measurements A and B respectively.

In an attempt to gain further insight into the field configurations in the transmission line, and to understand how the higher order waveguide modes limit the upper frequency range, we built a scale model of the setup having all dimensions larger than those of the cryogenic apparatus by a factor of four. For comparison, a frequency scan of the model structure is included in Fig. 2.8, using loop-probes in the positions of the samples. The data show that the non-TEM-mode resonance occurs at 27 GHz, considerably higher than in the low temperature experiment. It turns out that the breakdown of the sample-reference symmetry occurs not at the frequency at which higher order waveguide modes first propagate in our structure, but at the frequency at which they form a resonant standing wave. A full discussion of this is given in Section 2.2.6.

A number of other experimental tests were important to verify the proper operation of the system. Frequency scans without samples mounted on the sapphire stages confirmed that background absorption due to the sapphire and tiny amount of vacuum grease used to affix the samples is negligible — it is unmeasurable at low fre-

quency, and contributes no more than 2 $\mu\Omega$ to an $R_s$ measurement at 21 GHz. Scans without a sample also confirmed that no significant leakage heat current propagates to the thermometers directly from the microwave waveguide. The high thermal stability of the cryostat system is due in part to the very large effective heat capacity of the pumped 4 litre liquid-helium bath at 1.2 K. In addition, it is always important to make certain the temperature modulations of the samples are sufficiently small that the response of the thermal stages remains in the linear regime. Furthermore, measurements with the same sample located in different positions along the sapphire plate, with up to 0.5 mm displacement from the central location in the waveguide, confirmed that there is enough field homogeneity that our sample alignment procedure using an optical microscope is sufficient, and that samples of different sizes experience the same fields. To test the sensitivity of the absorption measurements to small misalignments of the sample, we performed a control experiment where a sample was measured, then deliberately misaligned by 2° so that the flat face of the sample was no longer parallel to the microwave field. (This is an amount much greater than the typical mounting error of less than 0.5°.) We could not resolve *any change* in surface resistance due to deliberate misalignment.

The central assumption of our method is that we measure the response of the surface of a broad, thin sample to a uniform applied microwave field. As a rule, geometric configurations involving sharp edges and corners are difficult to model, an issue that poses a very general problem in microwave engineering. In previous work, the magnetic field-dependent penetration depth $\lambda(T, H)$ was measured in a thin platelet sample before and after rounding the sharp edges of the crystal by mechanical polishing. While the measurements showed the sharp edges to be important to the *nonlinear* response, they had no influence on the low-field, linear response of the sample [57]. Since, within the surface impedance approximation, changes in the surface current profile affect the real ($\Delta\lambda$) and imaginary (power absorption) responses equally [38], we can conclude that the power absorption would have been equally unaffected. Given that the field geometry and crystal aspect ratios were comparable to the present experiment, we can be confident that the sharp edges of our platelet samples do not contribute significantly to the measurement.

A very convincing verification of the technique is provided by the ability to compare broadband $R_s(\omega, T)$ data with measurements of the *same sample* in five different high-Q microwave resonators. These experiments probe the temperature dependence of the absorption to high precision at a fixed microwave frequency: however, the determination of the *absolute* value of $R_s$ is limited to about 10% as discussed previously. The bolometric method has the advantage of being able to measure a true spectrum because the dominant uncertainty, the absolute surface resistance of the reference sample, enters as a scale factor that applies across the entire frequency and temperature range. The bolometry uncertainties are discussed more thoroughly in Section 2.3. Figure 2.9 shows that there is very good agreement of both the temperature and frequency dependence of the surface resistance as measured independently by the fixed-frequency and broadband experiments.

### 2.2.5 Frequency Response of Distributed Thermal Stage

We wish to calculate the temperature response of a simple thermal stage to a sinusoidal heat flux $P_{in} = \mathrm{Re}\left\{\tilde{P}_0 e^{i\omega t}\right\}$ superimposed on a static temperature gradient. We consider an arrangement where the isothermal sample stage has neglible thermal mass and is connected to base temperature by a weak thermal link with distributed heat capacity $c_V$ per unit volume. It is a straightforward extension to include an additional lumped heat capacity for the isothermal stage; once the lumped heat capacity dominates, the frequency response simplifies to that of a single-pole low-pass filter. However, in our case this is unnecessary: for electrodynamic measurements at low temperatures, the sample holder is required to be both electrically insulating and highly crystalline, and will therefore have very low heat capacity.

Here we consider the one-dimensional problem of a thin bar (the quartz tube in our apparatus) of length $L$ and cross-sectional area $A$, with one end fixed at a base temperature $T_0$ while the other end is heated by a heat flux due to sample power absorption. The propagation of a heat current $J_Q$ through the bar is constrained by the continuity equation $\partial J_Q/\partial x + c_V \partial T/\partial t = 0$ and the thermal conductivity $\kappa$ is defined by $J_Q = -\kappa \partial T/\partial x$. Together, these lead to the one-dimensional diffusion equation $\partial T/\partial t = \alpha \partial^2 T/\partial x^2$ where $\alpha = \kappa/c_V$ is the thermal diffusivity. Defining a complex thermal diffusion length $\tilde{\delta} = \sqrt{\alpha/i\omega}$, the time-dependent part of the temperature profile can be written

$$\Delta T(x,t) = \mathrm{Re}\left\{\tilde{T} e^{i\omega t} \sinh(x/\tilde{\delta})\right\} \tag{2.4}$$

where $\tilde{T}$ is fixed by the heat-flux boundary condition: $P_{in} = -\kappa A (\partial T/\partial x)|_{x=L}$. This completely determines the frequency-dependent temperature rise of the sample stage:

$$\Delta T(L,t) = \mathrm{Re}\left\{\frac{\tilde{P}_0}{\kappa A}\tilde{\delta} e^{i\omega t} \tanh(L/\tilde{\delta})\right\} \tag{2.5}$$

In the low frequency limit, the temperature rise reverts to the usual result:

$$\Delta T(L,t) = \frac{P_0 L}{\kappa A}\cos(\omega t), \tag{2.6}$$

where, without loss of generality, we have set the phase of the input heat flux to zero. In the high frequency limit, the thermal diffusion length becomes shorter than the weak link and the temperature rise is reduced, being given by:

$$\Delta T(L,t) = \frac{P_0 |\tilde{\delta}|}{\kappa A}\cos(\omega t - \pi/4) \tag{2.7}$$

where $|\tilde{\delta}| = \sqrt{\alpha/\omega}$. At finite frequencies, part of the heat flux is diverted into the distributed heat capacity of the thermal link. For a fixed input power (and hence fixed temperature *gradient* at the end of the thermal link) this leads to smaller temperature rises and a decreased sensitivity of the bolometric method. Clearly, the experimental

sensitivity of the bolometric method will be optimized by operating at or near to the low-frequency limit: $|\tilde{\delta}| > L$ or $\omega < \alpha/L^2$. However, the frequency at which the performance will be optimal will be a trade-off between the bolometer response and the excess bolometer or amplifier noise, which usually exhibits a $1/f$ type of spectrum. Therefore, a consideration of the thermal diffusivity and the dimensions of the weak-link must be part of any plan to increase the modulation frequency.

Fig. 2.11 shows the frequency response of the sample thermal stage in our apparatus when it was subjected to a sinusoidally varying heater power, normalized to the static response. Included in the figure are fits to the distributed-heat-capacity model, Eq. 2.5 and a single-pole low-pass filter response $\Delta T(\omega)/\Delta T(\omega = 0) = 1/\sqrt{1+\omega^2\tau^2}$. Although both curves fit the data well over most of the frequency range, the best-fit value of the time constant $\tau$ in the lumped-element model corresponds to a heat capacity much larger than the estimated heat capacity of the sapphire sample stage. Instead, the value obtained from the fit is approximately half the heat capacity of the quartz tube, indicating the correct physics is that of heat diffusion in a distributed thermal system.

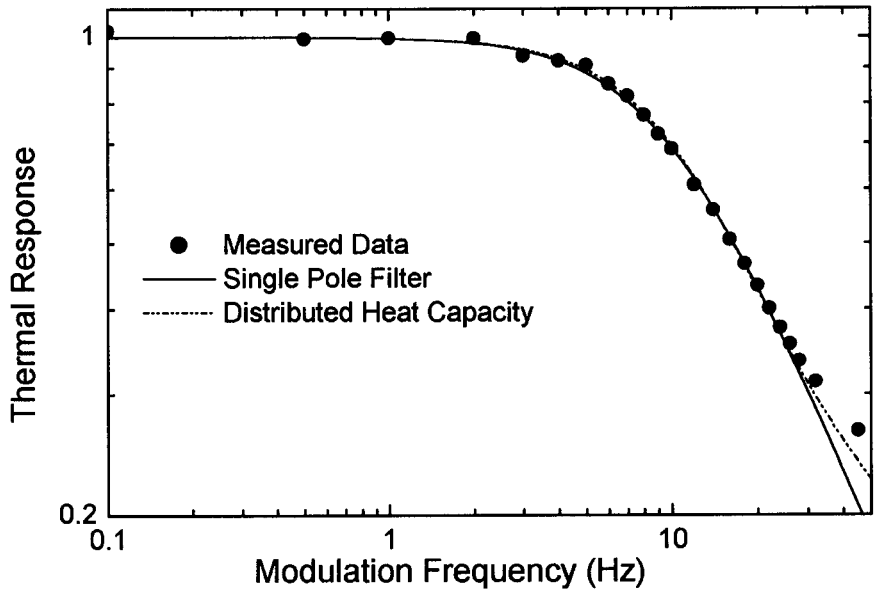


Figure 2.11: Low temperature ($T$ = 1.3 K) measurements of the dynamic thermal response of the quartz-tube bolometer platform. Curves on the plot show fits using lumped and distributed heat capacity models.

### 2.2.6 Design Strategy for Rectangular Coaxial Transmission Line

In optimizing a microwave transmission line for the bolometric measurement of surface resistance the guiding aims are: (a) to deliver microwave power efficiently to

the sample region, over as wide a frequency range as possible and with a well defined polarization; (b) to have regions of uniform microwave magnetic field at the sample and reference positions; and (c) at these positions, to have a fixed, frequency-independent ratio between the field strengths. These aims can be met by using an impedance-matched (50 Ω), single-mode coaxial line, with rectangular cross section and a broad, flat center conductor or septum, as shown in Fig. 2.12(i). In addition, the dimensions of the rectangular coaxial line should be chosen carefully, to prevent higher-order waveguide modes from entering the operating frequency range of the experiment, as these modes break the symmetry in field strength between sample and reference positions. This section outlines how to undertake the optimization.

A rectangular coaxial line, like any two-conductor line, supports a transverse electromagnetic (TEM) wave at all frequencies. Figure 2.12(ii) shows its electric and magnetic field configurations. The TEM mode has the desirable property that its magnetic fields lie in a plane perpendicular to the direction of propagation, forming closed loops around the centre conductor. Conservation of magnetic flux then leads to a fixed, frequency-independent relation between the fields on either side of the septum. These fields will also be quite homogeneous, as long as the height $C$ of the centre conductor is large compared to the gap $(B - D)/2$ between the centre and outer conductors. To deliver microwave power efficiently to the sample region the characteristic impedance of the TEM mode should be close to that of the cylindrical coaxial line used to bring microwaves into the cryostat. Gunston [58] has tabulated data on the impedance of rectangular coaxial line, and gives some useful approximate formulas. The following expression, due to Bräckelmann, is stated to be accurate to 10% for $D/B < 0.3$ and $C/A < 0.8$:

$$Z_0\sqrt{\epsilon_r} = 59.952 \ln\left(\frac{A+B}{C+D}\right)\Omega, \tag{2.8}$$

where $\epsilon_r$ is the relative permittivity of the dielectric filling the transmission line.

We now come to the question of what places an upper limit on the useful frequency range of the rectangular coaxial waveguide. At high frequencies our method, which incorporates an in-situ power meter, suffers a spectacular breakdown in the ratio of the relative strengths of the microwave magnetic fields at the sample and reference positions, as shown in Figure 2.8. This is caused by the presence of higher-order waveguide modes, which have different character from that of the TEM mode under the mid-plane reflection symmetries of the rectangular line. The waveguide modes with the lowest cut-off frequencies are the transverse electric modes $TE_{10}$ and $TE_{01}$, shown in Figures 2.12(iii) and 2.12(iv) respectively. These have the property that magnetic fields on opposite sides of the septum point in the *same* direction. The fields of the TEM mode, in contrast, are *antiparallel*, causing an admixture of TEM and TE modes to lack the important characteristic of equal field intensities at sample and reference positions. Particularly damaging is the $TE_{01}$ mode, which is not screened by the septum and has high field intensity in the vicinity of the sample and reference. In principal it is possible to avoid exciting the transverse electric modes by building a very symmetric transmission line. In practice, however, we find this

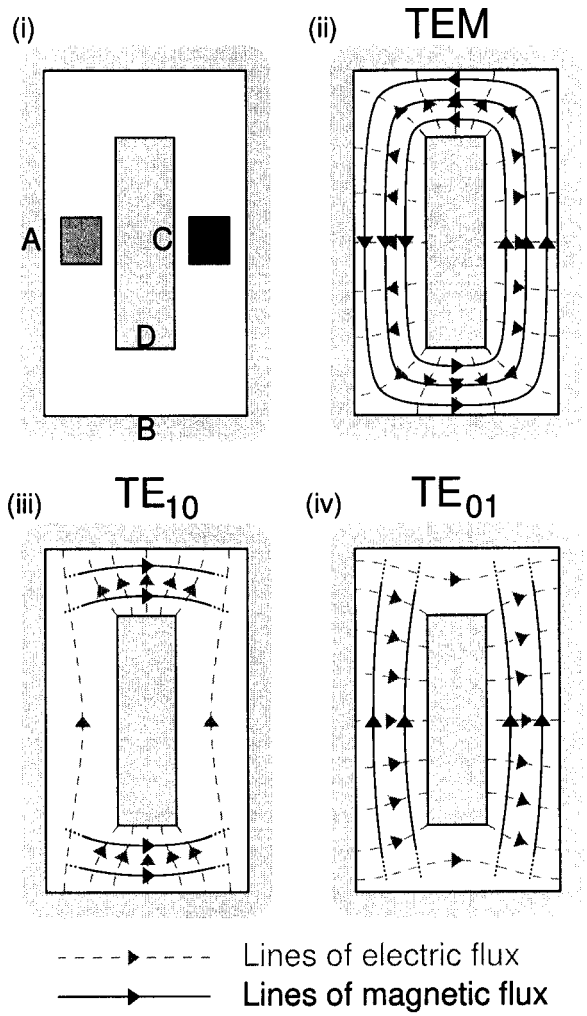


Figure 2.12: Cross sections of the rectangular coaxial transmission line: (i) physical layout of the transmission line showing dimensions $(A, B, C, D)$ of the inner and outer conductors, and sample and reference positions (shaded squares); (ii) fields of the TEM mode, showing how continuity of flux and a broad, flat inner conductor produce uniform, well polarized fields of equal intensity and opposite direction at the sample and reference positions; (iii) fields of the $TE_{10}$ mode; and (iv) fields of the $TE_{01}$ mode. (Magnetic fields of the transverse electric modes contain a component along the direction of propagation and do not form closed loops in the transverse plane.) It is clear that the $TE_{01}$ mode is most harmful to the operation of the broadband apparatus: its magnetic fields have high intensity at the sample and reference positions, and break the balance that otherwise exists in the TEM mode.

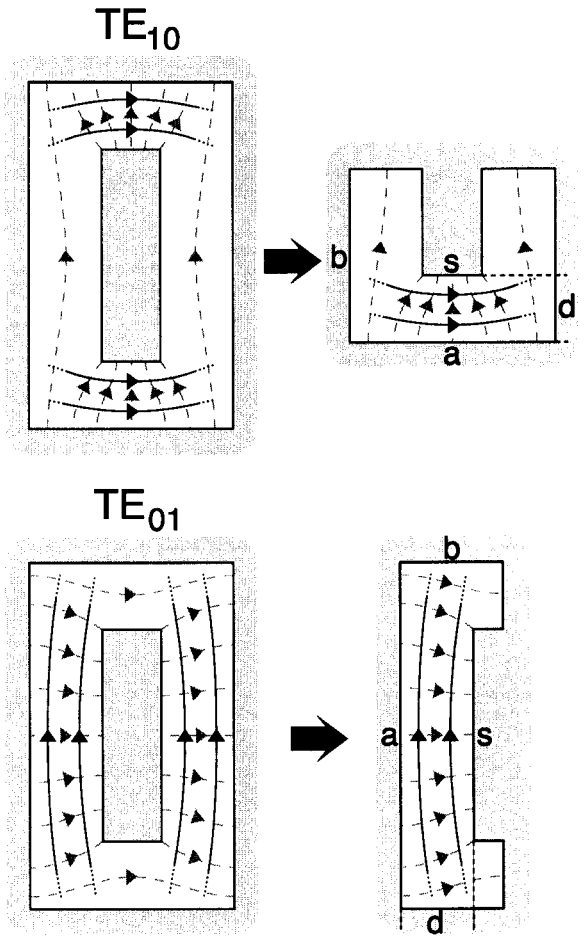


Figure 2.13: Conducting walls introduced along special electric equipotentials allow the waveguide modes of rectangular coaxial line to be mapped onto the fundamental mode of ridged waveguide, a problem extensively studied in the literature. The figures show the relabelling of dimensions in Pyle's notation [59] as $a, b, d$ and $s$.

to be impossible — sufficiently large symmetry-breaking perturbations are always present. Nevertheless, maintaining high symmetry is still desirable. A comparison of our results with calculations of the cut-off frequencies of the transverse electric modes shows that at frequencies where the higher order modes are free to propagate, they do not immediately cause a breakdown in field ratio: this only occurs when the transverse electric modes come into resonance. (This can be seen very clearly in Figure 2.8.) As a result, the range of operating frequency can be extended by as much as 50% just by shortening the final section of transmission line and carefully designing the transition between the cylindrical and rectangular sections.

Optimizing the range of single-mode operation of the rectangular transmission line requires a method for calculating the cut-off frequencies of the $TE_{10}$ and $TE_{01}$ modes. While waveguide modes in two-conductor rectangular transmission lines have

not been extensively studied, their field configurations can be mapped onto a more common geometry, that of ridged waveguide. Figure 2.13 shows how. Electric equipotentials run perpendicular to lines of electric flux, and special equipotentials, corresponding to local minima of the magnetic flux density, exist on the symmetry axes of the rectangle. A conducting wall can be introduced along these lines without disturbing the field distributions, thereby mapping each mode onto an equivalent ridged waveguide. Figure 2.13 illustrates the two different ways this is done, for the $TE_{10}$ and $TE_{01}$ modes respectively. A very early calculation of the cutoff frequency of ridged waveguide was carried out by Pyle [59] and is notable for its simplicity, generality and enduring accuracy when compared to more recent numerical methods [60]. Pyle's approach is to solve for the transverse resonance condition of the waveguide, which is equivalent to finding the cut-off frequency $\omega_c$. We have used this method in our design process, as it is easy to implement (involving only algebraic equations) and is accurate to several percent except when the septum becomes very thin. The length $\ell$ of the rectangular line, the cut-off frequency, and the discontinuity capacitance of the cylindrical-to-rectangular transition together determine the resonant frequencies $\omega_R$ of the transverse electric modes. There are two limiting cases, corresponding to open-circuit ($\ell = \lambda/4$) and short-circuit ($\ell = \lambda/2$) termination (where $\lambda = 2\pi/k$ is the wavelength along the guide), that follow from the waveguide dispersion relation.

$$\omega_R^2 = \omega_c^2 + c^2k^2 = \omega_c^2 + \frac{4c^2\pi^2}{\lambda^2} \tag{2.9}$$

$$= \omega_c^2 + \frac{c^2\pi^2}{4\ell^2} : \text{ open circuit} \tag{2.10}$$

$$= \omega_c^2 + \frac{c^2\pi^2}{\ell^2} : \text{ short circuit} \tag{2.11}$$

A high capacitance for the TE modes at the transition from cylindrical to rectangular coax is clearly favourable: it better approximates the short circuit termination condition and leads to resonant frequencies at the upper end of the range. This effect is responsible for the difference in resonant frequencies between the scale model and the actual apparatus seen in Figure 2.8. There is, however, a trade-off to be made: too large a transition capacitance for the TEM mode will result in most of the microwave power being reflected before it reaches the sample. The dimensions of the rectangular guide in our apparatus are $A = 8.90$ mm, $B = 4.06$ mm, $C = 4.95$ mm, $D = 0.91$ mm (see Fig. 2.12.i) and $\ell = 6.60$ mm. The cut-off frequencies for the $TE_{10}$ and $TE_{01}$ modes are calculated to be 19.68 GHz and 15.38 GHz respectively. The quarter wave-resonances would then occur at 22.72 GHz and 19.12 GHz, and the half wave resonances at 30.06 GHz and 27.44 GHz.

## 2.3 Performance

Figure 2.14 presents an example of high resolution broadband measurements of the frequency-dependent and temperature-dependent surface resistance of a superconducting sample. This particular data set is for $\hat{a}$-axis currents in a $YBa_2Cu_3O_{6.52}$

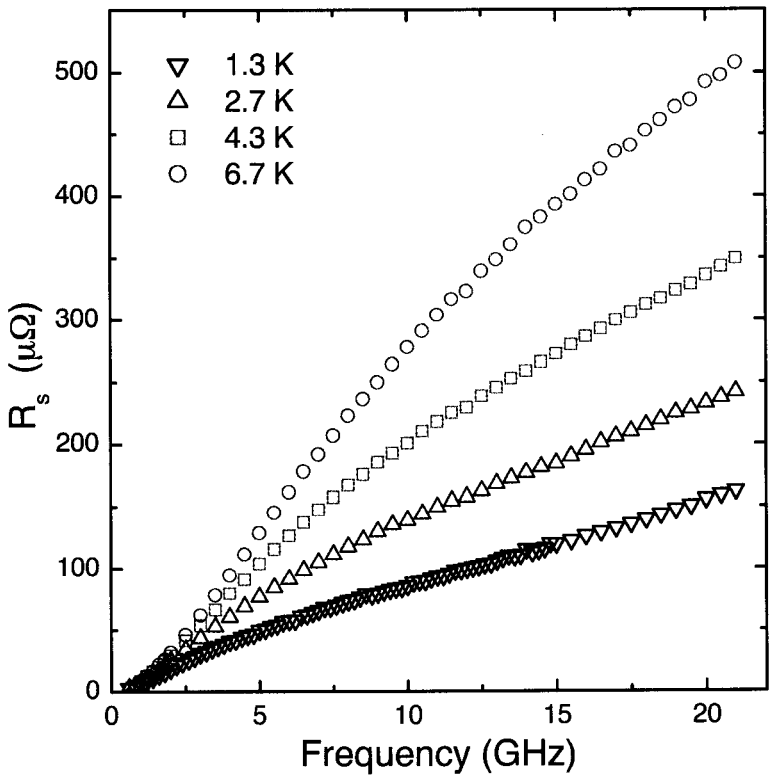


Figure 2.14: Broadband measurements of the microwave surface resistance spectrum of $YBa_2Cu_3O_{6.52}$ obtained with the bolometric apparatus below 10 K. The low frequency absorption approaches the resolution limit of the apparatus, while the upper frequency limit is imposed by the resonance in the microwave structure.

single crystal ($T_c$=56 K) having dimensions 1.25×0.96×0.010 mm$^3$. The data span the range 0.6-21 GHz, limited at high frequency by the resonance in the system, and at low frequency by the small dissipation of the sample, which approaches the resolution limit of the experiment. At 1 GHz, the values for the statistical r.m.s. uncertainty in surface resistance, $\delta R_s$, are about 0.2, 0.4, 0.6, and 1.3 $\mu\Omega$ for $T$ = 1.3, 2.7, 4.3, and 6.7 K respectively. Systematic contributions to the uncertainty enter as overall scale factors in the $R_s$ data and are attributed to an uncertainty in the DC resistivity of the thin Ag:Au alloy foil used as a reference sample (~5%), the surface area of the samples (~1%), and the absolute power sensitivity of the thermal stage (~1%).

The frequency dependence observed in $R_s(\omega)$ is mainly due to absorption by quasiparticles thermally excited from the superfluid condensate. The quantity of fundamental theoretical interest is the real part of the conductivity spectrum $\sigma_1(\omega)$, which must be extracted from the experimentally measured $R_s(\omega)$ data. A thorough discussion of the method we use to do this is given in the next section but, to first approximation, the shape of the conductivity spectrum can be found by dividing

$R_s(\omega)$ by a factor of $\omega^2$ to account for the screening of the applied field by the superfluid. With this in mind, it is immediately apparent why improving the sensitivity of the experiment is of the utmost importance. The low frequency region, where the power absorption becomes very small, is where the conductivity exhibits the strongest frequency dependence and is most important to measure accurately.

# Chapter 3

# Absolute Penetration Depth of $YBa_2Cu_3O_{6+y}$

The Meissner effect describes the way in which a superconductor screens an external magnetic field and is a defining feature of the superconducting state. Below the critical temperature, the London penetration depth $\lambda$ is the length scale over which fields are able to penetrate into the surface of a superconductor. As discussed in chapter 1, a measurement of $\lambda$ provides a rather direct measure of the superfluid phase stiffness $\rho_s \propto 1/\lambda^2$, or what is often referred to as superfluid density $n_s/m^* = 1/\mu_0 e^2 \lambda^2$, which can be a tensor quantity due to effects such as an anisotropic effective mass $m^*$. Because of the connection between $\lambda$ and the superfluid density, $\lambda$ enters as a control parameter in many physical properties of a superconductor. This is especially true when examining the electrodynamic properties, including microwave and infrared absorption, as well as some key properties of the vortex state in type-II superconductors such as the lower critical field $H_{C1}$ and the size of a vortex. A number of experimental techniques have been developed to measure both the absolute value and the temperature dependence of $\lambda$. While high precision methods have been developed for measuring the temperature dependence, the absolute value of $\lambda$ has proven to be particularly challenging. This is especially true if one wishes to measure the anisotropy of $\lambda$ that often exists in the unconventional superconductors.

This chapter presents a novel method for the measurement of the absolute value of the magnetic penetration depth in the $T \rightarrow 0$ limit in $YBa_2Cu_3O_{6+y}$. From the outset, the objective was to develop an approach that would not only yield an accurate absolute value of $\lambda$, but also meet the requirement of determining $\lambda$ for currents in the three major crystallographic directions. Envisioning a measurement method with sufficient sensitivity is especially challenging when one wants to work with samples where the intrinsic superconducting properties are best revealed, namely the small single crystals obtained by the self-flux crystal growth method. In this chapter, other means of measuring $\lambda$ will first be discussed and appraised before presenting the new microwave ESR method that we have developed recently at UBC.

This project has proven to be a rather large undertaking and highly collaborative in nature, benefitting from the efforts of many in the Bonn-Hardy lab at UBC. In particular, Ruixing Liang and Doug Bonn were responsible for the preparation and detwinning of the samples, Tami Pereg-Barnea and Richard Harris performed the calculation of the ESR spectrum from the crystal field Hamiltonian using Mathematica [61], Geoff Mullins measured $\Delta\lambda(T)$ at 1 GHz [62], Jake Bobowski polished samples prior to the EPMA analysis done by Mati Raudsepp in the Earth and Ocean Sciences Department at UBC and Walter Hardy first conceptualized the measurement

principal and provided important guidance throughout, including his extensive understanding of ESR/NMR spectroscopy. The author of this thesis performed all of the broadband microwave measurements in addition to the analysis of the experimental data along with Tami Pereg-Barnea and Richard Harris. The new results presented here are currently under review for publication [63].

## 3.1 Survey of Other Measurement Techniques

A wide variety of methods has been previously developed for the measurement of the absolute value of $\lambda$, but each has important drawbacks that must be considered when the objective is to obtain intrinsic $\lambda$ values in high quality single crystals. Here we will briefly consider two main classes of methods for examining a type-II superconductor that operate: (a) in the mixed state and (b) in the Meissner state. The techniques of class (a) take advantage of the fact that the penetration depth $\lambda$ controls the way in which magnetic fields decay as a function of distance from a vortex core in the mixed state. With a sufficiently sensitive means of probing the spatial variation of the field profile, $\lambda$ can be obtained. In class (b), the objective is to distinguish the small volume at the surface of a sample that remains field-penetrated from the volume that is screened by the superfluid when the sample is cooled deep into the superconducting state.

The first example of a method from class (a) is Muon spin rotation ($\mu SR$) which has been widely used to examine the cuprate superconductors. Here, spin-polarized muons having an average lifetime of 2.2 $\mu$s are implanted into a sample and the monitoring of their decay yields information about the local field environment [64]. This is made possible by the fact that the positron that is emitted when the implanted muon decays is ejected preferentially *along the direction of the muon spin.* Since the precession rate of the muon spin is proportional to the local field, a time-resolved measurement of the spatial distribution of the positron emission yields the field distribution in the sample. The challenge then becomes modeling the details of the spatially inhomogeneous magnetic field associated with the vortex state where $\lambda$ enters as a fitting parameter, as described in the review article by Soneir *et al.* [64]. $\mu SR$ measurements have the advantage that they are a bulk probe, and thus are not highly sensitive to surface defects. One drawback is that the measurement is insensitive to the in-plane anisotropy of $\lambda$, and only the geometric mean is obtained $\lambda_{ab} = (\lambda_a \lambda_b)^{1/2}$. Furthermore, care must be taken when working in the mixed state that $\lambda$ is not altered by the non-linear and non-local effects that have been shown to occur at the relatively high fields often used in the experiment [64]. This will be discussed further when the new ESR measurements are compared with existing $\mu SR$ data in Section 3.8.

Another example of a method from class (a) is the scanning Hall probe microscope which has been used to image individual vortices down to the submicron scale [65, 66]. At present, the Hall probe has a size of $0.5 \times 0.5$ $\mu m^2$, which is reduced somewhat by the depletion region in the semiconducting material when in operation. An absolute value of $\lambda$ can be inferred by modeling the field distribution above the vortex. Since

the spatial field inhomogeneity is high in the region where the measurement is made, the value of $\lambda$ that is obtained depends sensitively on knowing the position of the Hall sensor. This method has been used to measure the rather large values of $\lambda$ for underdoped $YBa_2Cu_3O_{6+y}$, however it is presently limited to a spatial resolution of $\sim$0.5 $\mu$m and hence cannot measure the smaller $\lambda$ values that occur at higher doping levels. This is due in part to the size of the Hall sensor itself, and in part to the uncertainty in the distance of the sensor above the vortex of interest.

Techniques belonging to class (b) measure the magnetic flux exclusion from a sample in the Meissner state, essentially by measuring the magnetic susceptibility at DC, radio or microwave frequencies [19, 67, 68]. These methods are widely used to precisely determine the temperature dependence $\Delta\lambda(T) = \lambda(T) - \lambda(T_o)$ relative to a base temperature $T_o$. However, a measurement of the absolute value amounts to a comparison between the physical volume of the sample and a susceptibility determination of the volume that is field-free, the difference being the small volume at the surface that is penetrated by the field. Such a measurement is most sensitive if the ratio of surface area to volume is large, which can be achieved by working with powders or films. This also has drawbacks in that difficulties with aligning powders and modeling the shape and size distribution of grains introduce substantial uncertainties in the absolute value of $\lambda$ [69]. For a macroscopic, high quality crystal of a cuprate superconductor, it is completely impractical to measure sample dimensions precisely enough to achieve an absolute measurement of $\lambda$ this way, except in geometries dominated by the very large values of $\lambda$ for screening currents running in the $\hat{c}$-direction.

Another means of accessing $\lambda$ absolutely in the Meissner state is through measurements of the far infrared reflectivity (FIR) [70]. Here, the reflectivity of a sample is measured in an interferometer over a wide frequency range, but no information on the phase is obtained. Through use of the Kramers–Krönig transform, with suitable extrapolations outside of the measured frequency range, the phase can be obtained from the reflectivity [71]. This in turn allows one to obtain the complex conductivity $\sigma_1(\omega)+i\sigma_2(\omega)$. Since $\sigma_2 = (\mu_o\omega\lambda^2)^{-1}$, an extrapolation of the quantity $[\mu_o\omega\sigma_2(\omega)]^{-1/2}$ to $\omega \rightarrow 0$ yields an estimate of $\lambda$. For this method to be accurate, the measurement must be made at low temperature where there are few quasiparticles to contribute to the measurement. If this is not the case, then the measured value of $\lambda$ may not correspond to the true London value as a result of the additional screening capability of the quasiparticles. By using polarized light it is possible to measure the optical properties along all of the principal axes and thus obtain the full anisotropy of $\lambda$ [72, 73]. Such infrared determinations of the absolute value of $\lambda$ at low temperature have been combined with microwave measurements of $\Delta\lambda(T)$ to produce the anisotropic $1/\lambda^2(T)$ in $YBa_2Cu_3O_{6+y}$ at y=0.60 and 0.95 [74], but it would be far preferable to have a more direct microwave measurement that gives the absolute value of $\lambda$, measured *on the same sample* as that used to determine the temperature dependence.

A technique used more recently by Prozorov *et al.* involves coating a single crystal of the superconductor of interest with a carefully characterized thin film of Al ($T_c^{Al} \sim$

1.2 K) which has a well-known value of $\lambda$ [75]. A tunnel-diode oscillator structure, held in close proximity to the sample, is used to measure the change in $\lambda$ to high precision. The Al coating serves as a calibration that allows a measured change in $\lambda$ upon warming above $T_c^{Al}$ to be related to the absolute value of $\lambda$ in the unknown crystal. This particular apparatus runs circular screening currents in the $\widehat{ab}$-plane and therefore measures an average of $\lambda_a$ and $\lambda_b$.

Lastly and briefly thin film techniques are mentioned. The chemical complexity of the oxide superconductors and their sensitivity to disorder means that using thin films to study the intrinsic properties must be done with care. With this in mind, very direct measurements of $\lambda$ have been achieved by measuring the transmission of low frequency fields through very thin films using mutual inductance techniques. The penetration depth enters as a parameter in a model for the screening capability of the thin film. While this is a very sensitive method that can yield absolute values of $\lambda$ with quite good precision, its chief drawbacks are the need to work with films (which tend to be defected and must be much thinner than $\lambda$) and the difficulty with measuring the anisotropy [76].

## 3.2 Measurement principal

This chapter describes a new method of measuring $\lambda(T \rightarrow 0)$ absolutely in single crystals of $YBa_2Cu_3O_{6+y}$ using a microwave technique that directly probes the volume of the sample penetrated by an external microwave field in the Meissner state (see Fig. 3.1). This has been achieved by slightly modifying the samples so that they contain an indicator whose microwave response directly reveals the field-penetrated volume of the sample, while the rest of the sample contributes no signal to the measurement. Specifically, a randomly distributed low concentration of magnetic moments ($Gd^{3+}$ ions) is doped into the superconductor to be used as an indicator of field penetration. The concentration is kept low enough that there is a minimal affect on the intrinsic transport properties of the material. The magnetic moments serve as a non-interacting spin system whose electron spin resonance (ESR) spectrum is a sum of one-particle ESR transitions. The energy levels of each single spin are determined by the crystallographic environment, *i.e.* the charge distribution around the magnetic ion, and the resulting susceptibility of the sample is that of a single spin multiplied by the number of spins that participate in the ESR process. If the moments are evenly distributed throughout the sample, the number of spins that participate in the process is proportional to the fraction of the sample's volume that is exposed to the field, *i.e.* the volume within a penetration depth of the surface. In order to count the number of spins exposed, the zero field ESR absorption spectrum is measured. This is done using the broadband spectrometer described in Chapter 2 in which the microwave frequency magnetic field is applied perpendicularly to the principal spin axis. The microwave field acts as a small perturbation that causes ESR transitions between energy levels.

In the rest of this chapter, the details of the sample preparation are provided as well as a description of how the ESR signal is separated from the intrinsic mi-

crowave response of the superconductor. Then the discussion turns to the theoretical calculation of the ESR spectrum using an effective crystal field Hamiltonian, a necessary prerequisite for extracting $\lambda$. It turns out that the issue of oxygen ordering in the CuO chains of the $YBa_2Cu_3O_{6+y}$ samples is very important for understanding the ESR response, and we are able to examine this in a very sensitive manner. Finally, the measured values for $\lambda$ in all three crystallographic directions for three distinct doping levels in the $YBa_2Cu_3O_{6+y}$ system are summarized and compared to measurements made by other groups using the techniques discussed in Section 3.1.

## 3.3 Sample Preparation and Experimental Technique

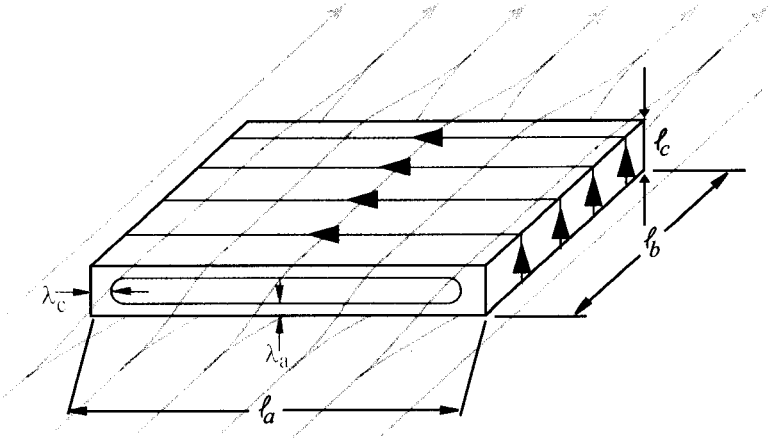


Figure 3.1: Schematic drawing of a platelet sample of a superconductor having an anisotropic penetration depth $\lambda$ in a uniform applied microwave magnetic field $H_{rf}$. In the above picture, the field penetrates a volume determined by $\lambda_a$ and $\lambda_c$ and the crystal dimensions $\ell_a$ and $\ell_c$, but contains no contribution from $\lambda_b$. By combining measurements where we rotate and cleave the crystal, we are able to determine values of $\lambda$ for all three crystallographic directions.

The objective of this work is to provide accurate measurements of the intrinsic absolute value of the magnetic penetration depth in the limit $T \rightarrow 0$. As discussed in Chapter 1, it is well-known that impurity doping can have a strong influence on the low energy density of states in a $d$-wave superconductor [21, 22], and for the present work care must be taken to ensure that the introduction of the spin-probe impurity does not alter $\lambda(T \rightarrow 0)$. This constrains the Gd concentration x, but conversely we wish to maximize the amplitude of the ESR response, which scales as x. We have found a good compromise at a nominal value of x$\approx$ 1% which results in an ESR spectrum that we can easily resolve and yet does not significantly alter the intrinsic low temperature properties of the material.

In $Gd_xY_{1-x}Ba_2Cu_3O_{6+y}$, the dopant $Gd^{3+}$ ion substitutes for the $Y^{3+}$ ion which is sandwiched between the two $CuO_2$ planes in the $YBa_2Cu_3O_{6+y}$ unit cell (refer to Fig. 1.4). The energy cost for cross-substitution of the Gd on the Ba site is prohibitive and such cation substitution occurs only for the lighter and larger members of the rare earth series. The ESR spectrum is determined completely by the crystal field environment of the $Gd^{3+}$ ion and therefore knowing that there is only one site for substitution means that changes in the ESR spectrum from sample-to-sample can only be due to changes of the oxygen order in the CuO chains. Another important feature of substitution on the Y site is that the Gd impurities are expected to be weak (Born) limit quasiparticle scattering centers as was found to be the case for $Ca^{2+}$ substitution on the same site [74]. Born scatterers have little effect on the superfluid density in the low temperature limit. This is in contrast, for instance, to the case of the non-magnetic impurity $Zn^{2+}$ which substitutes *into* the $CuO_2$ plane, and is known to be strongly pair-breaking.

The $Gd_xY_{1-x}Ba_2Cu_3O_{6+y}$ samples were grown using the self-flux method in $BaZrO_3$ crucibles as described in Section 1.5. The starting materials had the nominal concentration of Gd ions set by the ratio of oxide precursor substitution $Gd_2O_3$:$Y_2O_3$. The as-grown platelet single crystals were mechanically detwinned, annealed in flowing oxygen to set the oxygen content, sealed in a quartz capsule with a much larger sample for a homogenization anneal, and then given a final anneal at lower temperature for oxygen ordering. The annealing parameters have been previously published for the slightly overdoped (nearly full CuO chains, y=0.993) [34] and ortho-II ordered (alternating full and empty chains, y=0.52) [35] crystals. Other ordered phases at intermediate doping were also produced with larger chain-ordered superlattices, namely ortho-III [77] and ortho-VIII [78]. Crystals at these doping levels were made using procedures very similar to that used to produce the ortho-II samples, however the initial temperatures for setting the oxygen content were different (668 °C for ortho-VIII and 609 °C for ortho-III) as were the final low temperature annealing temperatures used to establish oxygen ordering in the CuO chain layers (35 °C for ortho-VIII (y=0.67) order and 60 °C for ortho-III (y=0.77) order).

A critical parameter in the analysis of the data is the absolute concentration of Gd ions x, which was measured absolutely by electron-probe micro-analysis (EPMA). For the present study, we found it to be important that each $Gd_xY_{1-x}Ba_2Cu_3O_{6+y}$ crystal was examined individually. Because the sample must be embedded in epoxy and subsequently polished to provide a parallel surface for EPMA, the analysis was done after all microwave measurements were completed. For a nominal Gd concentration of x= 1% in the growth flux, the resulting concentration in the crystals was found to vary from x= 1.05(.06)% to x= 1.37(.12)%. At least 10 locations were measured on each crystal surface as a means of ensuring that the stoichiometry was homogeneous. In all but one sample, the uniformity was within the statistical limitations of the measurement. For one sample it was necessary to examine 54 different locations covering the crystal surface to map out and take account of a small region, approximately 5% of the total surface, having an elevated Gd concentration of x= 1.50(.08)%. Measurements on the cut edges of a 100 $\mu m$ thick sample confirmed that there was no

gradient through the thickness of the sample. If the Gd concentration in the melt were to drift with time during the crystal growth, the resulting Gd gradient in the crystal would be problematic for the following analysis.

The low temperature broadband microwave absorption spectrum was measured using the spectrometer described in Chapter 2. In order to understand how the ESR signal is isolated from the measured data, recall the simple expressions of Eq. 1.14 that relate the surface resistance and reactance to the conductivity:

$$\begin{aligned} \mathrm{R}_s(\omega,T) &\simeq \frac{1}{2}\mu_o^2\omega^2\lambda^3(T)\sigma_1(\omega,T), \\ \mathrm{X}_s(\omega,T) &\simeq \sqrt{\frac{\mu_o\omega}{\sigma_2}} = \mu_o\omega\lambda(T). \end{aligned} \tag{3.1}$$

Note the appearance of $\lambda$ in both of the above expressions that highlights its important role in determining the absolute conductivity from measurements of $R_s$ and $X_s$. At low temperatures, absorption in a superconductor is due to quasiparticles thermally excited from the condensate, and the study of the quasiparticle conductivity spectrum $\sigma_1(\omega,T)$ is an important subject in its own right and is the subject of Chapter 4 of this dissertation. For the present case of a superconductor containing a dilute concentration of magnetic impurities, the imaginary part of the magnetic susceptibility, $\chi''$, provides another mechanism for power absorption.

Formally, the magnetic response can be included by a modification of the vacuum permeability $\mu_o$ in Eq. 1.13 to include a dimensionless complex susceptibility $\chi$, written as $\mu_o \rightarrow \mu = \mu_o(1+\chi'-\mathrm{i}\chi'')$. For the case of a sufficiently low concentration of magnetic impurities, $\chi', \chi'' \ll 1$, and the apparent surface impedance expressions can then be rewritten as

$$\begin{aligned} \mathrm{R}_s^{app}(\omega,T) &\simeq \frac{1}{2}\mu_o^2\omega^2\lambda^3(T)\left[\sigma_1(\omega,T)+\frac{\chi''(\omega,T)}{\mu_o\omega\lambda^2(T)}\right], \\ \mathrm{X}_s^{app}(\omega,T) &\simeq \mu_o\omega\lambda(T)\sqrt{1+\chi'(\omega,T)}. \end{aligned} \tag{3.2}$$

Thus, a frequency scanned measurement of the power absorption will provide an apparent surface resistance with two separate contributions; one from the quasiparticle conductivity $\sigma_1(\omega,T)$ and one from the ESR spectrum contained in $\chi''(\omega,T)$.

Equation 3.2 reveals that a measurement of the surface reactance will contain a contribution from $\chi'(\omega,T)$ in addition to probing $\lambda(T)$. This is evident in the comparison of our measurements of $\Delta\lambda(T)$ in pure and Gd doped $YBa_2Cu_3O_{6.95}$ and $YBa_2Cu_3O_{6.99}$, presented in Fig. 3.2. In fact, at the outset of this work we considered the possibility of fitting the curvature arising from $\chi'(T)$ in a low frequency measurement of $\Delta\lambda(T)$ as a means of extracting the absolute value of $\lambda$. However, it was decided that this method was not practical as it lacked the necessary sensitivity and also required knowing $\chi'(\omega,T)$ *a priori*. A further complication to this approach is that it has been well-established that a variety of paramagnetic impurities can introduce a low temperature upturn in a low frequency $\Delta\lambda(T)$ measurement [79], which would produce systematic errors in the extraction of an absolute value of $\lambda$.

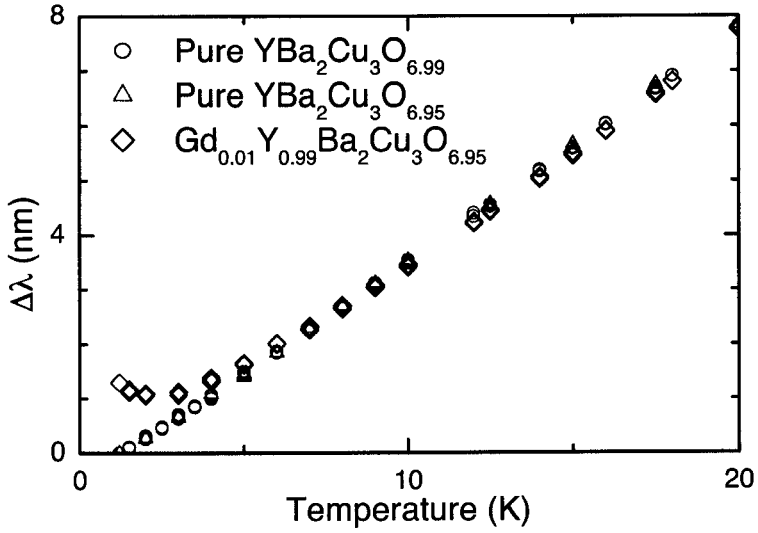


Figure 3.2: Measurements of the temperature-dependent change in apparent magnetic penetration depth, $\Delta\lambda(T)$, performed via cavity perturbation in a loop-gap resonator operating at 954 MHz [62]. A comparison between $\hat{a}$-axis measurements on single crystal samples with and without 1% Gd substituted for Y demonstrates that only below a temperature of $\sim$7 K does the contribution from the real part of the susceptibility $\chi'(\omega, T)$ contribute to the measurement as an upturn in the apparent penetration depth. Above this temperature, the intrinsic linear dependence of $\Delta\lambda(T)$ of a clean $d$-wave superconductor is recovered. While the data for the $Gd_xY_{1-x}Ba_2Cu_3O_{6+y}$ sample does show a non-monotonic temperature dependence that would be difficult to account for by impurity pair-breaking, the possibility of such a contribution cannot be entirely ruled out. However, an estimate of the contribution to $\Delta\lambda(1\ GHz, T)$ is within a factor of two of that expected from the measured ESR spectrum [62].

Fortunately, the broadband spectroscopy apparatus provides a means of accessing the ESR spectrum in much greater detail. Figure 3.3 shows a measurement of $R_s^{app}(\omega)$ from 0.5 GHz to 21 GHz at 1.3 Kelvin for a $Gd_{0.01}Y_{0.99}Ba_2Cu_3O_{6.99}$ sample. The quasiparticle absorption spectrum is known to be a slowly varying, monotonically increasing function of frequency, and the sharp ESR absorption lines ($\Delta f < 0.5$ GHz) are superposed. We will show in Chapter 4 that the low temperature microwave conductivity $\sigma_1(\omega, T)$ extracted from measurements of $R_s(\omega, T)$ can be interpreted as that of weak-limit quasiparticle scattering from impurities, and here we attribute the small changes in the spectrum of Fig. 3.3 to a slight increase in scattering due to the increased density of out-of-plane defects in the Gd doped samples. In order to separate the ESR contribution from the quasiparticle conductivity, we fit to the smooth background away from the ESR peaks using a second order polynomial, shown as a solid line in Fig. 3.3. After subtracting the polynomial, the remaining quantity

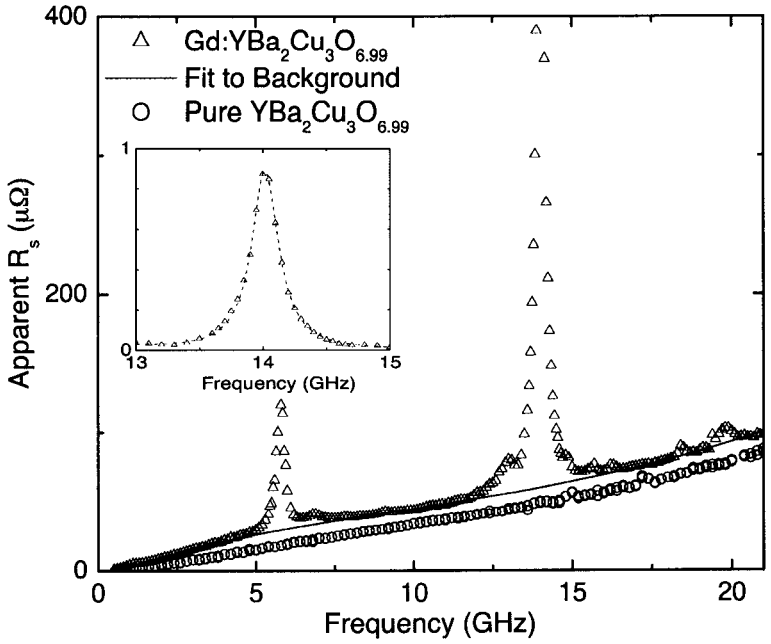


Figure 3.3: Broadband microwave absorption measurement of a $Gd_{0.01}Y_{0.99}Ba_2Cu_3O_{6.99}$ single crystal sample at 1.3 K. The broad, smooth background is due to quasiparticle absorption and the sharp lines are due to ESR transitions. The smooth line is a polynomial fit to the background away from the ESR peaks, and is seen to be similar to a sample without Gd. The inset shows that the main ESR transition at 14.05 GHz is very well described by a Lorentzian lineshape, shown as a dashed line.

is equal to $\frac{1}{2}\mu_o\omega\lambda\chi''(\omega)$ (from Eq. 3.2). In the subsequent section, we discuss the calculation of the quantity $\chi''(\omega)$ from the effective spin Hamiltonian. With the theoretical curve for the susceptibility of one Gd spin in hand, we are able to fit to the experimentally determined quantity with an overall multiplicative fit parameter $\lambda$.

## 3.4 Extracting anisotropic $\lambda$ values from multiple measurements

As mentioned previously, $YBa_2Cu_3O_{6+y}$ single crystals grow naturally as platelets having broad $\hat{a}\hat{b}$-plane crystal faces and thin $\hat{c}$-axis dimensions. All of our microwave measurements involve a uniform radio frequency magnetic field $H_{rf}$ applied parallel to the broad face of the crystal in order to minimize the effects of demagnetization, as shown schematically in Fig. 3.1. Since the crystal $\hat{c}$-axis is the principal spin axis of the Gd ions, the ESR response is maximized in this configuration. The number of Gd spins that are exposed to the microwave field is governed by the effective penetration depth $\lambda_{eff}$ and, for our geometry, will always contain contributions from $\lambda_a$ or $\lambda_b$

and $\lambda_c$. In the cuprates, the two-dimensionality of the $CuO_2$ planes results in a large anisotropy in the penetration depth: $\lambda_c \gg \lambda_a, \lambda_b$ for all doping levels. In practice, this means that despite working with thin crystals having the in-plane dimension $\ell_{a,b} \gtrsim 10\ell_c$, the $\hat{c}$-axis contribution to $\lambda_{eff}$ can be large. In some cases it was also necessary to account for a small fraction $t$ of the crystal which remained twinned (14% at most), introducing the third component of $\lambda$ into the measurement. Since $\lambda$ is small compared to any crystal dimension, it suffices to use a simple linearized relation for $\lambda_{eff}$,

$$\lambda_{eff} = \frac{\ell_p((1-t)\lambda_a + t\lambda_b) + \ell_c\lambda_c}{\ell_p + \ell_c} \tag{3.3}$$

where $\ell_p$ is the in-plane crystal dimension parallel to the flow of diamagnetic screening currents (the geometry is that of Fig. 3.1). Each component of $\lambda$ can be isolated by combining measurements performed on the *same crystal* but with its geometry altered in a controlled manner as attained by rotating and cleaving the crystal.

$YBa_2Cu_3O_{6+y}$ single crystals have strong natural cleave planes perpendicular to both the [100] and [010] directions. Using this fact, previous studies of the temperature dependence of $\lambda$ have been successful at separating the out-of-plane response from the in-plane response by measuring a sample, cleaving it $N$ times, and then repeating the measurement with all of the pieces together. The second measurement contains the same in-plane contribution, but has the $\hat{c}$-axis contribution enhanced by a factor of $N$ [46]. For practical reasons, in the present work it was not possible to measure all of the crystal fragments together following cleaving in all cases, and instead we successively measured each crystal after reducing the in-plane area. The $\hat{c}$-axis thickness $\ell_c$ of the crystal was unchanged for all measurements, but the measurement of $\ell_c$ retains the largest relative uncertainty because $\ell_c \ll \ell_{ab}$. Since $\lambda_c$ is also rather large, care must be taken when combining measurements in order to minimize the impact of the large relative uncertainty in the quantity $\ell_c\lambda_c$ in Eq. 3.3. The method we use here is to combine measurements of the same crystal in both $\hat{a}$-axis and $\hat{b}$-axis directions before and after cleaving to change the crystal's aspect ratio by approximately 50%, providing an over-determination of the three unknown $\lambda$ values. For example, before and after cleaving the sample we measure

$$\lambda^a_{eff} = \frac{a((1-t)\lambda_a + t\lambda_b) + c\lambda_c}{a+c} \tag{3.4}$$

$$\lambda^b_{eff} = \frac{b(t\lambda_a + (1-t)\lambda_b) + c\lambda_c}{b+c} \tag{3.5}$$

which sum to give

$$\frac{a+c}{a}\lambda^a_{eff} + \frac{b+c}{b}\lambda^b_{eff} = \lambda_a + \lambda_b + \left(\frac{c}{a} + \frac{c}{b}\right)\lambda_c. \tag{3.6}$$

A second measurement with new dimensions $\ell'_a$ and $\ell'_b$ provide a second expression having the same form as Eq. 3.6, and subtracting the two eliminates $\lambda_a$ and $\lambda_b$, leaving only $\lambda_c$ in terms of measured quantities. The values of $\lambda_a$ and $\lambda_b$ are then calculated from Eq. 3.4 and Eq. 3.5.

## 3.5 The Crystal Field Hamiltonian

Now we turn to a discussion of the way in which the magnetic penetration depth is obtained from our measurements of the ESR absorption spectrum. This amounts to the treatment of a dilute random array of $Gd^{3+}$ ions, each having an electron spin of $S = 7/2$, that contribute to the measured quantity $\frac{1}{2}\mu_0\lambda\chi''(\omega)$. The spectrum is a result of the energy level configuration determined by the splitting of the degenerate Gd spin levels by the crystalline field. Because the spin system is dilute, it can be described by a non-interacting single-spin effective crystal field (CF) Hamiltonian.

To produce a theoretical fit to the spectrum, it was necessary to diagonalize the CF Hamiltonian to calculate the energy levels. This was done numerically in Mathematica by Richard Harris in the early stages of this project. As part of her M.Sc. endeavor, Tami Pereg-Barnea continued this part of the project and extended and fine-tuned the software to produce the final fits to the data that are presented in this thesis. More complete details of her approach and a more general discussion of ESR spectroscopy are presented in her M.Sc. thesis [61].

In the case of our measurements, the application of a microwave field oriented perpendicular to the principal spin axis of the system is a time dependent perturbation that induces transitions between the spin levels. When the frequency of the applied field is tuned to the splitting between two levels, a maximum in the ESR absorption is observed. The intensity of the transition is found through the application of Fermi's golden rule for the two levels that define the transition, $m_i$ and $m_j$, and the susceptibility can be written as

$$\chi''_{ij}(\omega) = \mu_0\frac{\pi}{\hbar}|\mu_{ij}|^2\delta(\omega - [E_j - E_i]/\hbar)[N_i - N_j]. \tag{3.7}$$

In this expression, the eigenstates $m_i$ and $m_j$ correspond to the energies $E_i$ and $E_j$. The level occupation number is $N_i = N_0\mathcal{Z}^{-1}\exp(-\beta E_i)$, where $N_0$ is the total number of spins that participate in the process, $\mathcal{Z}$ is the partition function and $\beta = 1/k_BT$ is the inverse temperature. The perturbation $H_{rf}$ is given by the $S_x$ or $S_y$ operator and the matrix element between the two states is $\mu_{ij} = g\mu_B\langle m_j|S_{x/y}|m_i\rangle$, where $g$ is the Landé factor and $\mu_B$ is the Bohr magneton. It should be noted that approximately 30% of the stable isotopes of Gd have non-zero nuclear spin. However, the splitting due to these isotopes is much smaller than the ESR linewidth we observe and can therefore be ignored [80].

In real materials the ESR transitions are broadened by various relaxation processes such as spin-spin interactions, lattice disorder and spin-lattice interactions. This broadening, however, does not change the overall intensity of the ESR line, but merely replaces the delta function by some line shape function (in our case it is close to Lorentzian) whose integrated intensity is unity. In the initial stages of this work we examined optimally doped (y=0.93) crystals having three different concentrations of Gd ions; x$\simeq$ 0.5%, x$\simeq$ 1%, and x$\simeq$ 3%. From these measurements, we were able to conclude that the width of the Lorentzian-shaped ESR peaks ($\delta$f = 0.35 GHz for x= 1%) scaled approximately linearly with the nominal Gd concentration x, but with a substantial x=0 intercept of about 0.30 GHz. Although we did not perform

the detailed EPMA analysis to measure x of the nominally 0.5% and 3% samples, it seems clear that at x= 1% there is a dominant contribution to the broadening that is concentration independent. Since a dilute spin-spin interaction is expected to provide a relaxation rate that is linearly proportional to the concentration [81], our results suggest that some other process is responsible for much of the line broadening. The line width was also measured in the optimally doped samples at two different temperatures as shown in Fig. 3.4. The line widths decrease slightly upon increasing the temperature from 1 K to 3 K, indicating that spin-lattice relaxation is not likely to be the dominant process since typical relaxation mechanisms would be strongly temperature dependent. It remains unclear what the main spin relaxation mechanism responsible for the ESR line width is here. A final point is that no power dependence of the spectra were ever observed, verifying that saturation effects are unimportant and that the assumption of thermal equilibrium implicit in the Boltzmann factors used in Eq. 3.7 is well-founded.

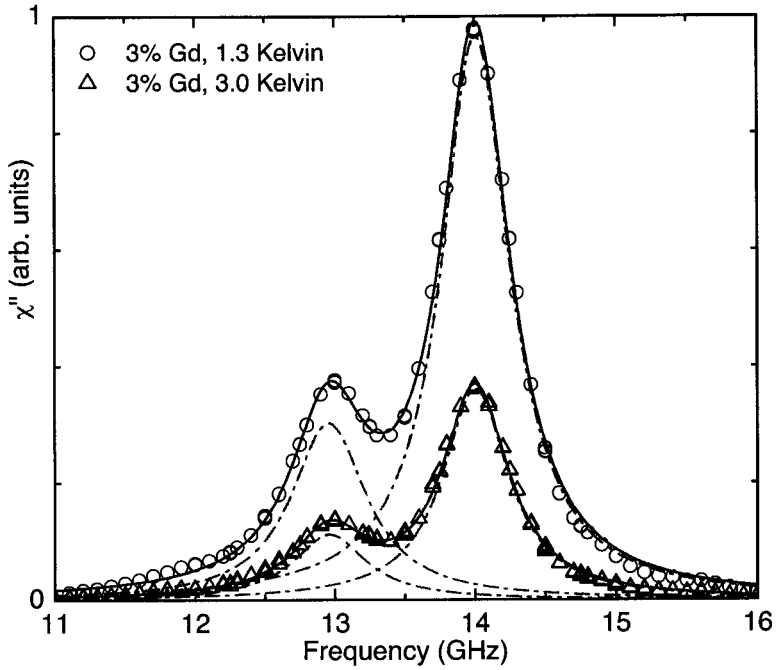


Figure 3.4: The temperature dependence of the ESR line width for 1.3 K and 3.0 K of an optimally doped $Gd_xY_{1-x}Ba_2Cu_3O_{6+y}$ sample with x=.03, normalized by the height of the 1.3 K peak. The G-band has line widths of 0.595 and 0.571 GHz and the F-band has line widths of 0.649 and 0.636 GHz at 1.3 K and 3 K, respectively. The line widths in our measurements of 1% Gd samples presented in this work are widths of 0.25-0.46 GHz at 1.3 K.

For the purpose of extracting $\lambda$, the quantity of interest is the effective number of spins exposed to the field $H_{rf}$. This requires a knowledge of the energy levels, their population and the corresponding matrix elements. This in turn requires knowing the Hamiltonian of the system. The Gd atom has the electron configuration of $[Xe]4f^75d^16s^2$ and ionization number of three in $Gd_xY_{1-x}Ba_2Cu_3O_{6+y}$. This implies

that the outer shell of the ion remains exactly half filled (seven $f$ electrons in fourteen states) and the system behaves like a 7/2 spin with no mixing with other $S+L$ multiplets due to Hund's rule. The construction of an effective Hamiltonian for a spin system is based on the expansion of the crystal field around the magnetic ion in terms of Stevens operators. These are the operator analogues of the spherical harmonics and are functions of $\hat{S}$, $\hat{S}_z$ and $\hat{S}_\pm$, given, for example, by Abragam and Bleaney [81]. Due to the lattice symmetries and the finite spin of the magnetic ion, the expansion reduces to a finite sum of operators $H = \sum_{p,q} B_q^p O_q^p$ where the $B_q^p$ are numerical coefficients called the crystal field parameters. The highest order of Stevens operator $O_q^p$ allowed for a spin of 7/2 in a crystal field is 6 since the matrix elements of the Stevens operators between two spin states are zero unless $p \leq 2S$. The order is restricted to even values by the required time reversal symmetry of the Hamiltonian. Furthermore, the $\hat{ab}$-plane anisotropy is so small that for most purposes one can assume $\pi/2$ rotation symmetry about the $\hat{c}$-axis; orthorhombicity is most significant in the overdoped samples. In the case of tetragonal symmetry, the relevant operators in order of significance are $O_2^0, O_4^0, O_4^4, O_6^0$ and $O_6^4$. The sixth order terms are difficult to resolve in our measured spectra and we simply adopt those of previous authors [82–84]. When the tetragonal ordering is slightly distorted, as will be discussed in the next section, three more Stevens operators can contribute to the Hamiltonian. For the present work, the largest and only significant one of them is $O_2^2$.

The spin 7/2 system discussed herein has four doubly degenerate energy levels with four eigenstates that are roughly the $\pm S_z$ eigenstates of the $S_z$ operator (see Fig. 3.5). The three allowed ESR transitions correspond to $S_z \rightarrow S_z \pm 1$. Small off-diagonal terms in the Hamiltonian, such as the $O_q^2$ and $O_q^4$, induce small level mixing that allow the otherwise forbidden transitions corresponding to $\pm 5/2 \rightarrow \pm 1/2$, $\pm 7/2 \rightarrow \pm 1/2$ and $\pm 7/2 \rightarrow \pm 3/2$ to occur, albeit with relatively low intensities. The resulting energy levels for different CF Hamiltonians are shown in Fig. 3.5. Due to the oxygen ordering in chains, which will be discussed in detail in the next section, most samples have more than one inequivalent site for the Gd ions. Therefore, two or three sets of CF parameters are needed to fit the spectrum. Following Jánossy *et al.* [82–84], and the spectra are labeled corresponding to a particular configuration by a band index using the notation shown in Fig. 3.6.

The fitting procedure is initiated by first constructing an effective spin Hamiltonian using the measured CF parameters reported by Jánossy *et al.* [82] and then adjusting the parameters to best fit the data. The fitting is focussed on the main transition ($\pm 7/2 \rightarrow \pm 5/2$ for each band) because it is the strongest and consequently least susceptible to experimental uncertainty. As a final step, a multiplicative factor representing the effective number of spins that have participated in the ESR process is then used to scale the overall amplitude of the model spectrum to match the measured data. This number, combined with the measured Gd concentration x in the crystal, gives the effective penetration depth $\lambda_{eff}$.

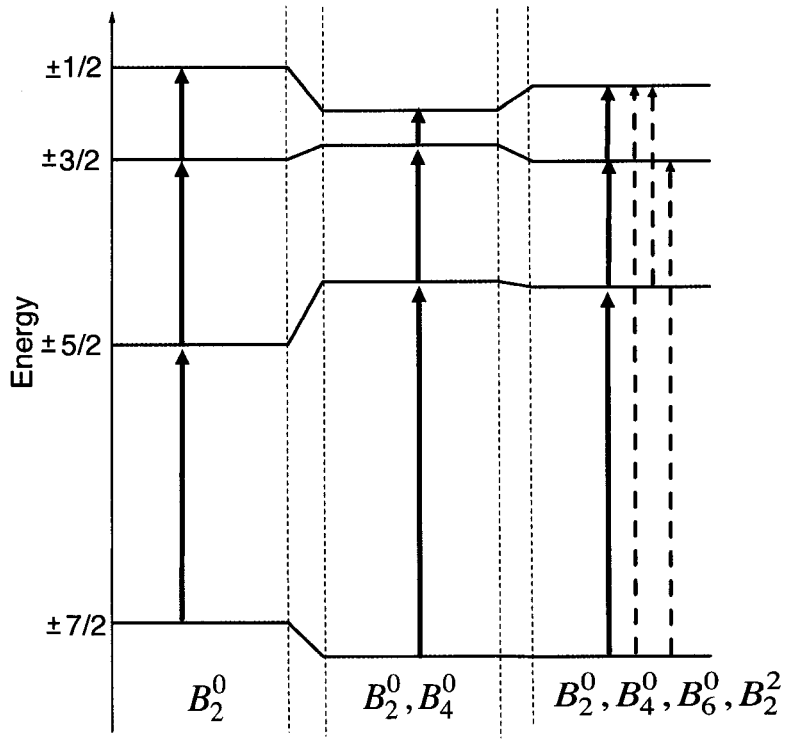


Figure 3.5: The energy levels resulting from the effective crystal field Hamiltonian. The levels, from left to right, correspond to: a diagonal Hamiltonian, $H \propto O_2^0 = 3S_z^2 - S(S+1)$, a tetragonal Hamiltonian with some off-diagonal level mixing and finally an orthorhombic Hamiltonian with $O_2^2 = (S_+^2 + S_-^2)/2$. The CF parameters shown here are typical for the samples we have measured, except for $B_2^2$ which has been exaggerated in order to make its effect more visible.

## 3.6 Dependence of ESR spectra on oxygen configuration

The presence of a chain layer breaks the tetragonal symmetry and the Stevens operator expansion of the foregoing section is then no longer exact. However, the chains are far from the Gd sites and this effect can be treated as a perturbation, leading to line broadening or line splitting. Here we will consider line splitting associated with distinct Gd environments and simply handle the line width as a parameter in a Lorentzian fit. Different types of Gd sites are encountered because hole doping in this system is controlled by manipulating the oxygen content and ordering of the $CuO_y$ chains in $Gd_xY_{1-x}Ba_2Cu_3O_{6+y}$. The oxygen content is set by annealing in controlled oxygen partial pressure at high temperatures and then the oxygen ions tend to organize into lengths of CuO chain fragments which are able to promote holes to the $CuO_2$ planes [31]. The strong tendency to form chain fragments means that there are 7 probable Gd environments corresponding to anything from 0 to 4 nearest neighbor chains. These different crystallographic environments have been identified previously

in ESR experiments on magnetically aligned $Gd_xY_{1-x}Ba_2Cu_3O_{6+y}$ powders [82–84] and are illustrated in Fig. 3.6.

The chains also tend to form ordered periodic superlattices consisting of arrangements of full and empty $CuO_y$ chains. The structures can be particularly well-ordered for special values of y. In the case of full oxygen doping, the CuO chains are nearly completely full with every Gd ion having four nearest neighbor chains. This results in the simplest of the spectra observed from among the five doping levels that we studied. It involves one primary set of CF parameters, denoted the G-band by Jánossey *et al.*, and generates three dominant ESR transitions. A secondary contribution of much lower intensity is also present in these measurements, resulting from a configuration where one of the four chain oxygens is missing, denoted the F-band. In the overdoped sample, the largest transition ($7/2 \rightarrow 5/2$) of this latter band is barely discernable, but as the oxygen concentration is reduced to optimal doping, the intensity of the F-band builds, as demonstrated in Fig. 3.6.

At lower doping, the next best-ordered phase occurs near $y \approx 0.5$, where the chains form an ortho-II structure of alternating full and empty chains [35]. Other ordered phases are: ortho-III with FFE (full, full, empty) chains and ortho-VIII with FFEFFEFE chains. In each of these phases there is more than one possible chain configuration around the Gd ions. Having detailed spectra at each doping allows us to identify the different bands and fit each spectrum with a set of crystal field parameters for each band. The fitted $\chi''$ spectra are shown in Fig. 3.6. In each spectrum, the relative intensities of the different bands is a measure of the relative number of Gd ions in each configuration. This information can be used to determine the amount of oxygen in the sample according to:

$$y = \frac{1}{4}\sum_n nI_n \qquad \sum_n I_n = 1 \tag{3.8}$$

where $n$ is the number of full nearest neighbor CuO chains in the band and $I_n$ is the observed relative intensity of the line associated with a particular band. The oxygen content is given by $6 + y$. The ESR measured oxygen content compared to that measured chemically is presented in Fig. 3.7. Note that the ESR points consistently underestimate the amount of oxygen in the crystals. We attribute this to the inefficiency of isolated oxygens in empty chains in promoting a hole into the $CuO_2$ planes. The above oxygen content analysis assumes maximal length of chains, *i.e.* all chains are either full or missing with no isolated oxygens or vacancies. Since the Gd ions are likely to be sensing the presence of chains through their influence on the charge distribution on the much nearer $CuO_2$ planes, an isolated oxygen ion hardly affects the crystal field environment since it does not promote a hole into the planes [31]. Thus a Gd ion near an isolated oxygen in an otherwise empty chain will experience the crystal field of an empty chain. This will lead to an underestimate of the oxygen content, but *will not affect the overall counting of Gd ions.*

It is also interesting to note that the ESR analysis provides a good measure of the chain disorder. For example, perfect three dimensional ortho-II ordering should produce only one band, corresponding to two full chains, the D-band. However, our

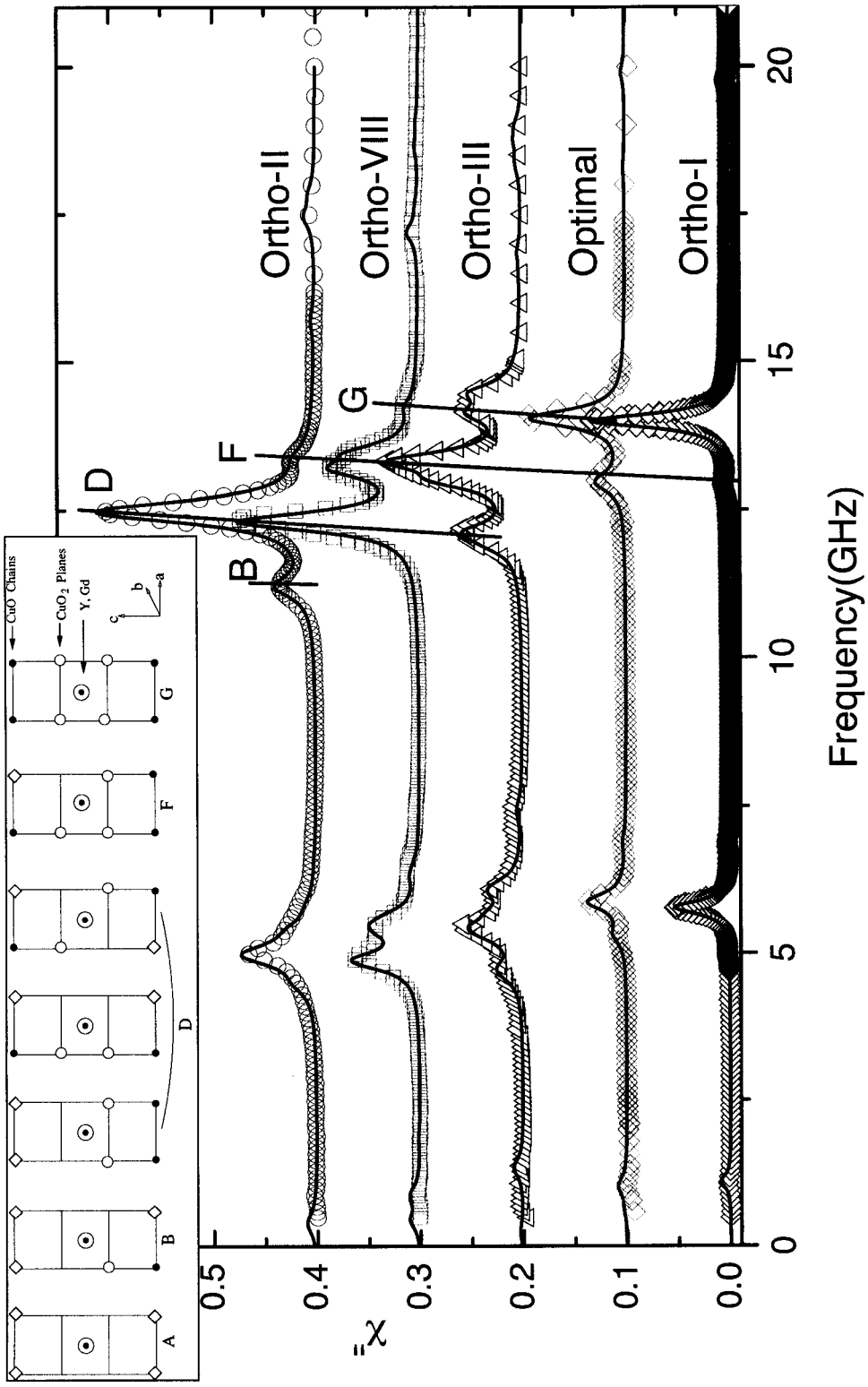


Figure 3.6: Measured ESR spectra for five dopings with screening currents running along the $\hat{a}$ direction shown with the spectrum calculated using the CF Hamiltonian. The calculated curve is scaled by an overall multiplicative factor of $\lambda_{eff}$ as explained in the text. The various spectra were offset by 0.1 from each other and the ortho-I spectrum was scaled down by a factor of four. The inset shows the identification of the ESR bands (A,B,D,F,G) attributed to a variety of oxygen configurations, taken from S. Pekker *et al.* [83]. Figures represent cross-sections through the center of a $YBa_2Cu_3O_{6+y}$ unit cell parallel to the $\hat{a}\hat{c}$-plane. Open circles indicate holes promoted onto Cu atoms in the $CuO_2$ planes, black circles indicate oxygen atoms in the CuO chains and diamonds indicate oxygen vacancies in the CuO chains. The central circle is the Gd ion. Note that the three D-band configurations all result in a single ESR band.

ortho-II spectrum displays two additional bands (the B and F bands) resulting from imperfections in the ortho-II ordering [35]. These deviations can be interpreted as ortho-II phase boundaries. Our ortho-III and ortho-VIII spectra are consistent with the existence of long range order along the $\hat{ab}$ plane, but with random stacking along the $\hat{c}$-direction.

## 3.7 Results

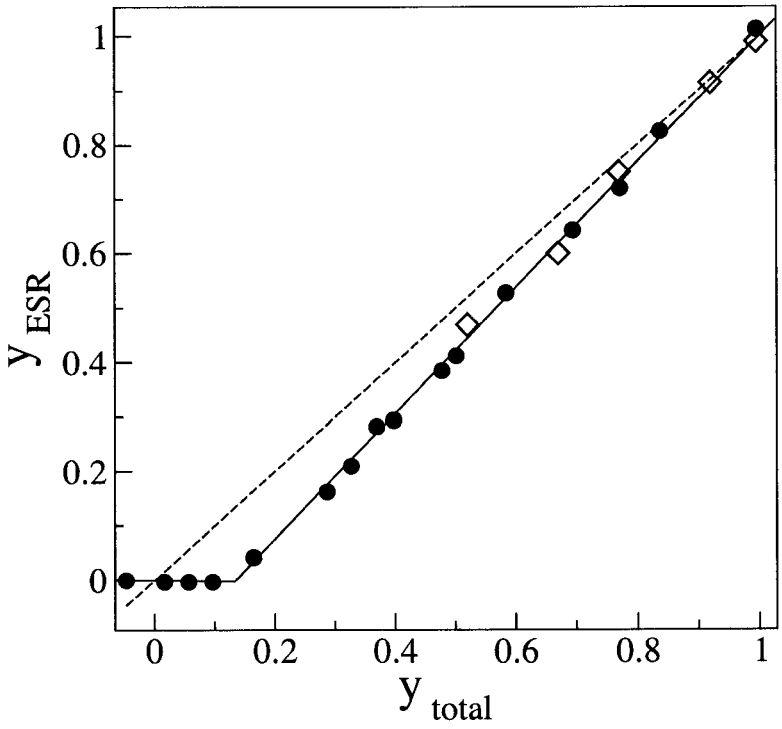


Figure 3.7: Ordered oxygen content as measured by ESR versus the total oxygen content of the sample. The solid circles are taken from Pekker *et al.* [83] ($y_{total}$ determined by weighing the sample) and the open diamonds are the values obtained from the present work ($y_{total}$ determined by the annealing temperature and oxygen partial pressure).

Detailed measurements of the ZF ESR absorption spectrum were performed in high quality samples of $Gd_{0.01}Y_{0.99}Ba_2Cu_3O_{6+y}$ at five different values of y. As noted above, four of these were chosen to be in ranges with particularly well-ordered CuO chain structures, denoted by the periodicity of their chain superlattices (ortho-I,II,III,VIII). The optimally doped sample, so-named because of the maximal $T_c$ value of 93 K (y=0.93) is in the ortho-I phase, but has a substantial number of oxygen vacancies on the chains. The ESR spectrum at each doping was fitted with a spectrum generated by an effective CF Hamiltonian, with initial guesses for the CF parameters taken from Rockenbauer *et al.* [84]. Subsequently, the CF parameters were adjusted

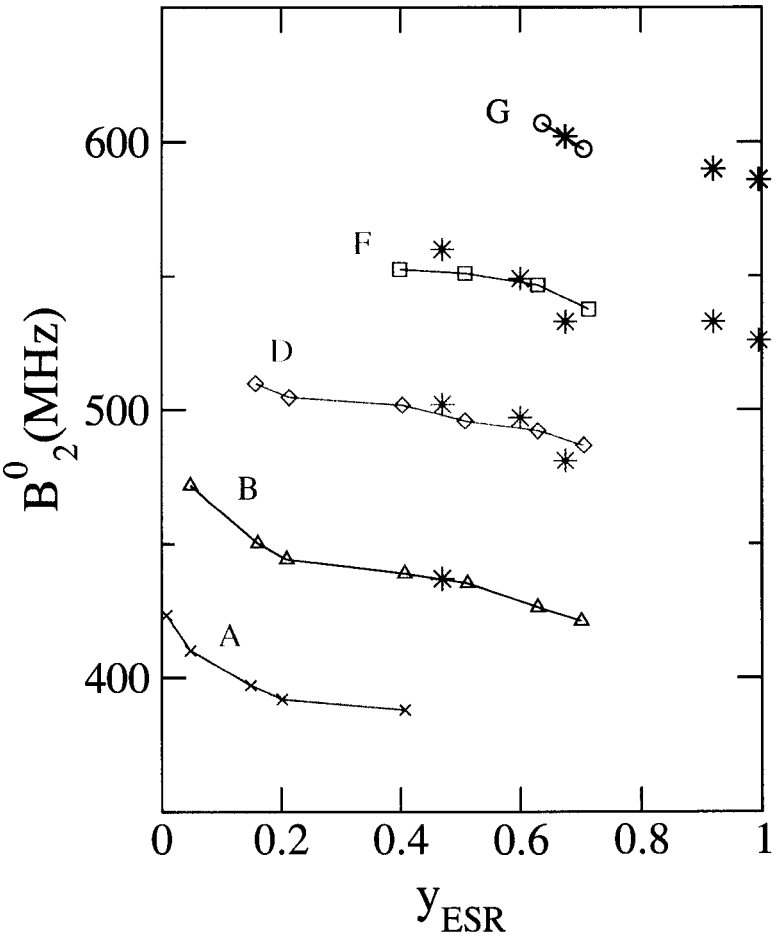


Figure 3.8: The oxygen doping evolution of the main CF parameter $B_2^0$ in MHz for the different bands. The open symbols are taken from Rockenbauer *et al.* [84] and the stars are the ZF ESR best fit values. For the ortho-III sample, where more than one set of CF parameters was found for each line, we show the values closest to previously the measured ones.

to best describe our measured spectra, and the best fit values are presented in Table 3.7. The evolution of the dominant CF parameter ($B_2^0$) as a function of the ESR measured oxygen content is shown in Fig. 3.8. The values and systematic trends of our fit values compare well to those of previous conventional ESR studies on powders [82–84].

The ESR spectrum is a sensitive probe of the crystallographic structure and the crystal symmetry in particular. This high sensitivity is demonstrated at its best in the spectrum of our overdoped sample. This is the most ordered and most orthorhombic phase, with four full CuO chains around virtually every Gd ion. The lines are very sharp and the main band, G, corresponds to 96% of the total spectral weight. As seen in Fig. 3.10, the orthorhombicity of the crystal is manifested as an additional line in the spectrum that appears only when the measurement is performed with screening currents flowing along the $\hat{b}$-direction. The spectra for both directions can

| Sample (Gd%) | Band | Intensity | $B_2^0$ (MHz) | $B_2^2$ (MHz) | $B_4^0$ (MHz) | $B_4^4$ (MHz) | $7/2 \rightarrow 5/2$ (GHz) | $3/2 \rightarrow 5/2$ (GHz) | $1/2 \rightarrow 3/2$ (GHz) |
|---|---|---|---|---|---|---|---|---|---|
| ortho-I | G | 96% | -587 (-598) | 26.7 (-) | -3.1 (-3.1) | 12.5 (13.2) | 14.0 | 5.8 | 1.12 |
| $(1.08 \pm 0.06)$ | F | 4% | -526 (-541) | 26.7 (-) | -3.1 (-3.1) | 12.5 (17.2) | 12.9 | 5.0 | 0.9 |
| optimal | G | 75% | -590(-598) | 0 | -3.1 (-3.1) | 12.7 (13.2) | 14.04 | 5.86 | 1.05 |
| $(1.28 \pm 0.02)$ | F | 25% | -533(-541) | 0 | -3.1 (-3.1) | 12.5 (17.2) | 13.02 | 5.2 | |
| ortho-III | G | 21% | -617,-604 -585(-598) | 30 (-) | -3.0 (-3.1) | 12.5 (13.1) | 14.4,14.1 | 6.13,6.03 | 1.4,1.3 |
| $(1.02 \pm 0.05)$ | F | 56% | -533,-517 (-541) | 6.7 (-) | -3.5 (-3.1) | 17.1 (17.2) | 13.3,13.0 | 5.4,5.45 | 0.2,0.3 |
| | D | 23% | -481,-475 (-497) | 26.7 (-) | -3.1 (-3.1) | 14.6 (14.7) | 12.1,11.9 | 4.7,4.6 | 0.6 |
| ortho-VIII | G | 2% | -630 (-598) | 1.6 (-) | -2.5 (-3.1) | 9 (13.1) | 14.2 | 6.3 | 1.9 |
| $(1.38 \pm 0.1)$ | F | 36% | -549 (-541) | 1.6 (-) | -3.0 (-3.1) | 12.5 (17.2) | 13.2 | 5.5 | 0.8 |
| | D | 62% | -497 (-497) | 1.6 (-) | -3.1 (-3.1) | 12.5 (14.7) | 12.3 | 4.9 | 0.8 |
| ortho-II | F | 4% | -560 (-541) | 5 (-) | -3.1 (-3.1) | 17.2 (17.2) | 13.4 | 5.8 | 0.8 |
| $(1.08 \pm 0.06)$ | D | 81% | -502 (-497) | 5 (-) | -3.2 (-3.1) | 14.7 (14.7) | 12.5 | 5.0 | 0.4 |
| | B | 15% | -437 (-445) | 5 (-) | -3.2 (-3.1) | 15.5 (17.2) | 11.2 | 4.5 | 0.2 |

Table 3.1: Crystal field parameters for the ESR bands that result from different oxygen contents of $Gd_{.01}Y_{.99}Ba_2Cu_3O_{6+y}$ in MHz. The Gd% in brackets in the first column indicates the relative substitution of Gd for Y. The CF parameters measured by Rockenbauer *et al.* [84] in conventional ESR on powder samples are given in brackets, and at each doping we have taken values from the nearest doping measured by these authors. The values of $B_6^0$ and $B_6^4$ could not be resolved from our spectra and we simply adopt the values of Rockenbauer *et al.* The transition frequencies, shown in GHz, were found either directly from the observed lines or by the fit Hamiltonian (when the lines were unobservable). The ortho-III spectrum required more than one set of CF parameters for each band due to further line splitting of unknown origin, which may be related to oxygen inhomogeneity.

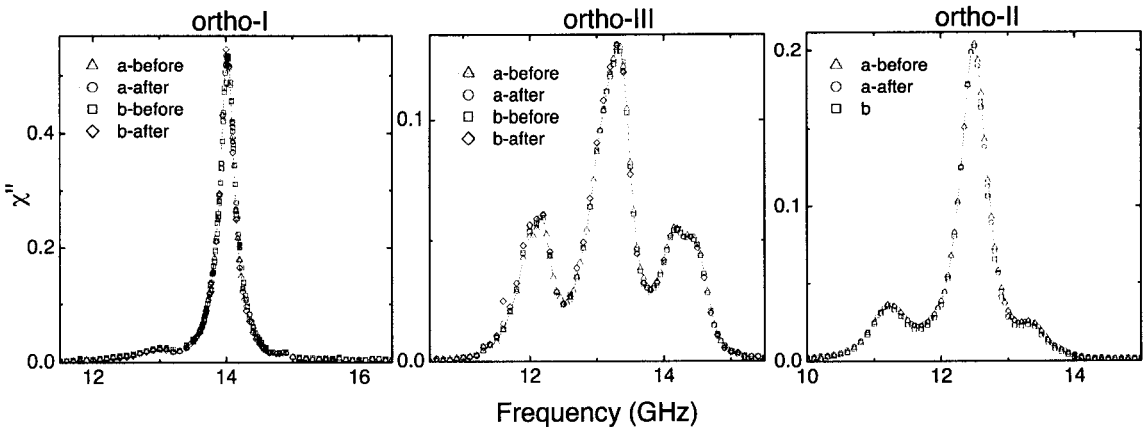


Figure 3.9: The main ESR line $\pm 5/2 \rightarrow 7/2$ in ortho-I, ortho-III and ortho-II. In each figure we overlay three or four measurements of the same crystal in the $\hat{a}$ and $\hat{b}$-directions, before and after cleaving the sample. Each graph has been scaled by the effective penetration depth $\lambda_{eff}$ of the particular measurement so that only $\chi''$ is presented. The changes in $\lambda_{eff}$ are due to the different aspect ratios of the crystal before and after the cleave and the different orientations of measurements. The fact that the curves lay directly on top of one another indicates the very high reproducibility of the measurements.

be fit with a single set of CF parameters by introducing an orthorhombic term in the CF Hamiltonian. This term is $B_2^2 O_2^2$, where $B_2^2$ is the measured coefficient and $O_2^2 = (S_+^2 + S_-^2)/2 = (S_x^2 - S_y^2)/2$. The inclusion of this term allows the otherwise forbidden transition of $\pm 5/2 \rightarrow \pm 1/2$ only when the magnetic field is applied in the $\hat{a}$-direction, and reveals the slight orthorhombicity of the crystal (the difference between the $\hat{a}$ and $\hat{b}$-dimensions of the unit cell is less than 2%).

The measured ortho-III spectrum is indicative of some disorder in the chain structure. First, the substantial amount of spectral weight in the F-band, which corresponds to three full chains, indicates that even if the ordering is perfect in the planes, the stacking along the $\hat{c}$-direction is disordered, *i.e.* the ortho-III structure may shift between adjacent chain layers [32, 78]. Second, it is found that each ESR peak is composed of two closely spaced lines that together produce a non-Lorentzian shape. Since the measured ESR oxygen level is consistent with the other crystals (see $y_{total} = 0.77$ in Fig. 3.7), confidence in the band identification is gained and the minor splitting is not interpreted as a change of chain configuration. The splitting implies a small variation of CF parameters *within the same band.* This might be the result of inhomogeneity in the oxygen concentration, which is consistent with a measured transition temperature broadening $\Delta T_c \approx 1$ K. However, we take the fact that the line shapes were not affected by cleaving the sample into smaller pieces as evidence that the sample is not macroscopically phase separated.

Our ortho-II spectra suggest fairly good ordering within the chain layers with a somewhat shorter correlation length in the $\hat{c}$-direction, in agreement with X-ray anal-

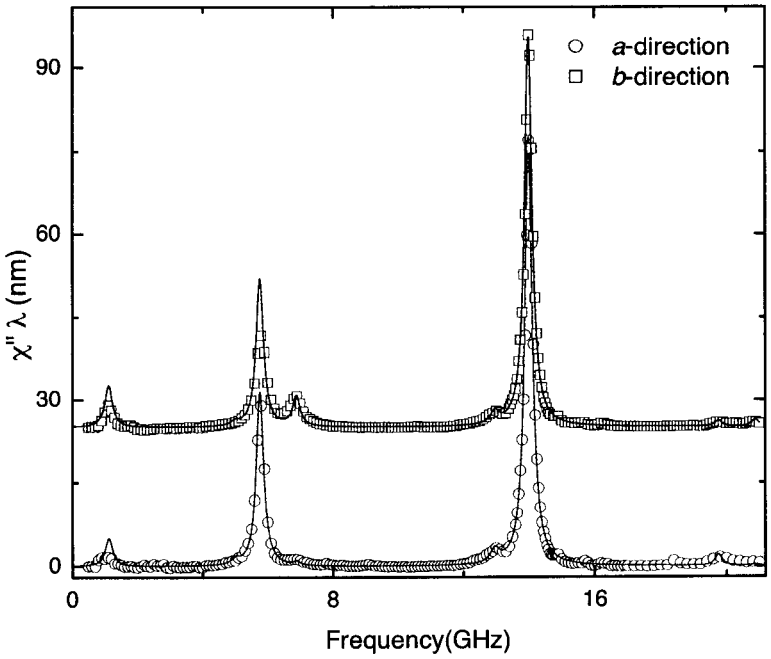


Figure 3.10: Oxygen-overdoped $Gd_{.01}Y_{.99}Ba_2Cu_3O_{6.993}$ sample ESR absorption spectra in the $\hat{a}$ and $\hat{b}$-directions. The $\hat{b}$-axis data was offset by 25 nm for clarity. The orthorhombicity of the crystal lattice is apparent in the appearance of an additional ESR line at 6.9 GHz when the screening currents flow in the $\hat{b}$-direction. This line corresponds to the $\pm 1/2 \rightarrow \pm 5/2$ transition that is allowed along the $\hat{b}$-direction, generated by the orthorhombic Stevens operator $B_2^2 = (S_x^2 - S_y^2)/2$. This same line appears with suppressed intensity in the $\hat{a}$-direction due to a small fraction of twinning in the sample. The observed spectrum indicates a predominance of the G-band oxygen configuration, as expected for a fully doped sample, with a 4% contribution from the F-band. For comparison, note that the F-band contribution in the optimally doped sample shown in Fig. 3.6 is much larger as a result of the lower oxygen content.

ysis [35]. The extraction of $\lambda_c$ in this sample was done by comparing two measurements in the $\hat{a}$-direction, where the first measurement was done on the whole sample and the second one on two pieces resulting from a cleave along the $\hat{b}$-direction. The effective penetration depth $\lambda_{eff}$ was observed to increase by about 210 nm due to the introduction of two more sample $\widehat{bc}$-faces, where currents flow along the $\hat{c}$-direction.

Enough data was obtained in order to reliably extract the absolute values of the penetration depth in all three crystallographic directions for three of the five doping levels studied: fully doped, ortho-II and ortho-III. The measurements at the remaining two doping levels were made using samples that were not amenable to the cleaving procedure required to extract absolute values of $\lambda$. The final results for $\lambda$ were derived as described in the previous sections, with the emphasis on performing enough measurements on the same sample in order to eliminate sample-dependent

| Phase | $T_c$(K) | 6+y | $\lambda_a$(nm) | $\lambda_b$(nm) | $\lambda_a/\lambda_b$ | $\lambda_c$(nm) |
|---|---|---|---|---|---|---|
| Ortho-I | 89 | 6.995 | $103 \pm 8$ | $80 \pm 5$ | $1.29 \pm 0.07$ | $635 \pm 50$ |
| Ortho-III | 75 | 6.77 | $135 \pm 13$ | $116 \pm 12$ | $1.16 \pm 0.12$ | $2068 \pm 200$ |
| Ortho-II | 56 | 6.52 | $202 \pm 22$ | $140 \pm 28$ | $1.44 \pm 0.26$ | $7500 \pm 480$ |

Table 3.2: Experimental values of the anisotropic magnetic penetration depth extracted from four or more different measurements of $\lambda_{eff}$ on the same crystal, with the microwave field applied in different directions and for different sample aspect ratios achieved by cleaving. The uncertainty in the ansisotropy is reduced since some of the systematic contributions to the uncertainty in absolute value cancel when comparing measurements on the same sample.

effects and to overdetermine the values of $\lambda$ for error control. The penetration depth results are presented in Table 3.2. The error estimates account for uncertainties arising from measurements of the sample dimensions, calibration of the microwave absorption experiment [85] and the estimation of the ESR fit parameters. Since the extraction of the penetration depth in the three crystallographic directions depends sensitively on the sample's dimensions, it is important to work with crystals that have smooth parallel well defined faces whose area is easy to measure. This was most easily achieved by choosing a single sample having a nice platelet geometry for each doping. If the analysis were restricted to measurements made on the same crystal where the geometry of the sample was altered in a controlled fashion by cleaving, a high degree of internal consistency between different measurements is obtained. In all cases we performed an extra measurement that overdetermines the penetration depth values and found agreement ranging from 0.5% to 6%. In the case of the ortho-II doping a second sample was measured having a 30% higher Gd concentration, and the results agreed to within 12% of the first sample. The high reproducibility of the measurements is demonstrated in Fig. 3.9 where we present data for the same crystal before and after cleaving the sample. Despite changing the aspect ratio of the crystal by approximately 50% in each case, the spectra are identical, modulo the overall multiplicative factor of $\lambda_{eff}$.

## 3.8 Discussion

The highly-detailed broadband measurements of the zero field ESR absorption spectrum in $Gd_xY_{1-x}Ba_2Cu_3O_{6+y}$ samples have provided a sensitive means of determining the crystal field parameters at the yttrium site, as well as providing insight into the way in which oxygen orders into CuO chains. The measured crystal field parameters were shown to be in excellent agreement with those previously obtained using high field ESR on powdered samples [82–84]. These new results also support the conclusions of the high field ESR work that isolated oxygen atoms in vacant CuO chains do not significantly influence the CF configuration around the magnetic ion and therefore cannot be distinguished from vacant chains, at least not via ESR spectroscopy.

| $T_c$(K) | $\lambda_a$(nm) | $\lambda_b$(nm) | $\lambda_c$(nm) | $\lambda_{ab}(nm)$ | Technique | Group | Year | Material |
|---|---|---|---|---|---|---|---|---|
| 89 | $103 \pm 8$ | $80 \pm 5$ | $635 \pm 50$ | $91^* \pm 6$ | Microwave | UBC [63] | 2003 | Single Crystal |
| 75 | $135 \pm 13$ | $116 \pm 12$ | $2068 \pm 200$ | $125^* \pm 12$ | Microwave | UBC [63] | 2003 | Single Crystal |
| 56 | $202 \pm 22$ | $140 \pm 28$ | $7500 \pm 480$ | $168^* \pm 26$ | Microwave | UBC [63] | 2003 | Single Crystal |
| 93 | — | — | — | $112^*$ | $\mu$SR | Sonier *et al.* [64] | 2000 | Mosaic |
| 59 | — | — | — | $170^*$ | $\mu$SR | Sonier *et al.* [86] | 1997 | Mosaic |
| 92 | 160 | 100 | — | $127^*$ | IR Reflectance | Basov *et al.* [73] | 1995 | Single Crystal |
| 59 | 248 | 183 | — | $213^*$ | IR Reflectance | Homes *et al.* [87] | 1999 | Single Crystal |
| 53 | — | — | 7800 | — | IR Reflectance | Homes *et al.* [72] | 1995 | Single Crystal |
| 58 | — | — | 6520 | — | IR Reflectance | Homes *et al.* [72] | 1995 | Single Crystal |
| 63 | — | — | 5170 | — | IR Reflectance | Homes *et al.* [72] | 1995 | Single Crystal |
| 78 | — | — | 3370 | — | IR Reflectance | Homes *et al.* [72] | 1995 | Single Crystal |
| 89 | — | — | 2030 | — | IR Reflectance | Homes *et al.* [72] | 1995 | Single Crystal |
| 91.5 | — | — | 1580 | — | IR Reflectance | Homes *et al.* [72] | 1995 | Single Crystal |
| 93.2 | — | — | 1060 | — | IR Reflectance | Homes *et al.* [72] | 1995 | Single Crystal |
| 92 | — | — | 1260 | $140^\dagger \pm 25\%$ | AC-Susceptibility | Panagopoulos *et al.* [69] | 1998 | Aligned Powder |
| 66 | — | — | 4530 | $210^\dagger \pm 25\%$ | AC-Susceptibility | Panagopoulos *et al.* [69] | 1998 | Aligned Powder |
| 56 | — | — | 7170 | $280^\dagger \pm 25\%$ | AC-Susceptibility | Panagopoulos *et al.* [69] | 1998 | Aligned Powder |
| ~90 | 155 | 80 | — | $111^*$ | $\mu$SR | Tallon *et al.* [88] | 1995 | Polycrystalline |
| 89 | — | — | — | $119^*$ | $\mu$SR | Pümpin *et al.* [89] | 1990 | Polycrystalline |
| 89 | — | — | — | $176^*$ | $\mu$SR | Uemura *et al.* [90] | 1989 | Polycrystalline |
| 70 | — | — | — | $204^*$ | $\mu$SR | Uemura *et al.* [90] | 1989 | Polycrystalline |
| 61 | — | — | — | $217^*$ | $\mu$SR | Uemura *et al.* [90] | 1989 | Polycrystalline |
| 90 | — | — | — | $200^\dagger$ | Mut. Inductance | Boyce *et al.* [91] | 2000 | Thin Film |
| 80 | — | — | — | $239^\dagger$ | Mut. Inductance | Boyce *et al.* [91] | 2000 | Thin Film |
| 60 | — | — | — | $275^\dagger$ | Mut. Inductance | Boyce *et al.* [91] | 2000 | Thin Film |
| 93 | — | — | — | $146^\dagger \pm 15$ | Mut. Inductance | Prozorov *et al.* [75] | 2000 | Thin Film |
| 93 | — | — | — | $157^\dagger \pm 20$ | Transmission | de Vaulchier *et al.* [92] | 1996 | Thin Film |

Table 3.3: Measurements of $\lambda(T \to 0)$ for $YBa_2Cu_3O_{6+y}$. The microwave and infrared techniques are capable of resolving $\lambda_a$ and $\lambda_b$, however $\mu SR$ determines the geometric mean $\lambda_{ab} = \sqrt{\lambda_a \lambda_b}$ (denoted by $^*$) and the field exclusion methods determine the average $\lambda_{ab} = (\lambda_a + \lambda_b)/2$ (denoted by $^\dagger$). The in-plane values of Tallon *et al.* are inferred from the doping dependence of their $\lambda_{ab}$ measurements. Uncertainties are provided when given in the original reference.

This is in accord with the fact that isolated oxygens do not promote holes from the copper-oxygen planes [31].

The principal result of the present measurements is a set of accurate values for the penetration depth in all three crystallographic directions for three oxygen-ordered phases of $YBa_2Cu_3O_{6+y}$, summarized in Table 3.2. The data reveal that the $\hat{c}$-axis penetration depth is large and increases very rapidly with decreasing doping, as observed previously in infrared measurements of $\lambda_c$ by Homes *et al.* [72]. These latter results are included in Table 3.3 which contains a survey of many of the relevant measurements of $\lambda(T \rightarrow 0)$ from the literature, as well as the present microwave ESR results. The new absolute values of penetration depth obtained with single crystals are considerably smaller than those obtained from magnetization studies of aligned powders by Panagopoulos *et al.* [69]. The origin of this discrepancy is not clear, but might be due to assumptions made in the analysis of the powder data or problems with the surfaces of grains embedded in epoxy. Our absolute values of $\lambda_a$ and $\lambda_b$ are also somewhat smaller than those obtained by far infrared measurements near optimal doping by Basov *et al.* [73]. However, the infrared measurements did point out the importance of the in-plane penetration depth anisotropy in these materials which becomes very large in the $YBa_2Cu_3O_{6.99}$ sample studied here. This anisotropy has been attributed to the presence of a nearly one-dimensional Fermi sheet derived mainly from the bands associated with the CuO chains [93].

As an overall trend, our values of $\lambda$ are considerably smaller than those inferred from $\mu SR$ measurements. An exception to this is the in-plane work of Sonier *et al.* who measured mosaics of high-purity, detwinned single crystals at two oxygen dopings nearly coincident with those of the microwave ESR work [64, 86]. Although the muon measurements are unable to directly determine the anisotropy in $\lambda$, their values compare well with the geometric mean of the $\hat{ab}$-plane values reported here. They found that a sample of $YBa_2Cu_3O_{6.60}$ with $T_c$=59 K had $\lambda_{ab}$=170 nm [86], very close to the geometric mean $\sqrt{\lambda_a\lambda_b}$=168±26 nm of the $T_c$=56 K sample studied here. Their optimally doped sample of $YBa_2Cu_3O_{6.95}$ with $T_c$=93 K had $\lambda_{ab}$=112 nm [64], which lies between the means of the $T_c$=75 K sample (125±12 nm) and the overdoped $T_c$=89 K sample (91±6 nm) studied here. The agreement reflects the particular care taken in these $\mu SR$ measurements to cover a wide range of applied magnetic fields in order to ascertain the low field limiting values and thus minimize the non-linear, non-local, and other effects that can arise in the vortex state.

As mentioned previously, $\mu SR$ measurements cannot directly measure the in-plane anisotropy. Despite this, Tallon *et al.* have also inferred a contribution from a CuO chain superfluid component by noting the very large increase in muon depolarization rate as the chain oxygen sites become filled near $YBa_2Cu_3O_7$ [88]. The interpretation of their polycrystalline $\mu SR$ data suggested values of $\lambda_a$=155 nm and $\lambda_b$=80 nm for samples with fully doped CuO chains, which overestimates both the overall magnitude and the anisotropy of the in-plane penetration depth relative to ours. However, the basic picture of chain-driven anisotropy is supported by our new microwave measurements. The new measurements also show substantial anisotropy in the ortho-II ordered sample, but rather less in the ortho-III sample, a sensible trend since the

ortho-III ordering is much poorer, which results in more fragmented chains.

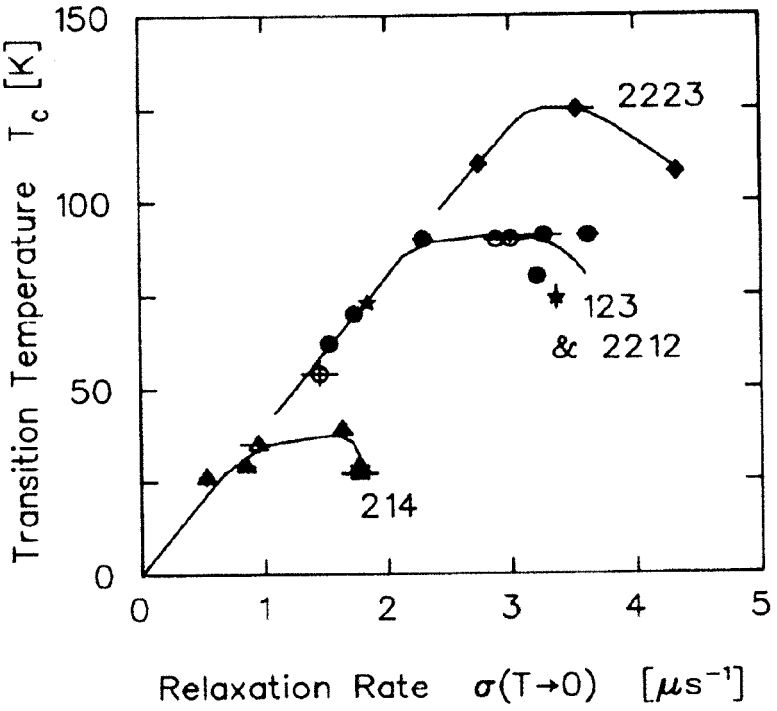


Figure 3.11: Muon spin relaxation data of Uemura *et al.* on polycrystalline samples of 16 different specimens of cuprate superconductor, plotted as $T_c$ versus muon spin relaxation rate $\sigma(T \rightarrow 0)$. This plot has become a widely-known piece of phenomenology in the study of the cuprates, often referred to as the "Uemura Plot" which includes the scaling $T_c \propto n_s/m^*$ at low doping. Details of the compounds studied in the plot are given in the text. Figure taken from Uemura *et al.* [90].

Much of the work on the doping dependence of $\lambda_{ab}$ has relied on muon spin relaxation measurements on polycrystalline samples. A long-accepted empirical result has been the linear relationship between $T_c$ and the superfluid phase stiffness $\rho_s \propto 1/\lambda^2 \propto n_s/m^*$, first inferred by Uemura *et al.* in the form of Fig. 3.11 [90]. Here, they report on 16 different specimens from 8 different cuprate compounds representing those with single (2:1:4), double (1:2:3, 2:2:1:2) and triple (2:2:2:3) $CuO_2$ layers in the unit cell.[1] It is concluded that the universal linear relation at underdoping between $T_c$ and $\sigma$ holds in all three classes of material, independent of the details of the crystal structure. Furthermore, $T_c$ saturates beyond a critical value of $\sigma$ in all systems.

Extracting a value for $1/\lambda^2$ from the value of $\sigma$ from $\mu SR$ measurements hinges on the success of a detailed model of the vortex lattice that provides a fit to the field

[1] In Fig.3.11, the 2:1:4 prototype is represented by $La_{2-x}Sr_xCuO_4$ (closed triangles); 1:2:3 by $YBa_2Cu_3O_{6+y}$ and $Y_{0.7}Ca_{0.3}Ba_2Cu_3O_7$ (closed circles); 2:2:1:2 by $Bi_2Sr_2CaCu_2O_8$ and $Tl_{0.5}Pb_{0.5}Sr_2CaCu_2O_7$ (stars); and 2:2:2:3 by $Bi_{2-x}Pb_xSr_2Ca_2Cu_3O_{10}$ and $Tl_2Ba_2Ca_2Cu_3O_{10}$ and $Tl_{0.5}Pb_{0.5}Sr_2Ca_2Cu_3O_9$ (closed diamonds).

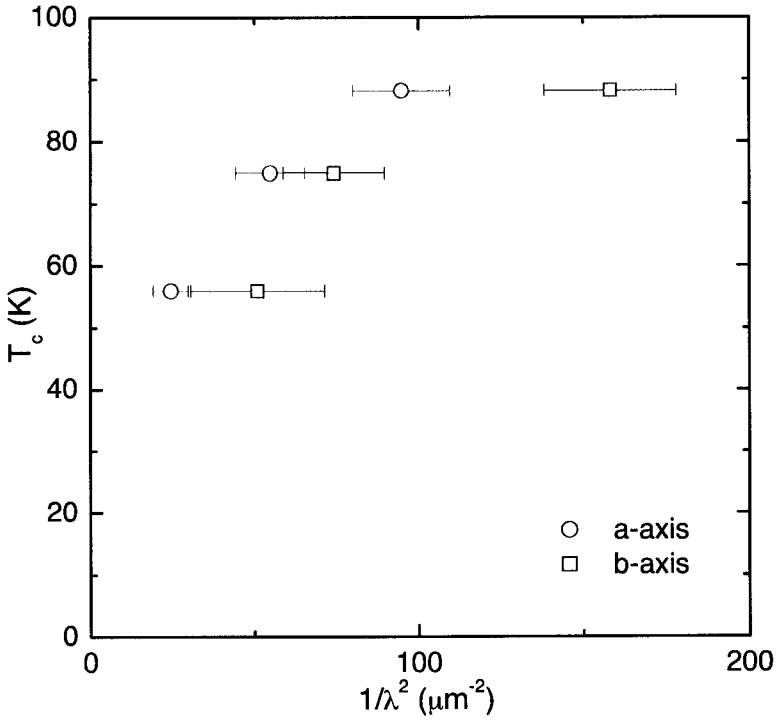


Figure 3.12: Measurements of the in-plane anisotropic absolute penetration depth $\lambda$ in $YBa_2Cu_3O_{6+y}$ for y=0.52, y=0.77 and y=0.995 plotted as $T_c$ versus superfluid phase stiffness ($\propto 1/\lambda^2$). Our data does not obey the scaling $T_c \propto 1/\lambda_a^2$ despite covering the same doping range as that of Fig. 3.11.

distribution detected by the muons. In most cases, the $\mu$SR data is analyzed assuming a simple Gaussian fit to the dephasing of the muon spins in order to extract $\sigma$, the relaxation rate, which is deemed proportional to $1/\lambda^2$. All $\mu$SR data in Table 3.3, except that of Sonier *et al.*, are analyzed in this fashion. The conversion from the measured $\sigma$ values to $1/\lambda^2$ is done using the formula $\sigma = 7.09 \times 10^4 \lambda^{-2}$, with $\sigma$ in $\mu s^{-1}$ and $\lambda$ in nm [94, 95]. In the $YBa_2Cu_3O_{6+y}$ system, this very simple treatment of muon data gives values of $\lambda_{ab}$ that are typically 20% or more larger than the single crystal data reported here [89, 90, 94, 96]. The resulting underestimate of the superfluid density, together with the problematic $\hat{ab}$-plane anisotropy and field-dependent effects, mean that the Meissner state single crystal penetration depths reported here can offer a clearer picture of the doping dependence of the superfluid density in the $CuO_2$ planes.

The microwave ESR results are presented in Fig. 3.12, plotted as $T_c$ versus $1/\lambda^2(T \rightarrow 0) \propto n_s/m^*$ for both in-plane crystallographic directions, along with error bars. The linear relationship is clearly not supported here, even when one discounts the data on $YBa_2Cu_3O_{6.993}$ which is slightly past optimal doping. In particular, the $\hat{a}$-axis phase stiffness, which should avoid contributions associated with the CuO chains, is very far from a relationship of the form $T_c \propto 1/\lambda_a^2$ for the $T_c$=56 K and $T_c$=75 K samples since it does not extrapolate to the origin.

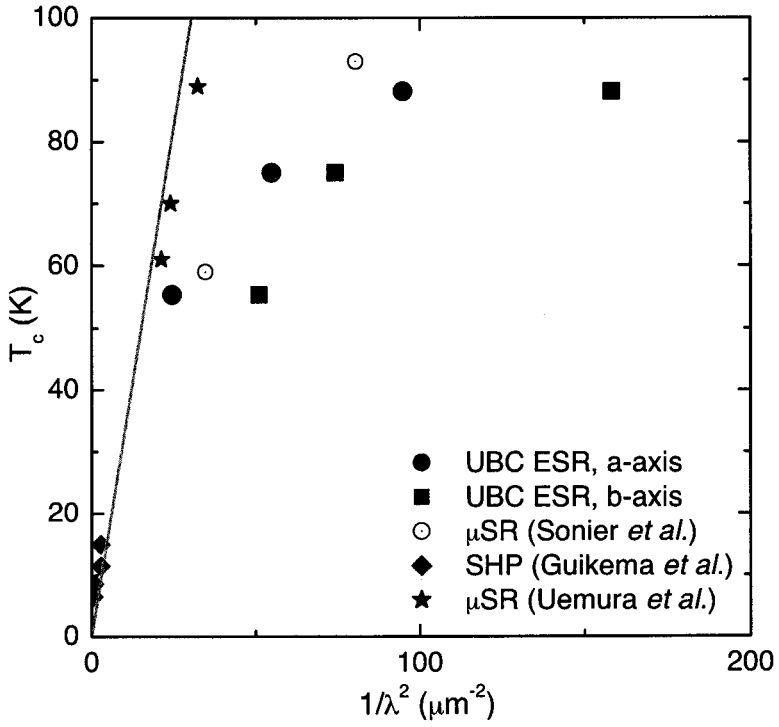


Figure 3.13: Measurements of the in-plane anisotropic absolute penetration depth $\lambda$ in $YBa_2Cu_3O_{6+y}$ for y=0.52, y=0.77 and y=0.995 plotted as $T_c$ versus superfluid phase stiffness ($\propto 1/\lambda^2$). Also shown are the $\mu SR$ results of Sonier *et al.* [86] and Uemura *et al.* [90], as well as the scanning Hall probe (SHP) results of Guikema *et al.* [66] at very low doping. The grey line is $T_c$=(3.3 K $\mu m^2)\lambda_{ab}^{-2}$ (Eq. 3.9), an estimate of the upper bound on $T_c$ obtained from the consideration of phase fluctuations by Emery and Kivelson [97].

Figure 3.13 compares the microwave ESR results to the $\mu SR$ results of Sonier *et al.* on $YBa_2Cu_3O_{6+y}$ single crystals, $\mu SR$ results of Uemura *et al.* on polycrystalline $YBa_2Cu_3O_{6+y}$, and to the scanning Hall probe results of Guikema *et al.* on underdoped $YBa_2Cu_3O_{6+y}$single crystals [66]. Excluding the results of Uemura *et al.* for the reasons discussed above, the data in the plot suggest a strongly *sublinear* dependence of $T_c$ on $1/\lambda_a^2$. Interestingly, the latest muon spin relaxation studies in this doping range by Tallon *et al.* [96] also suggest this sublinear relationship.

Emery and Kivelson have cited the result $T_c \propto 1/\lambda^2$ as evidence that phase fluctuations play a central role in setting $T_c$ on the underdoped side of the cuprate phase diagram [97]. Within this scenario, a consequence of the low superfluid density is that there is a maximum temperature $T_\theta^{\max}$ at which thermal phase fluctuations of the order parameter destroy superconductivity. They were able to provide a quantitative estimate of this temperature which gave reasonable agreement with the experimental results of Uemura *et al.*:

$$T_\theta^{\max} = A\frac{\hbar^2 n_s(0)a}{4m^*} = A\frac{(\hbar c)^2 a}{16\pi e^2 \lambda(0)^2}. \tag{3.9}$$

The parameters for $YBa_2Cu_3O_{6+y}$ are as follows: A is a dimensionless number $\approx 1$ that sets a short-distance cutoff in the Hamiltonian, taken to be 0.9 for definiteness for the quasi-two-dimensional cuprates, and a=max$(d, \xi_c)$ where $d$ is the average interplane spacing and $\xi_c$ is the $\hat{c}$-axis superconducting coherence length ($d > \xi_c$ for $YBa_2Cu_3O_{6+y}$ at these dopings). Evaluation of this expression yields the result $T_c$=(3.3 K $\mu m^2)\lambda_{ab}^{-2}$ which is shown to overestimate $T_c$ for all values of $1/\lambda^2$ in Fig. 3.13. From this we conclude that other factors must contribute to the determination of the critical temperature.

An obvious candidate is thermal excitation of nodal quasiparticles, discussed by Prohammer and Carbotte [98], Wen and Lee [99, 100] and Scalapino [101], which give rise to the linear temperature dependence of $\lambda(T)$ and rapidly deplete the superfluid density as temperature rises. More recently, Herbut and Case [102] have also argued in a general way that the observed sublinear scaling of $T_c$ with $\rho_s(0)$ in $YBa_2Cu_3O_{6+y}$ can be explained by the consideration of nodal quasiparticles, in addition to the vortex fluctuation physics near $T_c$. However, the central puzzle regarding the correlation between the absolute superfluid density and $T_c$ still remains in such a scenario. As the doping decreases, the zero temperature value of the superfluid density becomes much smaller, so that it becomes easy for quasiparticle excitations, in addition to fluctuations, to drive the material normal at a lower $T_c$.

To summarize, we have developed a novel zero field microwave ESR method that has produced a completely new set of accurate measurements of the anisotropic $\lambda(T \rightarrow 0)$ for $YBa_2Cu_3O_{6+y}$ single crystals at doping levels corresponding to three ordered phases. The results show significant discrepancy with some of the results obtained previously by other techniques, and we have outlined reasons why this may be so. In particular, we do not observe the widely-accepted result of a linear relationship between $T_c$ and $\rho_s(0)$. The new results, coupled with measurements of $\Delta\lambda(T)$, will provide an important opportunity to carefully revisit the results on doping dependence of the the temperature dependent superfluid density.

# Chapter 4

# Spectroscopy of $d$-Wave Quasiparticles in $YBa_2Cu_3O_{6+y}$

There remain many unanswered questions about the physics of the superconducting cuprates. A serious issue in the field of high temperature superconductivity is that many experiments have produced contradictory results due to the innate complexity both of the materials themselves and of the techniques required to examine their properties. The objective of the present microwave spectroscopy study is to produce a detailed experimental study of the best available samples of $YBa_2Cu_3O_{6+y}$ in one of the regions of the phase diagram which is best understood — the $d$-wave superconducting state. Many features of this state suggest that conventional Bardeen-Cooper-Schrieffer [3] theory, modified to account for $d$-wave pairing, is capable of describing the physics. Our intent is to carefully appraise this through examining the details of the way in which the charge excitations from the $d$-wave groundstate are scattered elastically from impurities through measurements of the microwave conductivity. Until now, a disturbing inconsistency has existed between the models for the microwave conductivity in this region and the available experimental data [30]. The quest to investigate this further has been the principal motivator in the development of the highly sensitive broadband microwave spectrometer described in Chapter 2 of this dissertation.

In this work we have succeeded in providing measurements of $\sigma_1(\omega, T)$ that reveal, for the first time, the cusp-shaped spectra expected for weak-limit impurity scattering in a clean $d$-wave superconductor. This discovery is the combined product of the new experimental technique, capable of probing the microwave spectrum in unprecedented resolution, with the production of extremely high quality single crystal samples of $YBa_2Cu_3O_{6+y}$, where even the off-plane CuO chain oxygen atoms are highly ordered. These samples have quasiparticle scattering rates that are low enough that the bulk of the spectrum lies within the range of the 21 GHz spectrometer. The results in this chapter are presented chronologically, starting with measurements of ortho-II ordered $YBa_2Cu_3O_{6.52}$ which were performed in 2000 and followed by those on fully-doped $YBa_2Cu_3O_{6.99}$ performed in 2002. This study has been previously published in a more concise form [103], but the results are updated here using the newly measured absolute values of $\lambda(T \rightarrow 0)$ presented in Chapter 3 of this thesis. In the present chapter, we focus our discussion on the $\hat{a}$-axis electrodynamic response, although broadband measurements of the $\hat{b}$-axis surface resistance will also be presented. These later results have recently been used by Richard Harris to help analyze the anisotropic transport in $YBa_2Cu_3O_{6+y}$ introduced by the presence of the CuO chains [104].

## 4.1 Electrodynamics of the Superconducting State

Microwave techniques have been applied to the $YBa_2Cu_3O_{6+y}$ system since the early days of the discovery of its superconductivity, and have produced key results concerning both the behaviour of the superfluid density, as well as the dynamics of the charged excitations from the superconducting condensate. High precision penetration depth measurements in 1993 by Hardy *et al.* [19] on high-quality single crystals were the first to reveal a linear temperature dependence of the superfluid density, thus providing a key piece of evidence that there were line nodes in the superconducting energy gap function. This understanding was furthered by the theoretical work of Hirschfeld, Puttika and Scalapino [24, 26] in which they showed that the low energy density of states in a *d*-wave superconductor could be strongly modified by the presence of pair-breaking impurities without strongly suppressing $T_c$, as discussed in Chapter 1 of this thesis. More specifically, they showed that a $T^2$ temperature dependence of $\Delta\lambda(T)$ at low temperatures was a consequence of the presence of unitarity-limit scattering centres. This helped to explain why some of the earlier measurements of $\Delta\lambda(T)$ on thin films had reported results other than $T$-linear. These ideas were further corroborated by the 1994 measurements of Bonn *et al.* [22] where microwave surface impedance measurements on $YBa_2Cu_3O_{6+y}$ samples intentionally doped with impurities (below the 1% level). When Zn was used as the dopant, $\Delta\lambda(T)$ developed the quadratic behaviour expected for strong impurity scattering, however comparable amounts of Ni impurities had no such effect. This was explained by the fact that, although both impurities substitute into the planar Cu site, Zn is in a non-magnetic ionization state, unlike Cu and Ni in the $YBa_2Cu_3O_{6+y}$ environment, and hence acts as a pair-breaking impurity. More recent scanning tunneling microscopy measurements on impurities in $Bi_2Sr_2CaCu_2O_{8+\delta}$ have confirmed these conclusions [105, 106].

Another early result was that of Nuss *et al.* [107] in 1991 who measured the conductivity of $YBa_2Cu_3O_7$ thin films using terahertz spectroscopy over the frequency range 0.5 THz to 2.5 THz. They observed a peak in $\sigma_1(T)$ that was attributed to a strong decrease in inelastic quasiparticle scattering rather than to a BCS-like coherence peak that occurs in a fully-gapped superconductor. Shortly thereafter, the low frequency microwave work of Bonn *et al.* [108, 109] showed a similar peak in $\sigma_1(T)$ that was conjectured to be the result of a competition between the rapid increase in quasiparticle lifetime $\tau$ and the decaying quasiparticle density $n_n(T)$ as the temperature was reduced. This analysis was carried out within the context of a Drude model characterized by an energy-independent scattering rate, despite the absence of low frequency spectroscopic information that could confirm its applicability. Other transport measurements including thermal conductivity and higher frequency electromagnetic measurements have drawn similar conclusions.

More recently, microwave measurements performed by the UBC superconductivity group have confirmed and extended these earlier findings, made possible by the advent of higher purity $YBa_2Cu_3O_{6+y}$ crystals grown in $BaZrO_3$ crucibles and the development of a sufficient number of fixed-frequency cavity perturbation systems to

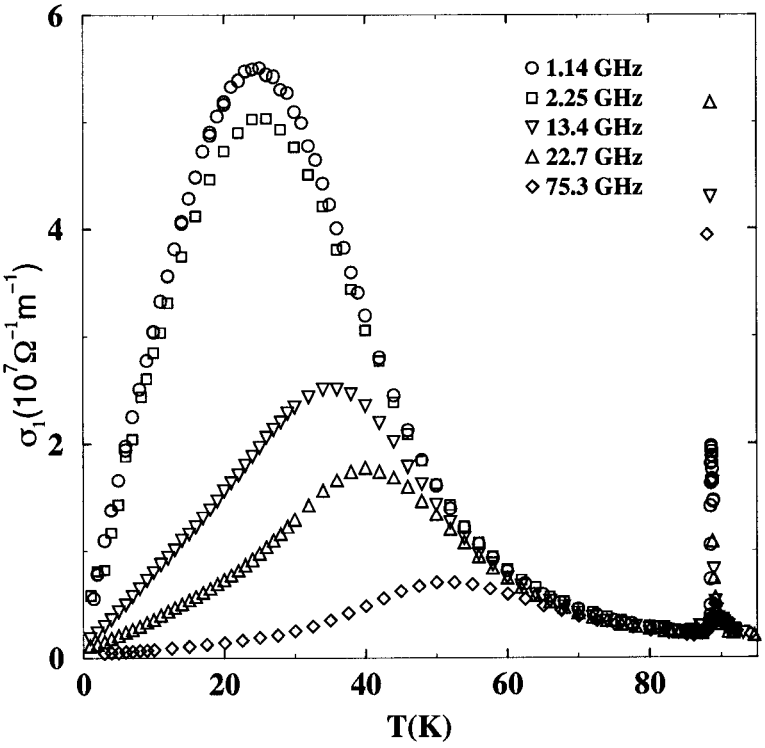


Figure 4.1: Cavity perturbation measurements of Hosseini *et al.* of the microwave conductivity over the range 1 GHZ to 75 GHz for $YBa_2Cu_3O_{6.993}$ plotted as a function of temperature. We point out that the absolute magnitude of $\sigma_1$ calculated from $R_s$ measurements is highly sensitive to the choice of $\lambda(T \rightarrow 0)$ (since $\sigma_1 \propto 1/\lambda^3$). The data in this plot uses $\lambda$ taken from infrared measurements to be 160 nm [30], whereas our new microwave ESR result of Chapter 3 is 103 nm.

map out a coarse microwave conductivity spectrum [30]. In particular, five superconducting resonators operating between 1 GHz and 75 GHz were used to examine the surface impedance of *the same single crystal sample* of fully-doped $YBa_2Cu_3O_{6.993}$, over the range 2 K to 100 K. The resulting conductivity curves are shown in Fig. 4.1 where the large peak in $\sigma_1(T)$ below 50 K is evident, as is the strong frequency dependence in the microwave region. Note the sharp peak in the curves at $T_c$=89 K attributed to superconducting fluctuations [110, 111], as well as the large, broad peak which moves to higher temperatures as the measurement frequency is increased. Figure 4.2 shows the five discrete frequency points at three representative temperatures plotted as conductivity spectra, along with fits to a Drude model that capture the features of the data rather well. Although not shown in the plot, the uncertainty in the fits becomes large at higher temperatures (above ~50 K) where the conductivity peak broadens out of the experimental bandwidth. The inset shows the temperature dependent quasiparticle scattering rate $\tau^{-1}$ derived from these fits, which is seen to decrease rapidly below $T_c$ and saturate at a constant value of $0.6\times10^{11}$ $s^{-1}$ at low

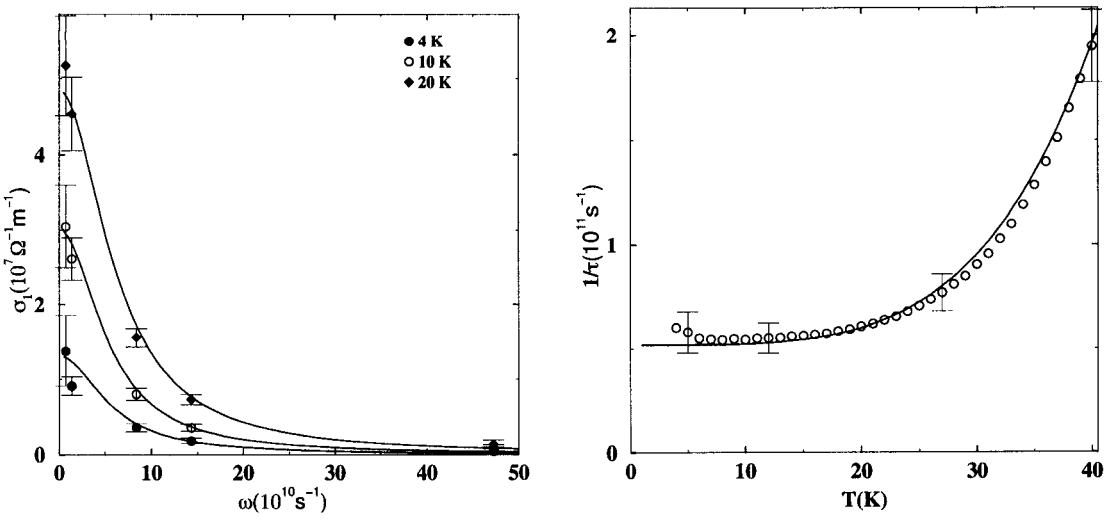


Figure 4.2: Left panel: Drude fits to the conductivity data of Hosseini *et al.* spanning 1 GHZ to 75 GHz for $YBa_2Cu_3O_{6.993}$ plotted as a function of frequency at three representative temperatures. Right panel: The quasiparticle scattering rate $\tau^{-1}$ that characterizes the width of the Drude lineshapes.

temperature, corresponding to a width of approximately 9 GHz. With a value of the Fermi velocity of $v_f = 2 \times 10^7$cm/s, this implies a rather long quasiparticle mean free path of 4 $\mu$m. Various proposals for understanding the mechanism responsible for the precipitous drop in $\tau^{-1}$ upon entering the superconducting state have been presented. The task is to understand the physics of the inelastic quasiparticle scattering processes, which most likely also play a role in the pairing interaction. One candidate that does a good job of fitting the data was put forward by Walker and Smith in which nodal quasiparticle-quasiparticle scattering generates the strongly-temperature-dependent scattering rate via an Umklapp mechanism [112].

At sufficiently low temperatures, the inelastic scattering processes that control the transport at high temperature subside and the system enters a regime where the elastic scattering of nodal quasiparticles from static disorder can be explored. In the measurements of Hosseini *et al.*, the temperature independence of $\tau^{-1}$ at the lowest temperatures was interpreted as the result of reaching an impurity-limited regime. From a theoretical perspective this is problematic because an *energy independent* $\tau$ does not come out in a straightforward way from models for the electrical conductivity in a *d*-wave superconductor [113].

These puzzling features have received considerable theoretical attention and some success in fitting to the data has been achieved by a number of approaches including: extending the SCTMA work to include the effects of order parameter suppression at the impurity site [114], considering scattering from twin boundary remnants [115], and allowing for intermediate values of the impurity scattering strength (*i.e.* phase shift) [25]. The strong frequency dependence of the conductivity observed in the microwave region, and the apparent discrepancy between the data and the theoreti-

cal predictions, begged for the continuous-frequency measurement of the absorption across a broad microwave range. The apparatus described in Chapter 2 of this thesis was developed specifically to satisfy this need.

## 4.2 Ortho-II Ordered $YBa_2Cu_3O_{6.52}$

### 4.2.1 Ortho-II Surface Resistance

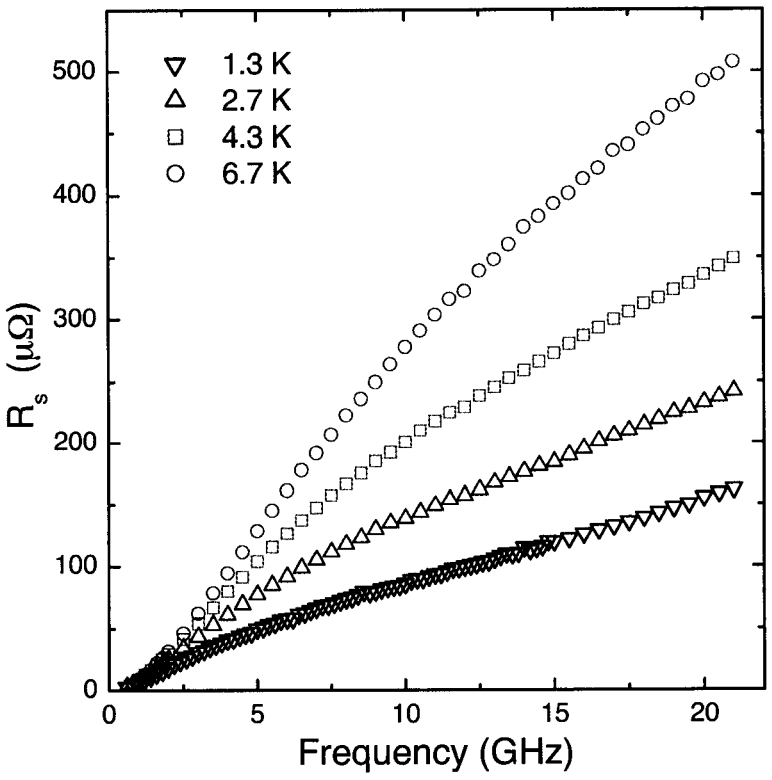


Figure 4.3: Low temperature surface resistance data for the $\hat{a}$-axis direction of ortho-II ordered $YBa_2Cu_3O_{6.52}$ measured with the broadband bolometric apparatus.

As discussed in Section 1.5, Ruixing Liang has recently produced ultra high purity $YBa_2Cu_3O_{6.52}$ single crystals having highly-ordered CuO chain oxygen atoms [35]. Figure 4.3 shows low temperature bolometric measurements of $R_s(\omega, T)$ for $\hat{a}$-axis currents in a sample of this compound having $T_c$=56 K. The particular sample studied here has dimensions $(a \times b \times c) = (1.25 \times 0.96 \times 0.010)$ mm$^3$. The measurements span the operating range of the experiment, 0.6 GHz to 21 GHz, and the experimental uncertainties are given in Section 2.3.

### 4.2.2 Extraction of $\sigma_1(\omega)$ from $R_s(\omega)$ Measurements

In this section, the way in which the microwave conductivity spectrum of a superconductor can be obtained from a measurement of its frequency-dependent surface resistance is discussed. This process is similar to the extraction of conductivity spectra in the infra-red frequency range from reflectance measurements. In both cases, one begins with incomplete information about the electrodynamic response: the bolometric technique described in this paper measures only the *resistive* part of the surface impedance; and optical techniques typically obtain the magnitude, but not the phase, of the reflectance. However, the conductivity $\sigma \equiv \sigma_1 - \mathrm{i}\sigma_2$ is a causal response function, and its real and imaginary parts are related by a Kramers–Krönig transform:

$$\sigma_2(\omega) = \frac{2\omega}{\pi}\mathcal{P}\int_0^\infty \frac{\sigma_1(\Omega)}{\Omega^2 - \omega^2}\mathrm{d}\Omega, \tag{4.1}$$

where $\mathcal{P}$ denotes the principal part of the integral. At first sight we seem to have replaced one uncertainty, incomplete knowledge of the phase, by another, the finite frequency range over which the measurements have been made. However, a suitable extrapolation of the data out of the measured frequency range is usually possible and makes the transform a well-defined procedure in practice. Often, a model form for $\sigma(\omega)$ is assumed that automatically provides both $\sigma_1(\omega)$ and $\sigma_2(\omega)$, as was done by Hosseini *et al.* who found a Drude conductivity spectrum to be sufficient [30]. This approach is unsatisfactory for the present work where the detailed spectrum is distinctly non-Lorentzian.

Recall from Eq. 1.8 that the microwave conductivity of a superconductor at finite frequencies can be written as

$$\sigma(\omega, T) = \sigma_{1N}(\omega, T) - \mathrm{i}\left[\sigma_{2N}(\omega, T) + \frac{1}{\mu_0\omega\lambda^2(T)}\right], \tag{4.2}$$

and that the surface impedance and conductivity are related via the expression

$$Z_s = R_s + \mathrm{i}X_s = \sqrt{\frac{\mathrm{i}\omega\mu_o}{\sigma}}. \tag{4.3}$$

Thus it is clear that finite frequency measurements of $R_s(\omega)$ will be determined by both the real and imaginary parts of the conductivity. However, one simplification occurs at temperatures well below $T_c$, where few thermally excited quasiparticles exist, and the low frequency reactive response is dominated by the superfluid. In this case, a good approximation to the relations is given by

$$\begin{aligned} R_s(\omega, T) &\simeq \frac{1}{2}\mu_0^2\omega^2\lambda^3(T)\sigma_1(\omega, T), \\ X_s(\omega, T) &\simeq \mu_0\omega\lambda(T). \end{aligned} \tag{4.4}$$

At higher frequencies and temperatures, a more complete treatment must account for quasiparticle contributions to field screening, which enter through $\sigma_{2N}(\omega, T)$. We

use an iterative procedure to obtain the quasiparticle conductivity spectrum $\sigma_{1N}(\omega)$, starting from the good initial guess provided by Eq. 4.4. The process goes as follows. A phenomenological form that captures the key characteristics of the dataset but has no physical motivation, namely

$$\sigma_1(\omega) = \sigma_0/[1 + (\omega/\Gamma)^y], \tag{4.5}$$

is fitted to the spectrum and used to extrapolate out of the measured frequency range. The Kramers–Krönig transform (Eq. 4.1) can then be applied to obtain $\sigma_{2N}(\omega)$. With $\sigma_{2N}(\omega)$ in hand, and with the superfluid contribution to $\sigma_2$ known from low frequency measurements of the magnetic penetration depth, a new extraction of the conductivity from the $R_s(\omega)$ data is made, this time using the *exact* expression, Eq. 4.3. The whole procedure is repeated to self-consistency. We find that the procedure is stable and converges rapidly, and is not sensitive to the details of the high-frequency extrapolation. Also, the corrections are quite small for the low temperature dataset shown in Fig. 4.6 where, at the highest temperature and frequency, they amount to a 7% change in $\sigma_1$.

In addition, two independent experimental checks give further assurance that this process obtains the correct conductivity spectra. First, note that Eq. 4.2 contains a complete expression for $\sigma_2$. Therefore, once we have measured the low frequency penetration depth and extracted the conductivity spectra from the $R_s(\omega)$ data, we can predict the temperature dependence of the surface reactance at *any* frequency and compare with experiments at higher frequency. We have made this comparison for $\sigma_2(\omega)$ at 22.7 GHz, with surface reactance data obtained on the same crystal, and find excellent agreement as seen in Fig. 4.4. We note that this is a frequency high enough for quasiparticle scattering to have a discernible effect on the surface reactance.

A second verification of the conductivity extraction procedure is its ability to predict the spectral weight that resides *outside* the frequency window of the measurement. A corollary of the Kramers–Krönig relation 4.1 is the oscillator-strength sum rule

$$\frac{ne^2}{m^*}(T) = \frac{2}{\pi}\int_0^\infty \sigma_1(\omega, T)\mathrm{d}\omega. \tag{4.6}$$

For a superconductor in the clean limit, the sum rule requires that any spectral weight depleted from the superfluid density $n_s(T)$ as the temperature is raised must reappear as an increase in the frequency-integrated quasiparticle conductivity. This comparison has been carried out using the phenomenological model for $\sigma_1(\omega)$ and is shown in the inset of Fig. 4.7 [103]. The good agreement in the temperature dependence of the superfluid and normal-fluid densities is a strong verification of both the analysis procedure *and* the bolometric technique.

### 4.2.3 Ortho-II Quasiparticle Conductivity

Due to the experimental difficulty in obtaining $\lambda(T \to 0)$ accurately, the microwave and optical literature on the cuprates retains rather significant uncertainties in the

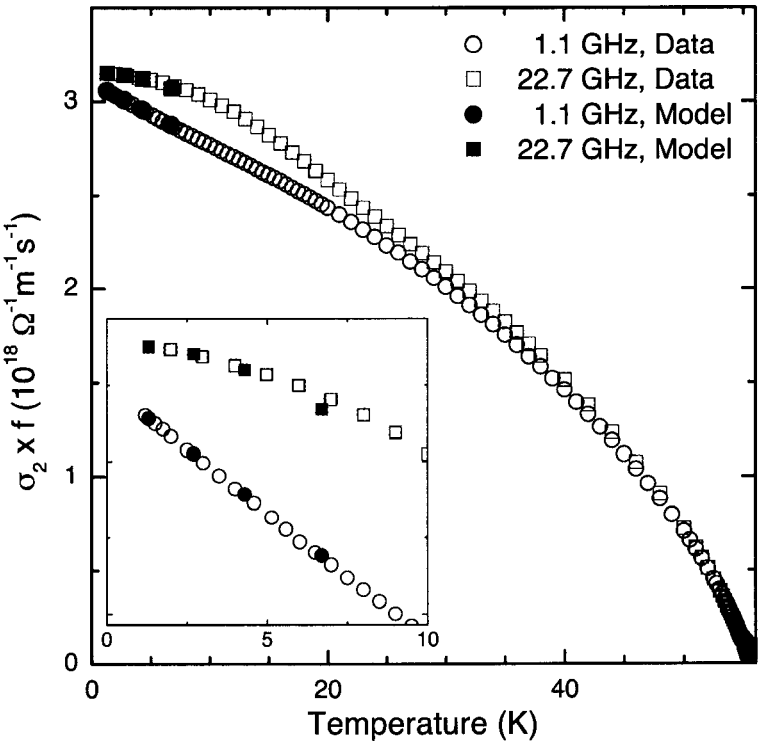


Figure 4.4: The imaginary component of Eq. 4.2, *i.e.* $\sigma_2(\omega, T)$, at 1.1 GHz and 22.7 GHz to demonstrate the effect of normal fluid screening. Cavity perturbation data (plotted as $\sigma_2 \times f$) are shown over the full temperature range and compared to the values calculated through the use of the Kramers–Krönig relation with fits to $\sigma_1(\omega, T)$ using Eq. 4.5. The very good agreement confirms that the model properly describes the quasiparticle conductivity. Because the cavity perturbation measurements cannot measure $\lambda(T \rightarrow 0, \omega)$ it was necessary to assume a value of $\lambda(T \rightarrow 0, 22.7GHz)$=200.5 nm to match the measured curve with the calculated value at 1.3 K. For this ortho-II sample, $\lambda(T \rightarrow 0, \omega \rightarrow 0)$=202 nm.

overall scaling of the data. For the present case of extracting $\sigma_1$ from measurements of $R_s$ and $\Delta\lambda(T)$, the result depends strongly on the value of $\lambda(T \rightarrow 0)$ since $\sigma_1 \approx 2R_s/(\mu_o^2\omega^2\lambda^3)$. Fortunately, this factor does not influence testing of the oscillator strength sum rule (Eq. 4.1) since the measurements of the temperature dependent superfluid density depend on $\lambda(T \rightarrow 0)$ in the same way: $\Delta(1/\lambda^2) \approx -\Delta\lambda/\lambda^3$. However, having accurate values for $\lambda$ is critical for the qualitative comparison between different dopings or crystallographic directions. For all calculations in this thesis, the new microwave ESR values are used as given in Table 3.2. For the present case of the ortho-II sample, the $\hat{a}$-axis value is $\lambda_a = 202 \pm 22$ nm.[1]

Figure 4.5 presents $\sigma_1(T)$ data extracted from cavity perturbation measurements at 1.1 GHz, 2.1 GHz, 2.9 GHz, 13.4 GHz , and 22.7 GHz. Note the features similar

[1]In the previous publication of this work [103], $\lambda_a = 260$ nm was used resulting in the reduction of the $\sigma_1$ spectra by an overall scale factor of 2.13.

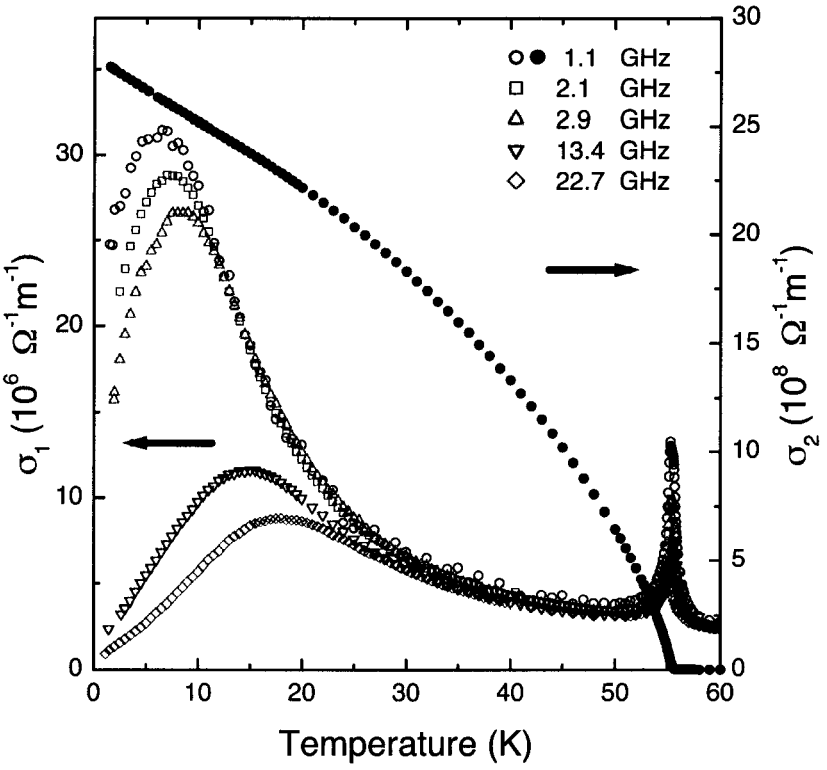


Figure 4.5: The temperature dependence of $\sigma_1$ and $\sigma_2$ of $YBa_2Cu_3O_{6.52}$ as measured by microwave cavity perturbation. $\sigma_1(T)$ was measured at five frequencies ranging from 1.1 GHz to 22.7 GHz. Low frequency $\sigma_2(T)$ data is also shown ($\lambda(T \rightarrow 0)$=202 nm). Note the fact that $\sigma_2 \gg \sigma_1$ throughout the superconducting state. Some features of the data are similar to those seen previously in the temperature dependence of overdoped $YBa_2Cu_3O_{6.99}$.

to the fully-doped data of Fig. 4.1 including the fluctuation peak at $T_c$=56 K as well as the much larger, frequency dependent peak at lower temperature. Above 30 K the curves overlap to within experimental uncertainty ($\approx$ 10%) indicating that the spectrum has broadened outside of the measurement window. A rather striking difference from the fully-doped case is the apparently large value of $\sigma_1$ for the low frequency frequency data at the lowest measurement temperature — for the 1.1 GHz ortho-II curve, the value at 2 K is roughly 5 times larger than the value at 50 K. Whether the conductivity remains large as the temperature is reduced further is an important question that we cannot presently answer. Also shown in the figure is the 1.1 GHz $\sigma_2(T)$ curve which reveals the linear form at low temperature expected for a clean $d$-wave superconductor and the non-mean-field behaviour near $T_c$ previously observed in high quality single crystals [110, 111].

Figure 4.6 depicts the real part of the quasiparticle conductivity spectrum extracted from the low temperature broadband $R_s$ measurements of Fig. 4.3 using the procedure described in the previous section. The strong frequency dependence over intervals as small as 1 GHz (equivalent to $T \approx 0.05$ K) shows that the timescale as-

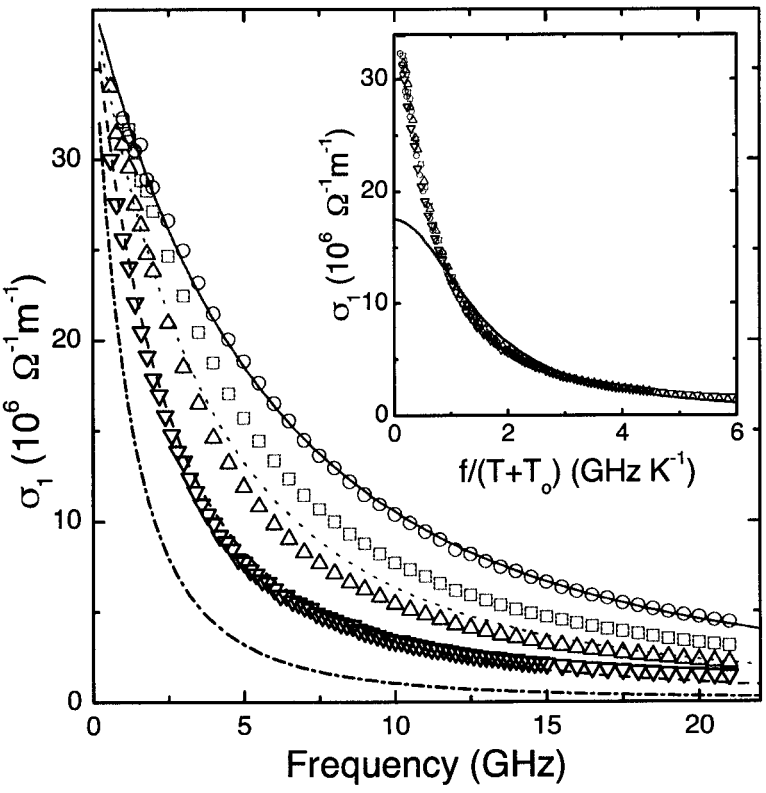


Figure 4.6: The low temperature evolution of the quasiparticle conductivity spectrum $\sigma_1(\omega, T)$ extracted from the surface resistance data of Fig. 4.3. The solid curve is a fit to the 6.7 K data with the Born-scattering model, but the dashed curves — predictions for the lower three temperatures — show that the model fails to capture the observed temperature dependence. The inset reveals that the data obey an unusual scaling; $\sigma_1(\omega, T) = \sigma_1(\omega/[T + T_0])$ with $T_0 = 2.0$ K. The Drude fit in the inset illustrates the inadequacy of the Lorentzian lineshape.

sociated with the scattering of the low-energy quasiparticles in these extremely clean samples falls within our microwave bandwidth. It is immediately apparent that the data have a non-Lorentzian, cusp-like shape which is very different from the data of Hosseini *et al.* for fully-doped $YBa_2Cu_3O_{6.99}$ (Fig. 4.2). Rather, the spectra show an approximately temperature-independent low frequency limit and a tail that falls more slowly than $1/\omega^2$. In these very highly-ordered and high-purity samples it is reasonable to expect that the scattering should be in the weak-limit. Superfluid density measurements that indicate clean *d*-wave behaviour down to the lowest temperature of 1.2 K support this (see inset, Fig. 4.7).

The solid curve in Fig. 4.6 shows a convincing fit to the 6.7 K data using the energy-averaged Drude form of Eq. 1.15 with $\tau^{-1}(\varepsilon) = \Gamma_B \varepsilon$, indicating that the overall shape of the spectrum is well-described by the weak-limit scattering calculation. The fit parameters are $\hbar\Gamma_B = 0.032$ and $ne^2\hbar/(m^*\Delta_0) = 1.26 \times 10^6\ \Omega^{-1}\mathrm{m}^{-1}$. The other curves are the predictions of the Born-limit model for the lower temperatures using the

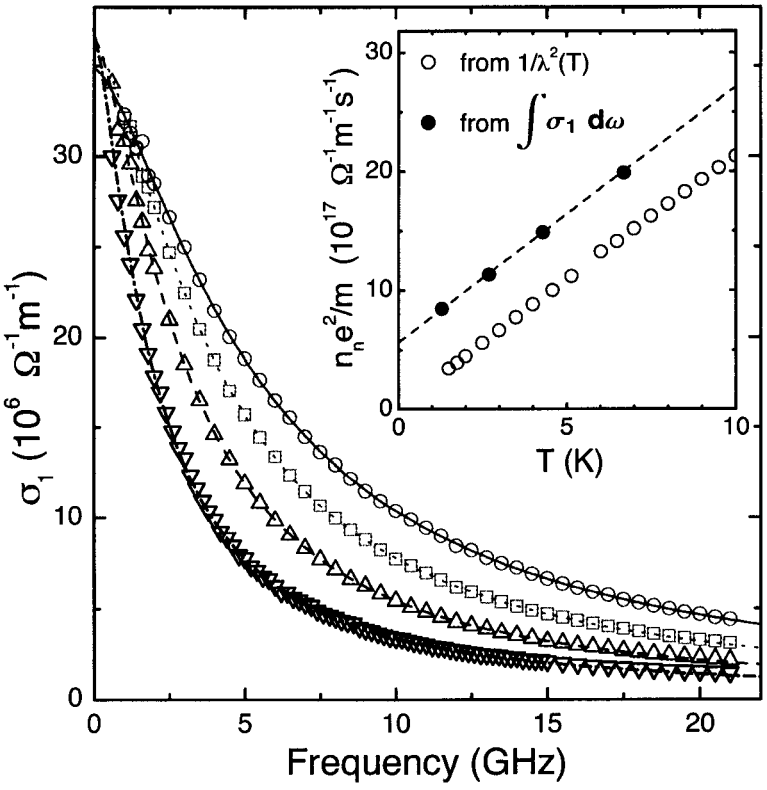


Figure 4.7: Phenomenological fits with Eq. 4.5 to the four conductivity spectra (same symbols as Fig. 4.3). The inset compares the normal fluid density $n_n e^2/m^*$ obtained by integrating Eqn. 4.5 with the loss of superfluid density inferred from 1.1 GHz $\Delta\lambda(T)$ data. The dashed line has the slope of the open symbols, and the agreement indicates that the normal-fluid and superfluid spectral weight obey the conductivity sum rule, although a residual normal fluid term is implied.

parameters from the 6.7 K spectrum fit. The temperature independent $\sigma_1(\omega \to 0)$ and a tail that falls more slowly than $1/\omega^2$ are features exhibited by the Born scattering model, in agreement with the data. However, it is clear that this model progressively underestimates the spectral weight as temperature is reduced, and thus a global fit for all temperatures is significantly less satisfactory. The close coincidence of the *predicted* 2.7 K spectrum and the *observed* 1.3 K data shows that the data is scaling, but not directly as $\omega/T$ as required by the model. This is confirmed in the inset of Fig. 4.6 where the $\sigma_1(\omega, T)$ data are shown to scale very well as $\omega/(T + T_0)$ with $T_0$=2.0 K. Hence, it is concluded that the weak-scattering limit model does indeed capture the spectral linshape, but the SCTMA model's requirement that the spectral weight vanish as $T \to 0$ leads to disagreement.

As discussed previously, considerable insight into both the shape of $\sigma_1(\omega)$ and the internal consistency of the data can be gained through fitting with a purely phenomenological model that allows for the observed scaling. Here, the form of Eq. 4.5 is adopted because it captures the Born-lineshape features seen in the data, namely

the cusp-like shape and high frequency tail. Figure 4.7 shows the fits to individual spectra using this model where the parameters $\sigma_o$ and $y$ remain relatively constant, with average values of $3.56(\pm 0.11) \times 10^7\ \Omega^{-1}m^{-1}$ and $1.45(\pm 0.06)$ respectively. The parameter $\Gamma$ varies approximately linearly in temperature with fit values 12.1, 19.2, 26.3, and $35.0 \times 10^9\ s^{-1}$. Although these fits also suggest the unusual $\omega$–$T$ scaling, enforcing it in the model reduces the agreement in the spectral weight comparison. As discussed previously, integration of the fits provides the *absolute* temperature-dependent spectral weight associated with the normal fluid.

In the inset of Fig. 4.7, this normal fluid spectral weight is compared to the spectral weight lost from the superfluid as determined independently by the measurements of $\Delta\lambda(T)$ and the slopes agree to within 2%. Again it is emphasized that the excellent agreement verifies that our model not only fits the measured $\sigma_1(\omega)$ spectra, but also properly models the quasiparticle oscillator strength to higher frequencies beyond our bandwidth.

The offset apparent in the normal fluid density suggests a $T = 0$ residual normal fluid. Although the possibility that the observed oscillator strength is due to an *extrinsic* source cannot be completely ruled out, the adherence to the observed simple scaling down to the lowest temperature of 1.3 K is taken as strong evidence that this $\sigma_1(T \rightarrow 0)$ arises due to pair-breaking effects. A further discussion of this issue will be returned to in Section 4.5.

## 4.3 Fully-Doped $YBa_2Cu_3O_{6.99}$

### 4.3.1 Fully-Doped Surface Resistance

The discovery of a cusp-shaped spectrum for the low temperature conductivity of $YBa_2Cu_3O_{6.52}$ was surprising because the coarse spectra seen by Hosseini *et al.* in fully-doped $YBa_2Cu_3O_{6.99}$ were reasonably well described by simple Drude fits ($y = 2$ in Eq. 4.5) [30]. To investigate this apparent discrepancy further, broadband measurements were made on a crystal of the fully-doped material from the same generation as the ortho-II sample, thus having the same nominal impurity level. The $R_s(\omega, T)$ data for $\hat{a}$-axis currents in a sample having dimensions $(a \times b \times c) = (1.10 \times 0.83 \times 0.009)\ mm^3$ are presented in Fig. 4.8.

### 4.3.2 Fully-Doped Quasiparticle Conductivity

Figure 4.9 presents quasiparticle conductivity spectra for fully-doped $YBa_2Cu_3O_{6.99}$ sample extracted from the surface resistance data of Fig. 4.8 and fit with a Drude lineshape. The value of $\lambda_a(T \rightarrow 0) = 103 \pm 8$ nm was taken from Table 3.2. At the lowest temperatures, the Drude fits are poor because a cusp-like spectrum does indeed emerge, similar to that observed in the ortho-II case. This was not seen in the earlier measurements on fully-doped samples because of the limited coverage of the spectrum, and also because of the tendency towards a more Lorentzian lineshape above 4 K. This is evident in the progressively better fit to a Drude model with

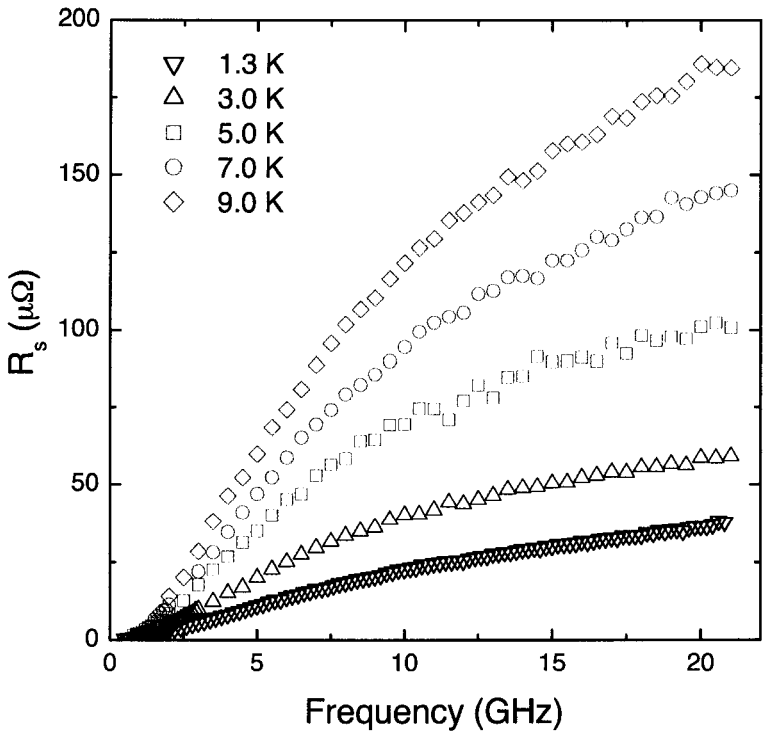


Figure 4.8: Low temperature surface resistance data for the $\hat{a}$-axis direction of fully-doped $YBa_2Cu_3O_{6.99}$ measured with the broadband bolometric apparatus.

increasing temperature, as seen in Fig. 4.9. Note that the 5 spectra do not scale in the manner seen for the $YBa_2Cu_3O_{6.50}$ sample, nor do the $\sigma_1(\omega \rightarrow 0)$ values indicate a temperature independent value. The low temperature scattering rate $\tau^{-1}$ was determined by Hosseini *et al.* to be approximately constant at $5.6(\pm 0.6) \times 10^{10}$ s$^{-1}$ below 20 K, and here we find an average value of $\tau^{-1} = 4.4(\pm 0.3) \times 10^{10}$ s$^{-1}$ with the decrease likely due to continued improvements in sample purity. For the broadband data we also find that the integration of the Drude model captures the oscillator strength rather well, although at our lowest temperatures the fits are too poor for us to comment upon an extrapolated residual value (see the inset of Fig. 4.9). It is interesting to note that fits to the fully-doped spectra using the phenomenological form of Eq. 4.5 result in a value of $\sigma_0$ that evolves with temperature, and a relatively constant value of $y$ having an average $\bar{y} = 1.7$ ($\pm 0.1$). In stark contrast to the ortho-II case, the scattering rate parameter $\Gamma$ shows little temperature dependence with $\overline{\Gamma} = 34$ ($\pm 6$) $\times 10^9$ s$^{-1}$. These observations explain why the Drude model has been capable of capturing the key features of the data. It turns out that a low temperature cusp-like shape that gives way to a broader spectral feature can be generated by the SCTMA model with an intermediate value of the scattering phase shift, as will be discussed in Section 4.5.

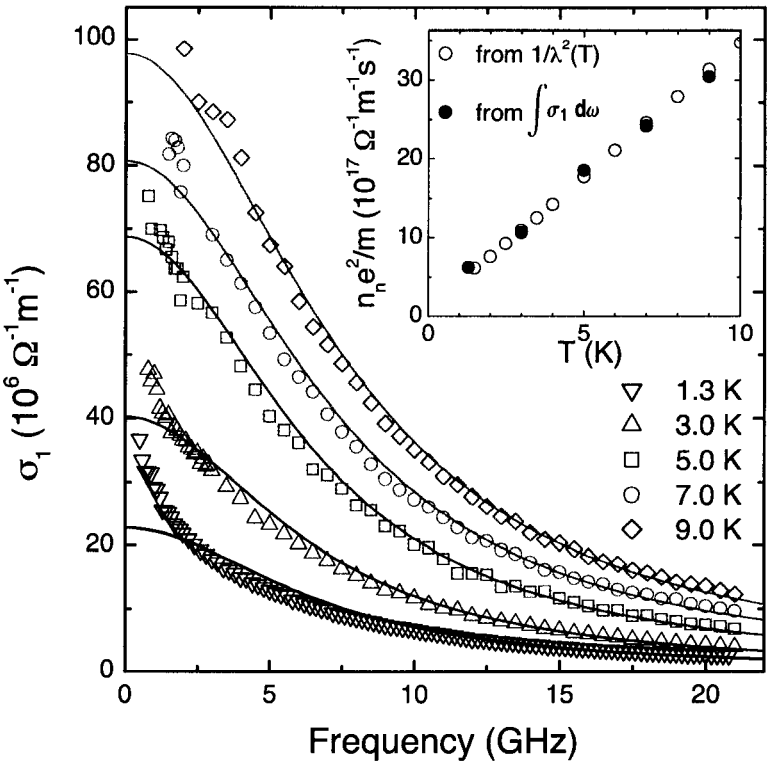


Figure 4.9: The conductivity spectrum of a fully-doped sample of $YBa_2Cu_3O_{6.99}$ in the $\hat{a}$-direction. The Drude fits to the spectra highlight the evolution from a cusp-like shape to a more Lorentzian lineshape with increasing temperature.

## 4.4 In-Plane Anisotropy

While the CuO chains in $YBa_2Cu_3O_{6+y}$ are generally regarded as an additional complication that is best avoided when testing the intrinsic superconducting properties in the cuprates, understanding their phenomenology is nevertheless important. Since $YBa_2Cu_3O_{6+y}$ crystals can be nearly completely detwinned, it is straightforward to measure the in-plane anisotropic transport properties. For the present bolometric system, this simply involves rotating the crystal by 90° and repeating the measurement. Such a measurement for $R_s(\omega, T)$ with $rf$ currents flowing in $\hat{b}$-axis direction for the ortho-II sample is presented in Fig. 4.10. At the present time, this quantity has not been measured for the high-purity fully-doped samples.

Measurements in the UBC superconductivity lab produced coarse $\hat{b}$-axis conductivity spectra at the same five frequencies as the $\hat{a}$-axis results of Hosseini *et al.*, and they were analyzed within a Drude model context [116]. However, it was found that unlike in the $\hat{a}$-direction, a very broad spectral component ($\sigma_1^{1D}$) was required to fit the data in addition to the narrow Lorentzian-shaped quasiparticle peak ($\sigma_1^{2D}$) and the conductivity was expressed in the form

$$\sigma_1^b = \sigma_1^{2D} + \sigma_1^{1D}. \tag{4.7}$$

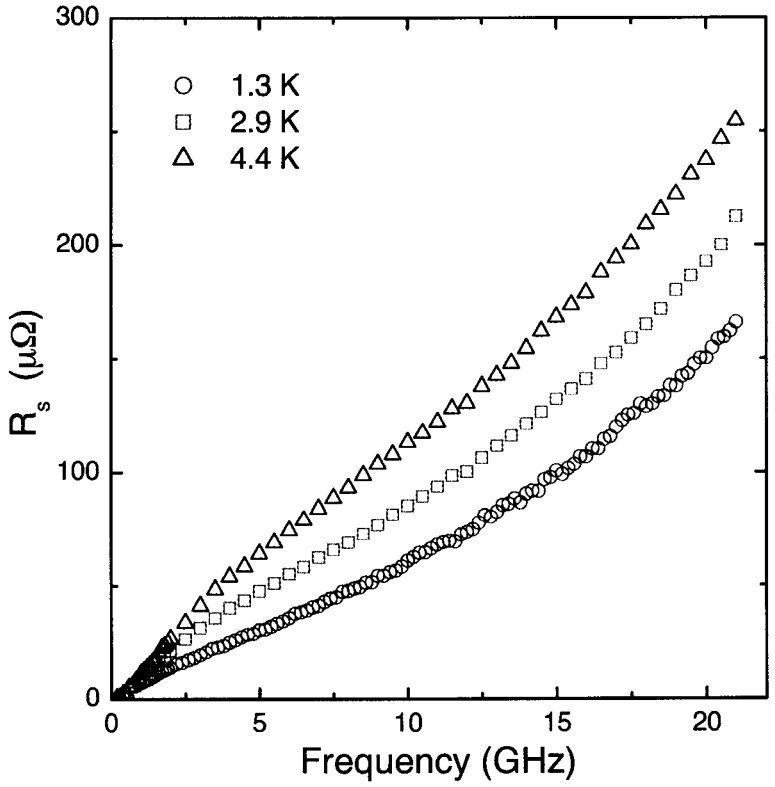


Figure 4.10: Broadband $R_s(\omega, T)$ of an ortho-II ordered sample of $YBa_2Cu_3O_{6.52}$ with screening currents flowing in the $\hat{b}$-direction.

The broad spectrum was attributed to a quasi-one-dimensional band resulting from the presence of the CuO chains which have a scattering rate that is significantly larger due to the remaining disorder. The $\sigma_1^{2D}$ was found to have a width $\tau^{-1}$ that had the same temperature dependence as that of the $\hat{a}$-axis direction. Thus, within this model, it was concluded that the two-dimensional scattering rate was indeed isotropic. However the planar spectral weight associated with the $\sigma_1^{2D}$ component revealed a peculiar anisotropy in which the $\hat{b}$-axis component was at least 1.5 times larger than that of the $\hat{a}$-axis [116].

Very recently, Richard Harris has revisited the analysis of the in-plane conductivity for fully-doped $YBa_2Cu_3O_{6+y}$ using the new absolute values of $\lambda(T \rightarrow 0)$ from Chapter 3, and also examined the ortho-II case [104]. A rather clear picture of the anisotropy has emerged from the combination of both broadband and cavity perturbation measurements on the same samples. In the fully-doped case of $YBa_2Cu_3O_{6.993}$, the earlier description using a two-component conductivity (Eq. 4.7) having plane and chain contributions still holds. However, the anisotropy in the spectral weight is no longer present to within experimental uncertainty when the new values of $\lambda(T \rightarrow 0)$ are used to set the absolute scale of $\sigma_1(\omega)$.[2] Thus the rather satisfying conclusion is reached that both the two-dimensional scattering rate *and* the quasiparticle spectral weight show no in-plane anisotropy for the fully-doped sample.

[2]The values used previously were $\lambda_a(T \rightarrow 0)$=160 nm and $\lambda_b(T \rightarrow 0)$=100 nm [116].

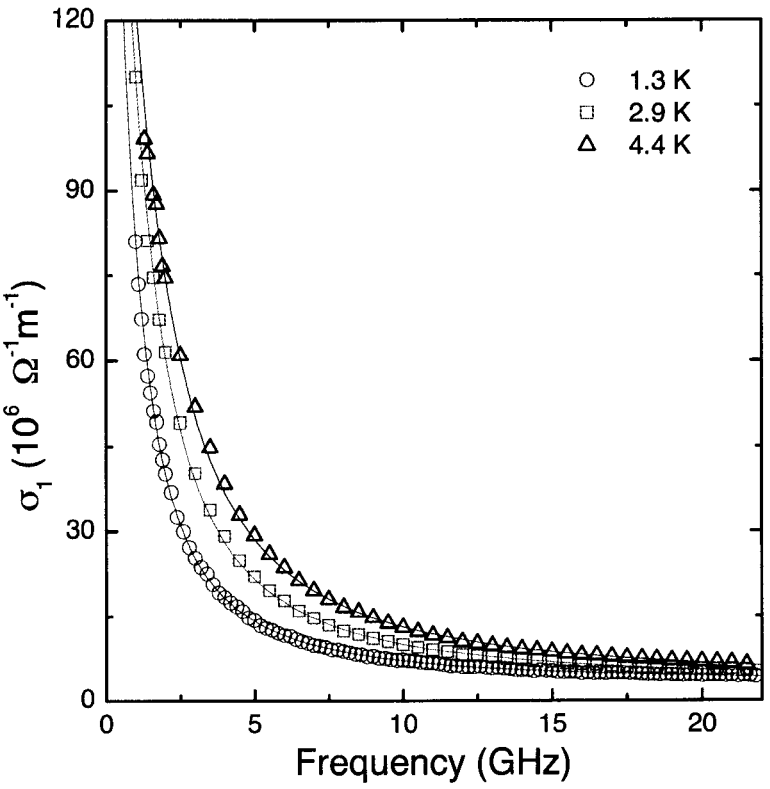


Figure 4.11: Broadband $\sigma_1(\omega, T)$ for ortho-II ordered $YBa_2Cu_3O_{6.52}$ with screening currents flowing in the $\hat{b}$-direction. Figure provided courtesy of R. Harris.

The story is more complicated for the ortho-II case. Attempting to fit the data with the simple procedure just described results in significant $\hat{a}$:$\hat{b}$ anisotropy in both the spectral weight and elastic scattering rate, although the inelastic scattering rate seemed roughly the same in the two directions. As a demonstration, the broadband ortho-II $\sigma_1(\omega, T)$ spectra extracted from the data in Fig. 4.10 with phenomenological fits (using Eq. 4.5 with an additional constant offset $\sigma_1^{1D}$). The result concluded from the fitting was that the influence of the periodic superlattice of CuO chain oxygen atoms on the electronic band structure must be considered. The ortho-II ordering produces a structure with alternating full and empty CuO chains, and thus a doubling of the effective unit cell is introduced (or halving of the first Brillouin zone). The detailed band structure analysis [116] argues that such a change in the topology of the Fermi surface can indeed provide the requisite additional feature of another term in the conductivity expression that allows the spectral weight to be distributed in a way that does not require anisotropy in the two-dimensional component. In total, there should be six different bands which contribute to the $\hat{b}$-axis conductivity. One important implication of this picture is that the Umklapp model for the inelastic quasiparticle scattering cannot be applicable since the doubled-unit-cell Fermi surface geometry does not allow such a process [116].

## 4.5 Discussion

We have presented quasiparticle conductivity spectra for under-doped and fully-doped samples of $YBa_2Cu_3O_{6+y}$. At the lowest temperatures, both samples reveal the cusp-like lineshape expected for weak-limit impurity scattering. The spectra exhibit a width on the order of 5 GHz at 1.3 K signifying very long quasiparticle scattering times and confirming the high quality of the $YBa_2Cu_3O_{6+y}$ crystals. In these very clean samples, we find that most of the spectral weight resides below our experimental frequency limit of 21 GHz at 1.3 K, but the increase in scattering as the temperature is raised quickly broadens the spectra. We note that many cuprate materials, such as $Bi_2Sr_2CaCu_2O_{8+\delta}$, have scattering rates that are orders of magnitude higher and require THz frequency techniques to probe their dynamics [117]. Despite our observation that the conductivity spectra do match the predicted theoretical lineshape, two main questions remain unanswered. First, why is the cusp-like shape only seen at the lowest temperature in the fully-doped sample, and second, what is the cause of the $T \rightarrow 0$ residual oscillator strength?

In an attempt to explain the phenomenology observed in the conductivity data, Richard Harris has performed a generalization of the SCTMA work of Hirschfeld *et al.* [24, 26] to include potentials of arbitrary scattering strength. The reader is referred to his Ph.D. dissertation for a more thorough treatment of this subject [104]. In this work, $\sigma_1(\omega, T)$ in a single band model can be expressed as

$$\sigma_1(\omega, T) = \frac{\alpha^2 n e^2}{m^* \Delta_o} \int d\omega \, \mathcal{F}\left[\Gamma_N, c, \tilde{\varepsilon}, \tilde{\xi}_k, \omega, T\right]. \tag{4.8}$$

Here, $\mathcal{F}[\ldots]$ is a function determined from the electrical Kubo formula [118], $\tilde{\varepsilon}$ is the renormalized internal frequency, $\Gamma_N$ is the 'normal' state electronic scattering rate, $c \equiv 1/\pi N_o V$ dictates the strength of the defect potential $V$ relative to $N_o$ (the normal state electronic density of states at the Fermi energy) and $\tilde{\xi}_k$ is the renormalized electronic dispersion. Note that all energies are written in units of temperature (K), and hence $\Delta_0$ has units of $s^{-1}$ throughout the present analysis. The prefactor $\alpha^2 n e^2/m^* \Delta_0$ controls the quasiparticle oscillator strength, where $\alpha$ represents the Ioffe-Millis charge renormalization [119]. This prefactor can be determined from experimental measurements of the slope of the temperature-dependent London penetration depth [113].

The most frequently-invoked limit of this model is unitary scattering ($c \rightarrow 0$) in which $\tau^{-1}(\varepsilon)$ is peaked at $\varepsilon = 0$ and decreases as $1/\varepsilon$ beyond an impurity bandwidth $\gamma \sim (\Delta_0 \Gamma_N)^{1/2}$. For $k_B T < \gamma$, this gives a quadratic temperature-dependence to both $\sigma_1$ and $\sigma_2$ above a universal limit $\sigma_{oo} = ne^2/(\pi m^* \Delta_0)$:

$$\sigma_1(\omega \rightarrow 0, T) \sim \sigma_{oo} \left[1 + \frac{\pi^2}{3}\left(\frac{k_B T}{\Gamma_N}\right)^2\right]. \tag{4.9}$$

In contrast, the underdoped sample has a temperature-independent $\sigma_1(\omega \rightarrow 0, T)$ that remains far above the expected universal limit $\sigma_{oo}$ [120]. We point out that this alone is not inconsistent with the limit of weak scattering where the onset for

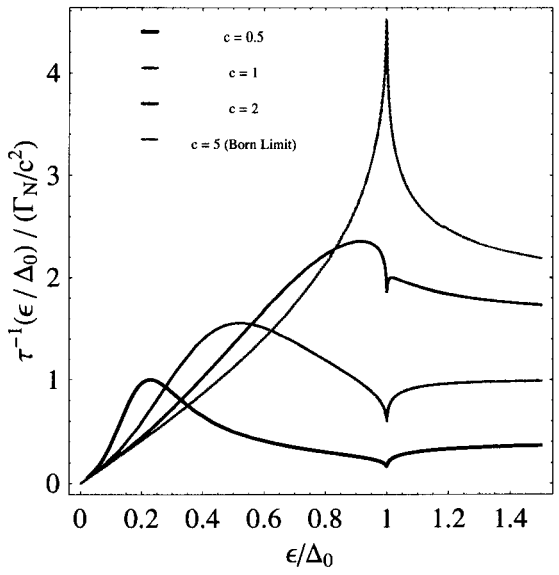


Figure 4.12: Quasiparticle scattering rate $\tau^{-1}$ for different values of $c$, the cotangent of the scattering phase shift ($\Gamma_N$ fixed). In the Born limit, $\tau^{-1}(\varepsilon) \propto N(\varepsilon)$ and is seen to have the characteristic $d$-wave form. As the impurity resonance moves down in energy, the enhancement of the scattering rate can be clearly seen.

$\sigma_{00}$ is expected to be exponentially small in temperature [26]. However, the search to simultaneously match the spectral lineshape and the oscillator strength leads us away from unitary scattering. For different values of the cotangent of the scattering phase shift, the scattering resonance peaks at $\varepsilon_{\rm peak} \neq 0$ and $\tau^{-1}(\varepsilon) \propto \varepsilon$ for small $\varepsilon$ (see Fig. 4.12). In this case, one obtains a *temperature-independent* low frequency form

$$\sigma_1(\omega \to 0, T) = \frac{\alpha^2}{2}\frac{ne^2}{m^*\Delta_0}\left(\frac{\Gamma_N}{\Delta_0 c^2}\right)^{-1} \tag{4.10}$$

valid over the range $T^* < T < 5\varepsilon_{\rm peak}$, where $T^*$ is an exponentially small energy [26]. This intermediate behaviour is seen at all temperatures in the underdoped data and may be present below ~3 K in the overdoped data (see Fig. 4.13). The value of $\Gamma_N/\Delta_0 c^2$ is fixed by the height of the cusp in $\sigma_1(\omega)$, since the quantity $\alpha^2 ne^2/2m^*\Delta_0$ can be determined separately from penetration depth measurements.

The parameter $c$ can be established by noting the upper temperature $T \sim 5\varepsilon_{peak}$ at which the limiting behaviour of Eq. 4.10 breaks down and a transition to a temperature-dependent $\sigma_1(\omega \to 0)$ can be observed; this is apparent in the overdoped data but we can only establish a lower bound on $\varepsilon_{peak}$ for the underdoped data (see Table 4.1). Thus all of the parameters in Eq. 4.8 can be established and used to generate the theoretical spectra shown in Figs. 4.13 [104]. The curves do a reasonable job of describing the overall features seen in the data. Upon closer examination however, we conclude that while the elastic point scattering model generates the correct qualitative features, the shift away from the Born-scattering limit does not produce the apparent residual oscillator strength observed in the data of Fig. 4.7. In

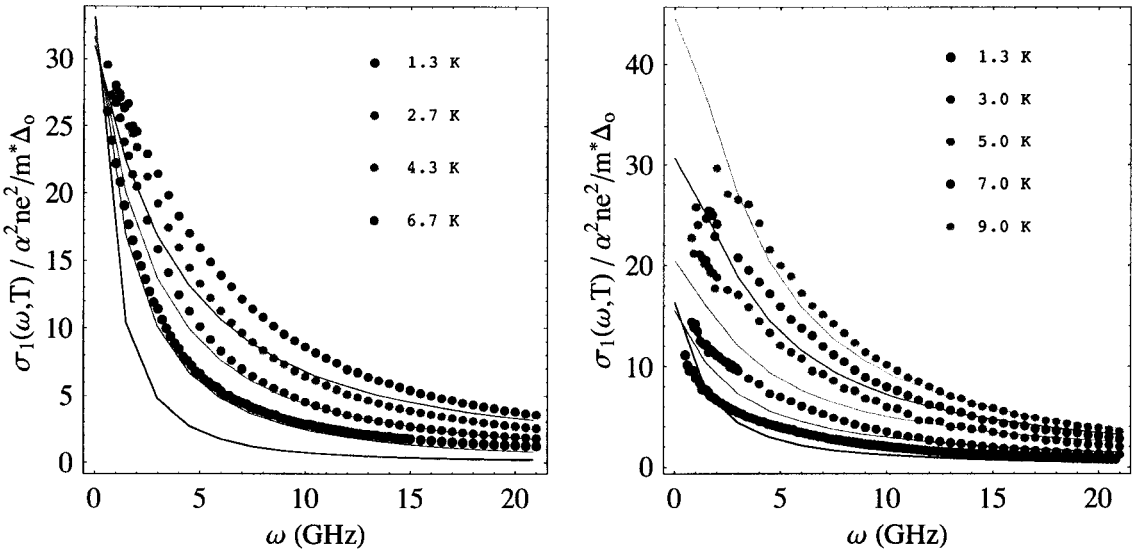


Figure 4.13: The quasiparticle conductivity due to elastic scattering from point-like Coulomb defects using the parameters given in Table 4.1. Left panel is ortho-II $YBa_2Cu_3O_{6.52}$ and right panel is fully-doped $YBa_2Cu_3O_{6.99}$ fit with a model for the elastic scattering of quasiparticles from point defects. The different phenomenology produced to characterize the two data sets is a result of using different values of the scattering phase shift. The fit parameters are given in Table 4.1. Figures provided courtesy of R. Harris.

response to the broadband microwave spectra, Schachinger and Carbotte have argued that the SCTMA with intermediate scattering strengths, neither Born nor unitary-limit, can give significant impurity-induced absorption while retaining a quasilinear temperature dependence of the superfluid density and cusp-like $\sigma_1(\omega)$ spectra [121]. However, Harris has pointed out that in that work, a very large impurity density was required to generate the offset in the spectral weight. Thus he has concluded that it is not possible to simultaneously produce the observed spectral weight and the $\sigma_1(\omega)$ lineshapes of the data using the SCTMA approach [104]. Furthermore, neither his efforts to attempt to model the effect of a more realistic spatial dependence for the impurity potential nor the inclusion of scattering from magnetic defects have provided the required behaviour. At UBC, we are currently underway with extending the broadband $R_s$ measurement techniques to 100 mK which will certainly provide further clues as to the nature of the impurity scattering mechanism. Experiments in which intentional dopants (*e.g.* Ni or Zn) are introduced into the latest generation of high-purity crystals will also be especially relevant. This may require some effort to ensure uniformity of the dopant atoms throughout the crystals.

In summary, we have provided the first highly detailed measurements of the quasiparticle conductivity spectrum in the disorder-dominated regime of an extremely clean *d*-wave superconductor. This regime has been accessed by using well-ordered

| Doping | $\alpha^2 ne^2/m^*\Delta_o$ | $\hbar\Delta_o/k_B$ | $\Gamma_N/\Delta_o c^2$ | $c$ | $\lambda(T \to 0)$ |
|---|---|---|---|---|---|
| Underdoped | $1.1 \times 10^6\,\Omega^{-1}\mathrm{m}^{-1}$ | 800 K | 1/70 | $\gtrsim 0.1$ | 202 nm |
| Overdoped | $3.0 \times 10^6\,\Omega^{-1}\mathrm{m}^{-1}$ | 400 K | 1/36 | 0.1 | 103 nm |

Table 4.1: Summary of the parameters used in the point-scattering calculation of R. Harris ($\Delta_o$ values taken from Ref. [122]).

crystals of very high purity, measured with a broadband microwave technique whose frequency range matches the very small quasiparticle scattering rate in the samples. A number of puzzling features remain, particularly the residual normal fluid inferred from extrapolations to $T = 0$, a phenomenon that is seen to a much greater degree in other cuprates [117, 123]. The cause of the evolution from a cusp-like spectrum to a more Lorentzian lineshape in fully-doped $YBa_2Cu_3O_{6.99}$ seems to suggest that intermediate scattering strengths are responsible for the transition. Nevertheless, the cusp-shaped conductivity spectra seen at low temperature *are* characteristic of Born-limit scattering. Additional physics might be needed to resolve the remaining puzzles, but the data presented here provide a simple starting point that is quite close to the expectation for nodal quasiparticles scattered weakly by impurities.

# Chapter 5

# Conclusions

At the heart of the work in this dissertation is the novel broadband microwave spectrometer developed during the course of the author's doctoral studies. This instrument has provided a flexible and powerful means of investigating the low temperature electrodynamics of superconducting samples, with the results on single crystal samples of $YBa_2Cu_3O_{6+y}$ included here to provide two results of key importance to the understanding of cuprate superconductivity.

The design of the broadband microwave spectrometer is presented in Chapter 2. It has a minimum detectable power of 1.5 pW at a base temperature of 1.3 K. This has allowed detailed measurements of the surface resistance of $1 \times 1$ mm$^2$ superconducting single crystal samples with surface resistance as low as 1 $\mu\Omega$. The frequency coverage of the apparatus spans 0.5 GHz to 21 GHz, where the low frequency limit is set by the vanishingly small absorption in the superconductor and the upper frequency limit corresponds to the propagation of higher order waveguide modes in the system. From a theoretical analysis of the power sensitivity of the bolometer, we expect that the instrument can be further improved by the use of more carefully selected temperature sensors that do not exhibit excess noise. Furthermore, these sensors should facilitate measurements to higher temperatures, allowing spectroscopy to be carried out at or near the critical temperature of the cuprate superconductors. At the present time, a system to extend the technique to milli-Kelvin temperatures is under construction at UBC.

In Chapter 3, an original method for measuring the absolute value of the magnetic penetration depth $\lambda$ in the Meissner state using zero field electron spin resonance spectroscopy is demonstrated. The result is a completely new set of accurate measurements of the anisotropic $\lambda(T \rightarrow 0)$ for $YBa_2Cu_3O_{6+y}$ single crystals at three doping levels corresponding to oxygen-ordered phases. The results are substantially different from most of the data in the literature, many of which are for polycrystalline samples and were made using measurement techniques that can be challenging to interpret. The previously obtained result of a linear relationship between $T_c$ and $\rho_s(0) \propto 1/\lambda^2$ *is not observed.* The new results do show that there is significant anisotropy in the in-plane superfluid density in $YBa_2Cu_3O_{6+y}$which becomes large when the CuO chains are nearly full. Revisiting previous microwave determinations of the temperature-dependent penetration depth will be informative, given that an accurate $\lambda$ value at $T \rightarrow 0$ is required in order to extract the evolution of the temperature dependent superfluid density.

Finally, convincing evidence is given in Chapter 4 that the behaviour of the charged excitations from the superconducting condensate is very similar to that expected for BCS $d$-wave nodal quasiparticles. The evidence is in the form of detailed

measurements of the microwave conductivity spectrum in the low temperature regime where the quasiparticle scattering dynamics are determined by their interaction with the remaining impurities in a high quality single crystals. These results have confirmed the earlier finding of Hosseini *et al* in fully-doped $YBa_2Cu_3O_{6.99}$ that the spectrum is well described by a Lorentzian line shape having a nearly temperature independent width, except at the lowest temperatures. The high resolution of the new measurements and the additional data on under-doped $YBa_2Cu_3O_{6.52}$ have allowed the detailed comparison with the relevant model for quasiparticle scattering from point-like defects. For the first time, many of the characteristic features of the model were seen in the microwave conductivity data. However, the data also indicate a feature not predicted by the self-consistent $t$-matrix approach, namely a residual normal fluid in the $T \rightarrow 0$ limit that remains unexplained.

# Bibliography

[1] H. K. Onnes, Leiden Comm. **120b, 122b, 124c** (1911).

[2] J. G. Bednorz and K. A. Müller, Z. Phys. **B64**, 189 (1986).

[3] J. Bardeen, L. N. Cooper, and J. R. Schrieffer, Phys. Rev. **108**, 1175 (1957).

[4] W. E. Pickett, Rev. Mod. Phys. **61**, 433 (1989).

[5] A. P. Mackenzie and Y. Maeno, Rev. Mod. Phys. **75**, 657 (2003).

[6] T. Timusk and B. Statt, Rep. Prog. Phys. **62**, 61 (1999).

[7] P. B. Allen, Z. Fisk, and A. Migliori, in *Physical Properties of High Temperature Superconductors, Vol. 1*, edited by D. Ginsberg (World Scientific, Singapore, 1989).

[8] B. Batlogg, H. Y. Hwang, H. Tagaki, H. L. Kao, J. Kwo, and R. Cava, J. Low Temp. Phys. **95**, 23 (1994).

[9] A. Hosseini, Ph.D. thesis, University of British Columbia (2002).

[10] R. Liang, D. A. Bonn, W. N. Hardy, J. C. Wynn, K. A. Moler, L. Lu, S. Larochelle, L. Zhou, M. Greven, L. Lurio, et al., Physica (Amsterdam) **383C**, 1 (2002).

[11] Y. S. Lee, F. C. Chou, A. Tewary, M. A. Kastner, S. H. Lee and R. J. Birgeneau, cond-mat\0309325, 2003.

[12] M. Tinkham, *Introduction to Superconductivity* (McGraw Hill, Inc. Toronto, Canada, 1996).

[13] F. and H. London, Proc. Roy. Soc. **A149**, 71 (1935).

[14] A. J. Berlinsky, C. Kallin, G. Rose, and A. C. Shi, Phys. Rev. B **48**, 4074 (1993).

[15] A. A. Abrikosov, *Fundamentals of the Theory of Metals* (North-Holland, New York, 1988).

[16] I. Kosztin and A. J. Leggett, Phys. Rev. Lett. **79**, 135 (1997).

[17] J. J. Chang and D. J. Scalapino, Phys. Rev. B **40**, 4299 (1989).

[18] C. C. Tsuei and J. R. Kirtley, Rev. Mod. Phys. **72**, 969 (2000).

[19] W. N. Hardy, D. A. Bonn, D. C. Morgan, R. Liang, and K. Zhang, Phys. Rev. Lett. **70**, 3999 (1993).

[20] P. W. Anderson, J. Phys. Chem. Solids **11**, 26 (1959).

[21] P. J. Hirschfeld and W. A. Atkinson, J. Low Temp. Phys. **127**, 289 (2002).

[22] D. A. Bonn, S. Kamal, K. Zhang, R. Liang, D. J. Baar, E. Klein, , and W. N. Hardy, Phys. Rev. B **50**, 4051 (1994).

[23] P. J. Hirschfeld and N. Goldenfeld, Phys. Rev. B **48**, 4219 (1993).

[24] P. J. Hirschfeld, W. O. Putikka, and D. J. Scalapino, Phys. Rev. Lett. **71**, 3705 (1993).

[25] C. T. Reick, D. Straub, and K. Scharnberg, J. Low Temp. Phys. **117**, 1295 (1999).

[26] P. J. Hirschfeld, W. O. Putikka, and D. J. Scalapino, Phys. Rev. B **50**, 10250 (1994).

[27] J. M. Byers, M. E. Flatté, and D. J. Scalapino, Phys. Rev. Lett. **71**, 3363 (1993).

[28] E. W. Hudson, S. H. Pan, A. K. Gupta, K. W. Ng, and J. C. Davis, Science **285**, 88 (1999).

[29] A. Yazdani, C. M. Howald, C. P. Lutz, A. Kapitulnik, and D. M. Eigler, Phys. Rev. Lett. **83**, 176 (1999).

[30] A. Hosseini, R. Harris, S. Kamal, P. Dosanjh, J. S. Preston, R. Liang, W. N. Hardy, and D. A. Bonn, Phys. Rev. B **60**, 1349 (1999).

[31] J. Zaanen, A. T. Paxton, O. Jepsen, and O. K. Andersen, Phys. Rev. Lett. **60**, 2685 (1998).

[32] Ruixing Liang, private communication.

[33] R. Liang, P. Dosanjh, D. Bonn, D. Baar, J. Carolan, and W. N. Hardy, Physica (Amsterdam) **195C**, 51 (1992).

[34] R. Liang, D. A. Bonn, and W. N. Hardy, Physica (Amsterdam) **304C**, 105 (1998).

[35] R. Liang, D. A. Bonn, and W. N. Hardy, Physica (Amsterdam) **336C**, 57 (2000).

[36] A. Erb, E. Walker, and R. Flukiger, Physica (Amsterdam) **258C**, 9 (1996).

[37] D. A. Bonn and W. N. Hardy, in *Physical Properties of High Temperature Superconductors, Vol. 5*, edited by D. Ginsberg (World Scientific, Singapore, 1996).

[38] R. J. Ormeno, D. C. Morgan, D. M. Broun, S. F. Lee, and J. R. Waldram, Rev. Sci. Instrum. **68**, 2121 (1997).

[39] M. A. Biondi and M. P. Garfunkel, Phys. Rev. **116**, 853 (1959).

[40] Speer type AR 7404-1200Ω resistor.

[41] Y. Matsuda, N. P. Ong, Y. F. Yan, J. M. Harris, and J. B. Peterson, Phys. Rev. B **49**, 4380 (1994).

[42] O. K. C. Tsui, N. P. Ong, Y. Matsuda, Y. F. Yan, and J. B. Peterson, Phys. Rev. Lett. **73**, 724 (1994).

[43] Y. Matsuda, M. B. Gaifullin, K. Kumagai, T. Mochiku, K. Kadowaki, and K. Hirata, Czech. J. Phys. **46**, 3203 (1996).

[44] M. B. Gaifullin, Y. Matsuda, N. Chikumoto, J. Shimoyama, K. Kishio, and R. Yoshizaki, Phys. Rev. Lett. **83**, 3928 (1999).

[45] D. L. Rubin, K. Green, J. Gruschus, J. Kirchgessner, D. Moffat, H. Padamsee, J. Sears, Q. S. Shu, L. F. Shneemeyer, and J. V. Waszczak, Phys. Rev. B **38**, 6538 (1988).

[46] A. Hosseini, S. Kamal, D. A. Bonn, R. Liang, and W. N. Hardy, Phys. Rev. Lett. **81**, 1298 (1998).

[47] J. M. Gildemeister, A. T. Lee, and P. L. Richards, Appl. Phys. Lett. **74**, 868 (1999).

[48] Cernox$^{TM}$ resistor, model CX-1050-BC (BC = Bare Chip option), was purchased from Lake Shore Cryotronics, Inc. of 575 McCorkle Boulevard, Westerville, Ohio 43082 USA.

[49] D. K. Schroder, *Semiconductor Material and Device Characterization* (John Wiley and Sons, New York, 1988).

[50] K. M. Itoh, E. E. Haller, W. L. Hansen, J. W. Beeman, J. W. Farmer, A. Rudnev, A. Tikhomirov, and V. I. Ozhogin, Appl. Phys. Lett. **64**, 2121 (1994).

[51] Haller-Beeman$^{TM}$ neutron transmutation doped resistor, model NTD-C was purchased from Haller-Beeman Assoc. Inc. of 5020 Santa Rita Rd., El Sobrante, CA 94803 USA.

[52] S. Sridhar and W. L. Kennedy, Rev. Sci. Instrum. **59**, 531 (1988).

[53] Dow Corning #976V High Vacuum Grease, Dow Corning Corporation P.O. Box 0994 Midland, Michegan 48686-0994 USA.

[54] 1.50 kΩ thin-film surface-mount resistors, model SOTA # S0303AS1501FKW, were purchased from State of the Art, Inc. of 2470 Fox Hill Rd., State College, Pennsylvania 16803-1797 USA.

[55] Stycast 2850FT, Emerson and Cuming Inc., Canton, Massachusetts 02021 USA.

[56] R. P. Elliott and F. A. Shunk, Bull. Alloy Phase Diagrams **1**, 45 (1980).

[57] C. P. Bidinosti, W. N. Hardy, D. A. Bonn, and R. Liang, Phys. Rev. Lett. **83**, 3277 (1999).

[58] M. A. R. Gunston, *Microwave Transmission-Line Impedance Data* (Van Nostrand Reinhold, UK, 1971).

[59] J. R. Pyle, IEEE. Trans. Microwave Theory Tech. **MTT-14**, 175 (1966).

[60] S. Amari, J. Bornemann, and R. Vahldieck, IEEE. Trans. Microwave Theory Tech. **MTT-44**, 2256 (1996).

[61] T. Pereg-Barnea, M.Sc. thesis, University of British Columbia (2001).

[62] G. K. Mullins, M.Sc. thesis, University of British Columbia (2003).

[63] T. Pereg-Barnea and P. J. Turner and R. Harris and G. Mullins and J. S. Bobowski and M. Raudsepp and Ruixing Liang and D. A. Bonn and W. N. Hardy, cond-mat\0311555, 2003, accepted to Phys. Rev. B.

[64] J. E. Sonier, J. H. Brewer, and R. F. Kiefl, Rev. Mod. Phys. **72**, 769 (2000).

[65] A. M. Chang, H. D. Hallen, L. Harriott, H. F. Hess, H. L. Kao, J. Kwo, R. E. Miller, R. Wolfe, J. van der Ziel, and T. Y. Chang, Appl. Phys. Lett. **61**, 1974 (1992).

[66] J. W. Guikema, J. H. Bluhm, D. A. Bonn, R. Liang, W. N. Hardy, and K. A. Moler, Submitted to Phys. Rev. Lett. (2003).

[67] L. Krusin-Elbaum, R. L. Greene, F. Holtzberg, A. P. Malozemoff, and Y. Yeshurun, Phys. Rev. Lett. **62**, 21 (1989).

[68] A. Carrington, R. W. Gianetta, J. T. Kim, and J. Giapintzakis, Phys. Rev. B **59**, 14173 (1999).

[69] C. Panagopoulos, J. R. Cooper, and T. Xiang, Phys. Rev. B **57**, 13422 (1998).

[70] T. Timusk and D. B. Tanner, in *Physical Properties of High Temperature Superconductors, Vol. 1*, edited by D. Ginsberg (World Scientific, Singapore, 1989).

[71] D. Y. Smith, in *Handbook of Optical Constants of Solids*, edited by E. D. Palik (Academic Press, Orlando, 1985).

[72] C. C. Homes, T. Timusk, D. A. Bonn, R. Liang, and W. N. Hardy, Physica (Amsterdam) **254C**, 265 (1995).

[73] D. N. Basov, R. Liang, D. A. Bonn, W. N. Hardy, B. Dabrowski, M. Quijada, D. B. Tanner, P. J. .Rice, D. M. Ginsberg, and T. Timusk, Phys. Rev. Lett. **74**, 598 (1995).

[74] D. A. Bonn, S. Kamal, A. Bonakdarpour, R. Liang, W. N. Hardy, C. C. Homes, D. N. Basov, and T. Timusk, Czech. J. Phys. **46**, 3195 (1996).

[75] R. Prozorov, R. W. Giannetta, A. Carrington, P. Fournier, R. L. Greene, P. Guptasarma, D. G. Hinks, and A. R. Banks, Appl. Phys. Lett. **77**, 4202 (2000).

[76] J. Y. Lee, K. M. Paget, T. R. Lemberger, S. R. Flotyn, and X. Wu, Phys. Rev. B **50**, 3337 (1994).

[77] P. Manca, S. Sanna, G. Calestani, A. Migliori, S. Lapinskas, and E. E. Tornau, Phys. Rev. B **63**, 134512 (2001).

[78] M. v. Zimmermann, J. R. Schneider, T. Frello, N. H. Andersen, J. Madsen, M. Kall, H. F. Poulsen, R. Liang, P. Dosanjh, and W. N. Hardy, Phys. Rev. B **68**, 104515 (2003).

[79] R. Prozorov, R. W. Giannetta, P. Fournier, and R. L. Greene, Phys. Rev. Lett. **85**, 3700 (2000).

[80] $^{155}$Gd and $^{157}$Gd each have nuclear spin $I = 3/2$ and natural abundances of 14.80% and 15.65% respectively. Typical values of the isotropic hyperfine coupling are 12 and 15 MHz, which are much smaller than our observed ZF ESR line width of about 300 MHz. A. Jánossy, private communication.

[81] A. Abragam and B. Bleaney, *Electron Paramagnetic Resonance of Transition Ions* (Clarendon press, Oxford, UK, 1970).

[82] A. Jánossy, A. Rockenbauer, S. Pekker, G. Oszlanyi, G. Faigel, and L. Korecz, Physica (Amsterdam) **171C**, 457 (1990).

[83] S. Pekker, A. Jánossy, and A. Rockenbauer, Physica (Amsterdam) **181C**, 11 (1991).

[84] A. Rockenbauer, A. Jánossy, L. Krecz, and S. Pekker, J. Mag. Res. **97**, 540 (1992).

[85] P. J. Turner, D. M. Broun, S. Kamal, M. E. Hayden, J. S. Bobowski, R. Harris, D. C. Morgan, J. S. Preston, W. N. Hardy, and D. A. Bonn, Rev. Sci. Instrum. **75**, 124 (2004).

[86] J. E. Sonier, J. H. Brewer, R. F. Kiefl, D. A. Bonn, S. R. Dunsiger, W. N. Hardy, R. Liang, W. A. MacFarlane, R. I. Miller, , et al., Phys. Rev. Lett. **79**, 2875 (1997).

[87] C. C. Homes, D. A. Bonn, R. Liang, W. N. Hardy, D. N. Basov, T. Timusk, and B. P. Clayman, Phys. Rev. B **60**, 9782 (1999).

[88] J. L. Tallon, C. Bernhard, U. Binninger, A. Hofer, G. V. M. Williams, E. J. Ansaldo, J. I. Budnick, and C. Niedermayer, Phys. Rev. Lett. **74**, 1008 (1995).

[89] B. Pümpin, H. Keller, W. Kündig, I. M. Savić, J. W. Schneider, H. Simmler, P. Zimmermann, E. Kaldis, S. Rusiecki, and C. Rossel, Hyperfine Interact. **63**, 25 (1990).

[90] Y. J. Uemura, G. M. Luke, B. J. Sternlieb, J. H. Brewer, J. F. Carolan, W. N. Hardy, R. Kadono, J. R. Kempton, R. F. Kiefl, S. R. Kreitzman, et al., Phys. Rev. Lett. **62**, 2317 (1989).

[91] B. R. Boyce, J. A. Skinta, and T. R. Lemberger, Physica (Amsterdam) **341C**, 561 (2000).

[92] L. A. deVaulchier, J. P. Vieren, Y. Guldner, N. Bontemps, R. Combescot, Y. Lemaître, and J. C. Mage, Europhys. Lett. **33**, 153 (1996).

[93] W. A. Atkinson, Phys. Rev. B **59**, 3377 (1999).

[94] C. Bernhard, C. Niedermayer, U. Binninger, A. Hofer, C. Wenger, J. L. Tallon, G. V. M. Williams, E. J. Anslado, J. I. Budnick, C. E. Stronach, et al., Phys. Rev. B **52**, 10488 (1995).

[95] W. Bardford and J. M. F. Gunn, Physica (Amsterdam) **156C**, 515 (1988).

[96] J. L. Tallon, J. W. Loram, J. R. Cooper, C. Panagopoulos, and C. Bernhard, Phys. Rev. B **68**, 180501 (2003).

[97] V. J. Emery and S. A. Kivelson, Nature **374**, 434 (1995).

[98] M. Prohammer and J. P. Carbotte, Phys. Rev. B **43**, 5370 (1991).

[99] P. A. Lee and X.-G. Wen, Phys. Rev. Lett. **78**, 4111 (1997).

[100] P. A. Lee and X.-G. Wen, Phys. Rev. B **59**, 3377 (1999).

[101] D. J. Scalapino, Phys. Rep. **250**, 329 (1995).

[102] I. F. Herbut and M. J. Case, cond-mat\0401101, 2004.

[103] P. J. Turner, R. Harris, S. Kamal, M. E. Hayden, D. M. Broun, D. C. Morgan, A. Hosseini, P. Dosanjh, G. Mullins, J. S. Preston, et al., Phys. Rev. Lett. **90**, 237005 (2003).

[104] R. Harris, Ph.D. thesis, University of British Columbia (2003).

[105] E. W. Hudson, K. M. Lang, V. Madhavan, S. H. Pan, H. Eisaki, S. Uchida, and J. C. Davis, Nature **411**, 920 (2001).

[106] S. H. Pan, E. W. Hudson, K. M. Lang, H. Eisaki, S. Uchida, and J. C. Davis, Nature **403**, 746 (2000).

[107] M. C. Nuss, P. M. Mankiewich, M. L. O'Malley, E. H. Westerwick, and P. B. Littlewood, Phys. Rev. B **66**, 3305 (1991).

[108] D. A. Bonn, P. Dosanjh, R. Liang, and W. N. Hardy, Phys. Rev. Lett. **68**, 2390 (1992).

[109] D. A. Bonn, R. Liang, T. M. Riseman, D. J. Baar, D. C. Morgan, K. Zhang, P. Dosanjh, T. L. Duty, A. MacFarlane, G. D. Morris, et al., Phys. Rev. B **47**, 11314 (1993).

[110] S. Kamal, D. A. Bonn, N. Goldenfeld, and P. J. Hirschfeld, Phys. Rev. Lett. **73**, 1845 (1994).

[111] S. Kamal, R. Liang, A. Hosseini, D. A. Bonn, and W. N. Hardy, Phys. Rev. B **58**, 8933 (1998).

[112] M. B. Walker and M. F. Smith, Phys. Rev. B **61**, 11285 (2000).

[113] A. J. Berlinsky, D. A. Bonn, R. Harris, and C. Kallin, Phys. Rev. B **61**, 9088 (2000).

[114] M. H. Hettler and P. J. Hirschfeld, Phys. Rev. B **61**, 11313 (2000).

[115] A. C. Durst and P. A. Lee, Phys. Rev. B **65**, 94501 (2002).

[116] R. Harris, A. Hosseini, S. Kamal, P. Dosanjh, R. Liang, W. N. Hardy, and D. A. Bonn, Phys. Rev. B **64**, 064509 (2000).

[117] J. Corson, J. Orenstein, S. Oh, J. O'Donnell, and J. N. Eckstein, Phys. Rev. Lett. **85**, 2569 (2000).

[118] G. D. Mahan, *Many-Particle Physics* (Plenum Press, New York, 1993).

[119] L. B. Ioffe and A. J. Millis, J. Phys. Chem. Solids **63**, 2259 (2002).

[120] P. A. Lee, Phys. Rev. Lett. **71**, 1887 (1993).

[121] E. Schachinger and J. P. Carbotte, Phys. Rev. B **67**, 134509 (2003).

[122] M. Sutherland, D. G. Hawthorn, R. W. Hill, F. Ronning, S. Wakimoto, H. Zhang, C. Proust, E. Boankin, C. Lupien, L. Taillefer, et al., Phys. Rev. B **67**, 174520 (2003).

[123] D. M. Broun, D. C. Morgan, R. J. Ormeno, S. F. Lee, A. W. Tyler, A. P. Mackenzie, and J. R. Waldram, Phys. Rev. B **56**, R11443 (1997).

# Appendix A

# Relating Surface Resistance to Power Absorption

For a conductor in an electromagnetic field, the total absorbed power per unit square area can be calculated by finding the real part of the complex Poynting vector **S** at the surface:

$$\mathrm{Re}\Big\{S_{zo}\Big\} = \mathrm{Re}\left\{\frac{1}{2}E_{xo} \times H_{yo}^{\star}\right\}. \tag{A.1}$$

Here we have taken the rectangular coordinate system geometry with a uniform conductor filling the half-space $z \leq 0$ which has a surface that covers the $x - y$ plane and a uniform harmonic magnetic field applied along the $y$-axis. Here we use the notation $S_{zo}$ which means the $z$ component of **S** evaluated at $z = 0$. Since the surface impedance $Z_s$ is defined to be $Z_s = E_{xo}/H_{yo}$, Eq. A.1 becomes

$$\mathrm{Re}\Big\{S_{zo}\Big\} = \mathrm{Re}\left\{\frac{1}{2}Z_s H_{yo}^2\right\}. \tag{A.2}$$

The tangential magnetic field at the conducting surface can be related to the surface current density **J** $(A/m^2)$ through a simple integration of Ampere's law:

$$\nabla \times \mathbf{H} = \mathbf{J}. \tag{A.3}$$

This can be integrated over the surface of our semi-infinite plane, followed by an application of Stoke's theorem to convert the curl integral to a line integral according to:

$$\oint \nabla \times \mathbf{H} \cdot d\mathbf{S} = \oint \mathbf{J} \cdot d\mathbf{S} \tag{A.4}$$

$$\oint \mathbf{H} \cdot dl = J_s \cdot l. \tag{A.5}$$

$J_s$ is the surface current per unit width $(A/m)$ and $l$ is the length along the surface. The integration path for **H** is chosen to be a loop running from deep inside the conductor where the field is zero, perpendicularly up to the surface and extending a length $l$ along the surface, then returning perpendicularly deep into the surface. For this case, the integral only picks up the tangential field at the surface where **H** is parallel to $dl$ and we have

$$H_{\mathrm{tangentialatsurface}} \cdot l = J_s \cdot l \tag{A.6}$$

$$\Longrightarrow H_{yo} = J_{so}. \tag{A.7}$$

With this result, Eq. A.8 becomes

$$\mathrm{Re}\left\{S_{zo}\right\} = \mathrm{Re}\left\{\frac{1}{2}Z_s H_{yo}^2\right\} \tag{A.8}$$

$$= \frac{1}{2}R_s J_{so}^2 \tag{A.9}$$

which is readily recognized as an Ohmic loss per unit area.

# Appendix B

# H.P.S. Model for Microwave Conducitivity of a $d$-wave Superconductor

The complete expression derived by Hirschfeld, Putikka and Scalapino [26] is:

$$\sigma_{xx}(\omega) = \left(\frac{ne^2}{m}\right) \int_{-\infty}^{\infty} d\varepsilon \left[-\frac{\partial f}{\partial \varepsilon}\right] N(\varepsilon) \mathrm{Im}\left(\frac{1}{\omega - \mathrm{i}/\tau(\varepsilon)}\right). \tag{B.1}$$

The above expression contains the approximation

$$\left[-\frac{\partial f}{\partial \varepsilon}\right] \approx \left[\tanh\left(\frac{\beta\varepsilon}{2}\right) - \tanh\left(\frac{\beta\varepsilon - \beta\omega}{2}\right)\right] / 2\omega \tag{B.2}$$

which is valid in the small $\omega/T$ limit which does not apply to the data analyzed in Chapter 4 of this thesis. There, the frequency (20 GHz) and temperature (1 K $\approx$ 21 GHz) are comparable and hence the full expression must be used.